The Dissertation Committee for Manas Ravindra Shah
certifies that this is the approved version of the following dissertation:

Modeling Self-Assembly and Structure-Property Relationships in Block Copolymers

Committee:

Venkat Ganesan, Supervisor

Isaac C. Sanchez

Donald R. Paul

Thomas M. Truskett

Muhammad H. Zaman

Modeling Self-Assembly and Structure-Property Relationships in Block Copolymers

by

Manas Ravindra Shah, B.Tech

Dissertation

Presented to the Faculty of the Graduate School of

The University of Texas at Austin

in Partial Fulfillment

of the Requirements

for the Degree of

Doctor of Philosophy

The University of Texas at Austin

December 2009

Dedicated to Smt. Swati R. Gujrathi and Shri Ravindra I. Gujrathi

Acknowledgments

First and foremost, I would like to express my sincere gratitude to my research supervisor Prof. Venkat Ganesan for his guidance and support throughout the course of my PhD. This dissertation would not have been complete without his ideas, knowledge, and constant encouragement.

I would like to extend my thanks to Dr. Victor Pryamitsyn for sharing his insights on many aspects of polymer physics and philosophy in general. I would like to specially thank him for his insights and help for Chapter 3. A special thanks to Prof Ganesan's group for scientific discussions and support.

I would like to thank the lunch group involving Amogh Prabhu, Gaurav Goel, Gaurav Gupta, Landry Khounlavong, Mehul Patel, and Reken Patel for making the daily routine of past 5 years more enjoyable. I would like to extend my thanks to Angad, Kedar, Navin, Nishant, Piyush, Raghu, and Ruchita for their constant encouragement and support.

Finally I would like to thank my parents and family for their exceptional support and understanding throughout these years.

Manas Ravindra Shah

The University of Texas at Austin
December 2009

Modeling Self-Assembly and Structure-Property Relationships in Block Copolymers

Publication No. ____________________

Manas Ravindra Shah, Ph.D.
The University of Texas at Austin, 2009

Supervisor: Venkat Ganesan

Block copolymers have been subject of tremendous research interest owing to their capability of undergoing self-assembly which allows them to tailor their electrical, optical, and mechanical properties. Statistical mechanics of flexible block copolymers is well understood. However, there are many unresolved issues with confinement of block copolymers as well as structure formation in block copolymers having non-flexible polymer blocks. We develop mean field theory models to address the issues arising in thermodynamics of such complex block copolymers. Also, we develop theoretical formalisms to understand the link between morphology and macroscopic properties in these block copolymers.

We study the stability and ordering in thin films of flexible diblock copolymer in the presence of compressible solvent using a combined polymer mean field theory and lattice gas model for binary fluid mixtures. We utilize mean field theory model to understand the self-assembly behavior in side-chain liquid crystalline block copolymers which involve interplay between microphase separation and liquid crystalline ordering of side chain mesogenic units.

We extend the field theoretic models for block copolymer to account for self-assembly in semicrystalline block copolymers. The semicrystalline chain is modeled as a semiflexible chain having non-bonded attractions between parallel bonds. We characterize the structure formation in such block copolymers as a function of the rigidity of the semicrystalline chain. Then we extend the formalism to study semicrystalline triblock and pentablock copolymers and evaluate bridging fractions in different sequences of semicrystalline multiblock copolymers.

Rod-coil block copolymers have a flexible polymer covalently linked to rigid polymer. Such polymers have potential applications as organic LEDs and photovoltaic devices. We study the self-assembly of such block copolymer under confinement. To make these block copolymers viable as photovoltaic devices, we performed the photovoltaic modeling of devices based on self-assembly of block copolymers. We characterize the interplay between self-assembly and anisotropy of charge transport (arising due to rigid polymer chains) in determining the eventual photovoltaic properties.

Contents

Acknowledgments **v**

Abstract **vi**

List of Figures **xii**

Chapter 1 Introduction **1**

- 1.1 Predicting Self-Assembly in Complex Block Copolymers 6
  - 1.1.1 Block Copolymer Thin Films in Presence of Compressible Solvent 7
  - 1.1.2 Side Chain Liquid Crystalline Block Copolymers 8
  - 1.1.3 Semicrystalline Block Copolymers 10
  - 1.1.4 Thin Films of Rod-Coil Block Copolymers 11
- 1.2 Computational Modeling of Structure-Property Relationship in Block Copolymers 12
  - 1.2.1 Mechanical Properties of Semicrystalline Multiblock Copolymers 13
  - 1.2.2 Morphology-Property Correlations in Rod-Coil Block Copolymers for Photovoltaic Applications 14
- 1.3 Thesis Organization 17

Chapter 2 Block Copolymer Thin Films in Presence of Compressible Solvents **21**

- 2.1 Introduction 21
- 2.2 Description of Theoretical Framework 23
  - 2.2.1 Model for Compressible Solvent 24
  - 2.2.2 SCFT framework 26

2.3 Free energy analysis 32
2.4 Results 37
2.5 Conclusions 41

Chapter 3 Self-Assembly of Side-Chain Liquid Crystalline Block Copolymers 43
3.1 Introduction 43
3.2 Description of SCFT Model and Framework 49
    3.2.1 Details of Numerical Calculations and Parameters . . . 59
3.3 Results and Discussion 63
    3.3.1 Phase Diagram and Morphologies 63
    3.3.2 Effect of molecular weight 69
    3.3.3 Summary of Results From Other Parametric Studies . 71
3.4 Strong Segregation Theory For Ordering in SCLC 74
    3.4.1 Model and Governing Equations 74
    3.4.2 Physical Insights From SST 81
    3.4.3 Comparisons of SST Results to SCFT 83
3.5 Conclusions 86

Chapter 4 Mechanical Properties of Semicrystalline Multiblock Copolymers 88
4.1 Introduction 88
4.2 Background and Description of Model 92
4.3 Model and Numerical Details 98
    4.3.1 Expansion in Spherical Harmonics 103
    4.3.2 Numerical Implementation 106
    4.3.3 Calculation of Bridge and Loop Fractions 107
4.4 Results and Discussion 108
    4.4.1 Diblock copolymers 109
    4.4.2 Triblock Copolymers 117
    4.4.3 Pentablock Copolymers 123
4.5 Conclusions 128

Chapter 5 Thin Film Morphologies of Rod-Coil Block Copolymers 130
5.1 Introduction 130
5.2 SCFT Model 135
  5.2.1 Key Ingredients 135
  5.2.2 Treatment of Surface Potential and Boundary Conditions 136
5.3 Results and Discussion 138
  5.3.1 Confinement by Neutral Surfaces 138
  5.3.2 Effect of Coil Attractive Surfaces 144
  5.3.3 No Flux Boundary Condition 147
5.4 Summary 151

Chapter 6 Morphology Property Correlations of Rod-Coil Block Copolymers for Photovoltaic Applications 152
6.1 Introduction 152
6.2 Drift-Diffusion Modeling of Device Characteristics 159
  6.2.1 Model 159
  6.2.2 Non-Dimensionalization of Drift-Diffusion Equations . 167
  6.2.3 Boundary Conditions and Numerical Details 167
  6.2.4 Parameters 170
  6.2.5 SCFT Model For Donor-Acceptor Morphologies 171
6.3 Results and Discussion 174
  6.3.1 Influence of the morphology of self-assembly upon device characteristics 174
  6.3.2 Effect of Domain Sizes 181
  6.3.3 Effect of Chemical Incompatibility and Degree of Phase Separation 184
  6.3.4 Influence of anisotropic charge transport characteristics 186
6.4 Summary and Outlook 194

Chapter 7 Future Work 196

Bibliography **199**

Vita **217**

List of Figures

1.1 (a) Theoretical and (b) Experimental phase diagrams of flexible diblock copolymers. Thermodynamics is characterized by two parameters - product of Flory-Huggins interaction parameter and degree of polymerization (χN), and volume fraction of one of the blocks (f). Adapted from Ref. [1]. 2
1.2 Schematics of rod-coil block copolymer, side-chain liquid crystalline block copolymer, and semicrystalline diblock copolymer. 4
1.3 Current-voltage characteristics of donor-acceptor block copolymer (B) compared that with blend (A) of donor and acceptor. Both the short circuit current J_{SC}, and open circuit voltage V_{OC} are higher for the block copolymer as compared to the blend. (Adapted from Ref. [2]) 16

2.1 Plot of $d\tilde{\phi}_S/dP$ vs P. The peak is sharper and higher for $\chi_{SV} = 1.9$ than for $\chi_{SV} = 1.5$. $\chi_{SV} = 1.9$ is closer to the critical point. 25
2.2 Free energy per unit area of the film as a function of x - distance from the substrate. The value of Flory-Huggins interaction parameter is $\chi_{AB}N = 12$ and the volume fraction of copolymer is $\phi = 0.35$. The solvent condition is fixed corresponding to $\chi_{SV} = 1.9$, $z = 1.2118$, $\tilde{P} = 1.35$, $\chi_{\bar{S}P}N = -25$. 33
2.3 Free energy as a function of total polymer concentration Φ_P for three different values of $\chi_{AB}N$.The solvent condition is fixed corresponding to $\chi_{SV} = 1.0$, $z = 0.814$, $\tilde{P} = 1.35$, $\chi_{\bar{S}P}N = -25$. These values of F are corrected with the bulk value of free energy 35
2.4 (a) The LDT (thin film systems, closed symbols) and ODT (bulk systems, open symbols) $\chi_{AB}N$ versus pressure ($\tilde{P}$) for. (b) The solvent volume fraction Φ_S *vs.* pressure for the cases shown in Part (a). The volume fraction of the block copolymer relative to the total volume of the system is fixed at $\phi = 0.15$. 39
2.5 The LDT (thin film systems, closed symbols) and ODT (bulk systems, open symbols) $\chi_{AB}N$ as a function of pressure $\tilde{P}$ for different values of $\chi_{\bar{S}P}N$ in thin film (closed symbols) and bulk systems (open symbols). The value of χ_{SV} is fixed at 1.5. . . . 40

3.1 (a) Molecular structure of a SCLC copolymer used in the experiments of Hammond and coworkers [3]. (b) A schematic of our model for side chain liquid crystalline polymer. N_A monomers of A block is attached with a B block having N_R number of attached mesogenic units. 48

3.2 Self assembly phase diagram obtained from 2D calculations. The parameters are $N = 200$ and $m = 5$. The solid line represents the transition from disordered phase to microphase separation, and the dashed line represents the transition to smectic ordering. Open diamonds represents disordered phase, while triangles represent lamellar phases and the circles represent the cylindrical morphologies discussed in the text. 62

3.3 (a) Hexagonally packed coil cylinders in a continuous LC block phase. $N = 200$, $m = 5$, $f_A = 0.22$ and $\chi_1 N = 25$. (b) The z-component ($\mathbf{S}_z(\mathbf{r})$) of the eigenvector corresponding to $\lambda_{max}(\mathbf{r})$. In regions where LC phase appears, the value of $\mathbf{S}_z(\mathbf{r})$ is 1.0, which implies that the orientation is along the z-axis. (c) A schematic representation for this morphology along with the nature of orientation of side chain liquid crystalline units within these microphases. 65

3.4 (a) Lamellar morphology for amorphous and LC blocks. The parameters are $N = 200$, $m = 5$, $f_A = 0.64$ and $\chi N = 10$. The rods are oriented parallel to interface between the two blocks. (b) A plot of the z-component ($\mathbf{S}_z(\mathbf{r})$) of the eigenvector corresponding to $\lambda_{max}(\mathbf{r})$. In regions, where the LC phase appears, the orientation is along the z-axis. (c) A schematic representing microphase separation and orientational ordering. 66

3.5 (a) Hexagonally packed LC cylinders in a matrix of A block. The parameters are $N = 200$, $m = 5$, $f_A = 0.76$ and $\chi_1 N = 18$. (b) A plot of the z-component ($\mathbf{S}_z(\mathbf{r})$) of the eigenvector corresponding to $\lambda_{max}(\mathbf{r})$. In regions, where the LC phase appears, the orientation is along the z-axis. (c) A schematic representation of the observed morphology. 70

3.6 (a) Self assembly phase diagram obtained from 2D calculations for the parameters are $N = 100$ and $m = 5$. Microphase separation and isotropic-smectic transition occurred at the same value of $\chi_1 N$ for this parametric case. (b) Comparison of microphase separation transition and isotropic-nematic transition (I-N) of the rods units for two cases: $N = 200$ and $m = 5$, and $N = 100$ and $m = 5$. 72
3.7 (a) SST phase diagram for the parameters $N = 100$ and $m = 5$. (b) SCFT phase diagram for the case $N = 100$, $m = 3$ and $\beta = 1$. (c) SST phase diagram for the case $N = 100$ and $m = 3$. In (a) and (c) the I-N transition lines coincide with the ODT's for a major portion of the phase diagram. 85

4.1 Schematic of bridging (B), looping (L), and free (F) conformations in AB diblock, ABA triblock, and ABABA pentablock copolymers. A bridging (B) conformation occurs when the ends of a middle block in a multiblock copolymer lie on different interfaces, whereas in a looped (L) configuration, both the ends lie on the same interface. In a free (F) conformation, only end of a chain is tethered to an interface, while other end is free. Solid line represents A chain, while the dotted line represents B chain. The dashed horizontal lines represents the planes of failure in the two domains in diblock and triblock copolymers. 90
4.2 Density and orientational order parameter for fixed $f = 0.50$, $\mu/\chi = 3$, $\beta = 6$. and $\lambda/\chi N = 0.03$. As we increase the value of χN (or equivalently decrease T), we observe orientational order growing inside the semiflexible polymer, and consequently the domain size increases. The orientational order parameter for these 3 values of χN are, $\mathbf{S} \approx 0$ ($\chi N = 13$), $\mathbf{S} = 0.43$ ($\chi N = 14$) and $\mathbf{S} = 0.59$ ($\chi N = 17$). This observation is akin to crystallization within lamellar morphologies. 110
4.3 Density and orientational order parameter for low and high values of chain rigidity, λ. The parameters are $\chi N = 18$, $\mu N = 54$, $f = 0.50$, and $\beta = 6$. The values of λ are a. 0.036, b. 0.36. The orientational order parameter for these 2 values of χN are, $\mathbf{S} \approx 0$ ($\chi N = 12$), and $\mathbf{S} = 0.68$ ($\chi N = 18$). 113

4.4 Scaling exponents of D as a function of fN for different values of rigidity, λ. The values of the other parameter are : $\chi N = 18$, $\mu/\chi = 3$, and $\beta = 6$. α represents the scaling exponent for domain spacing as a function of degree of polymerization of the flexible block. The straight lines represents the linear fit to the data points of domain scaling. Slope of these lines is used to evaluate the scaling exponent, α. (The plots are shifted on the y-axis to provide a better clarity, but it does not affect the slope of this log-log plot.) 117
4.5 The bridging volume fraction plotted as a function of persistence length λ for ABA and BAB. The filled triangle represents the value of f_{br} for a flexible ABA triblock copolymer. The parameters for this case are : $\chi N = 32$, $f = 0.50$, $\mu N = 80$, and $\beta = 12$. 119
4.6 Correlation between bridging fraction and nematic order parameter of the midblock chain in ABA triblock copolymer. The parameters are same as the one used in Fig. 4.5. 119
4.7 Correlation between the bridging fraction of A domain in BAB copolymer and the domain size of the flexible block (D_A). With increasing persistence length the domain size increases, while the bridging fraction (f_{br}) decreases. 122
4.8 Bridging fractions in B domains of ABA, ABABA and BABAB copolymers. The parameters are $\chi N_{penta} = 50$, $\chi N_{tri} = 50$, $\beta = 12$, and $\mu/\chi = 2.5$. Both the sequences of pentablock copolymers are symmetric and posses equal volume fractions of A and B, i.e. $f_1 = f_5 = 0.125$, and $f_2 = f_3 = f_4 = 0.25$. The variation of bridging fraction as a function of rigidity is qualitatively similar for both triblock and pentablock copolymers irrespective of the nature of the sequence. 124
4.9 Bridging fractions in A domains of ABA, ABABA and BABAB copolymers. The parameters are $\chi N_{penta} = 50$, $\chi N_{tri} = 50$, $\beta = 12$, and $\mu/\chi = 2.5$. Both the sequences of pentablock copolymers are symmetric and posses equal volume fractions of A and B, i.e. $f_1 = f_5 = 0.125$, and $f_2 = f_3 = f_4 = 0.25$. The variation of bridging fraction as a function of rigidity is qualitatively similar for both triblock and pentablock copolymers irrespective of the nature of the sequence. 126

5.1 Schematic of orientation of rod chains within block copolymer microphases for smectic A and smectic C alignment. 132
5.2 (a) Free energy plot for parallel and perpendicular lamellae for a smectic A case in bulk. The perpendicular lamellae posses lower free energy over the entire range of thickness. The parameters are : $\chi N = 10$, $f = 0.4$, $\omega N = 30$, and $\beta = 6$. (b) Density profile of the coil phase for $\Delta = 22R_g$. Red : Coil Block, Blue: Rod Block. 139
5.3 $\chi N = 8.0$, $f = 0.5$, $\beta = 10.$, $\omega N = 32$. Like for Smectic A morphology, perpendicular lamellar orientation is preferred for smectic C cases too. 142
5.4 Representative density profiles for confined puck phase (a) $\chi N = 12$, $f = 0.6$, $\beta = 10.$, $\omega N = 48$ and (b) $\chi N = 16$, $f = 0.7$, $\beta = 10$, $\omega N = 64$. 143
5.5 (a) Free energy versus thickness plot for parallel and perpendicular lamellae for the case considered in Fig. 5.2. $\lambda_1 = \lambda_2 = -20$. Perpendicular free energy has lower free energy even upon introduction of attractive interactions for coil. (b) Representative density profiles of parallel and perpendicular lamellae. 145
5.6 Plot of free energy as a function of thickness for parameters studied in Fig. 5.2. Here we apply Neumann condition for coil chain propagator function. In this framework, the perpendicular lamellae has the lowest free energy. 149
5.7 Free energy vs thickness variation for parallel and perpendicular lamellae for the case of very short rods. $\chi N = 12$, $f = 0.4$, $\omega N = 96$, and $\beta = 2$. The length of rods is comparable to coil layer near the surface, and thus the smectic A orientation is preserved near the surfaces under confinement. 149
5.8 (a) $\omega N = 18$. This case is near isotropic-nematic transition. (b) $\omega N = 30$. This case is for higher orientational ordering in the rod block. Smectic ordering inside the rod phase tends to favor the perpendicular lamellar orientation. 150

6.1 (a) Density profiles for donor and acceptor phases for parallel lamellae, and perpendicular lamellae. The coil block is shown in red and the rod block is shown in the blue phase. The parameters are: $\chi N = 10$, $f = 0.40$, $\omega N = 30$, and $\beta = 6$. (b) J-V curves for the above phases. The units are Am^{-2} for current density (J), and Volts for voltage (V). 173

6.2 (a) Schematics for parallel and perpendicular bilayer morphology. The red phase is the acceptor layer and blue layer is the donor phase. (b) Effect of domain orientation on the J-V response. The units are Am^{-2} for current density (J), and Volts for voltage (V). (c) Electron density (n) for parallel and perpendicular bilayer morphology. $V = 0.45V$, $\Delta = 100nm$. . . . 176
6.3 (a) Density profiles for donor and acceptor phases for puck phases. The parameters are $\chi N = 16$, $f = 06.$, $\omega N = 64$, and $\beta = 10$. (b) J-V curve for puck morphology compared with J-V curves for parallel and perpendicular morphology. It is quite evident that having straight nanostructured lamellar like morphologies between the two electrodes greatly improves the photovoltaic short-circuit current. The units are Am^{-2} for current density (J), and Volts for voltage (V). 178
6.4 Representative density profiles for blend and block copolymer morphologies obtained from SCFT simulations. The domain size in block copolymers are much smaller than the blend morphologies. The blend morphology is obtained by simulating a blend of rod polymers and solvent in SCFT framework. It is easily observed that the domain sizes in block copolymers are much smaller as compared to blend systems. 180
6.5 Effect of domain spacing for rod-coil block copolymers on the short-circuit current. 180
6.6 (a) Schematic of perpendicular multilayer morphology. (b) Effect of domain spacing for different exciton lifetimes. There exists an optimal domain width which produces the maximum J_{SC}. 183
6.7 (a) 1D rod density profiles for $\chi N = 8$, $\chi N = 12$, and $\chi N = 20$. These are generated by considering a slice of perpendicular lamellar morphology. Well microphase separated lamellaes are observed for higher χN value. (b) J-V curves for different values of phase separation characterized by χN. The units are Am^{-2} for current density (J), and Volts for voltage (V). (c) The relationship between interfacial width (ξ) in non-dimensional units and χN. (d) The relationship between J_{SC} and ξ (nm) for artificial perpendicular bilayer morphology. 187

6.8 One dimensional density profiles of orientational order parameter ($S(\mathbf{r})$), and rod density ($\phi_R(\mathbf{r})$) for three values of ωN - (a) 15, (b) 40, and (c) 100. 188
6.9 Effect of anisotropic mobility and orientational ordering on photocurrent. For well aligned rods, there exists an optimum value of μ_R which results in highest short-circuit current. 189
6.10 Effect of anisotropic mobility on photocurrent for two different thickness, 80 nm and 120 nm. The short circuit current is much higher in the thinner films. Also, the anisotropy effect is more pronounced for thinner devices. $\omega N = 40$. 191
6.11 (a) Effect of domain spacing for rod-coil block copolymers on the short-circuit current. The variation of $|J_{SC}|$ as a function of domain size is different for isotropic and anisotropic charge transport. The units of J_{SC} is Am^{-2}. (b) The reduction in short circuit current is due to an increased recombination rate. The numbers on y-axis should be multiplied by 10^{26}, and units are $m^{-3}s^{-1}$. 193

Chapter 1

Introduction

Block copolymers have attracted tremendous attention due to their capability to self-assemble which allows for tailoring of their mechanical, electrical, barrier, optical, and other physical properties [1, 4, 5, 6]. They are found to be important for technologies like adhesives, additives, lithography, thermoplastic elastomers, and recently organic electronic devices. The simplest and most studied block copolymer is flexible AB diblock copolymer, whose thermodynamics is well understood both theoretically and experimentally [1, 5, 6]. In Fig. 1.1, the theoretical and experimental phase diagram of flexible diblock copolymer is shown. The final microstructure is determined by the volume fraction of one of the monomers (f), and the incompatibility between the two blocks governed by the product χN, where χ denotes the Flory-Huggins interaction parameter and N the overall degree of polymerization ($\chi \propto 1/T$, where T denotes the temperature) [1, 5]. Depending on these two parameters, the diblock copolymer self-assembles to form microstructures such as lamellar, cylindrical, spherical, gyroid etc. The final morphology is governed by the balance between the incompatibility between two blocks and the conformational entropy of the two chains.

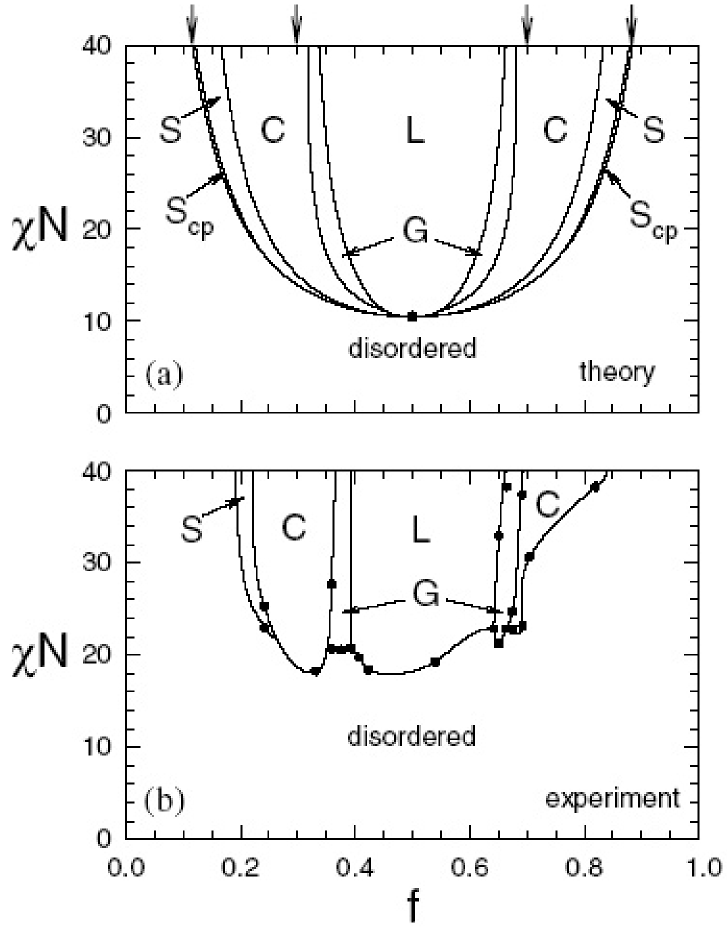

Figure 1.1: (a) Theoretical and (b) Experimental phase diagrams of flexible diblock copolymers. Thermodynamics is characterized by two parameters - product of Flory-Huggins interaction parameter and degree of polymerization (χN), and volume fraction of one of the blocks (f). Adapted from Ref. [1].

The self-assembly of multiblock copolymers and block copolymers with rigid blocks is significantly more complex than flexible counterparts. There has been lot of interest in studying block copolymers with rigid rod-like blocks either attached in the main chain (rod-coil block copolymers) [7, 8] or grafted as side chains to flexible block copolymers (side chain liquid crystalline polymers) [9, 10]. The self-assembly of such complex polymers is expected to be much more richer due to the interplay of the microphase separation and the liquid crystalline ordering between rod-like units [8]. Such block copolymers have potential applications in the area of organic electronics, namely electro-optical devices, organic LEDs, and organic photovoltaic devices. To make these technologies viable, it is necessary to understand the self-assembly in such polymers as well have the ability to predict how a given structure affects its final properties.

Another set of technologically important block copolymers are semicrystalline multiblock copolymers which have shown great potential as thermoplastic elastomers [11]. In such polymers, a crystallizable polymer is attached to flexible (or amorphous) polymer to allow tailoring of mechanical properties such as toughness of the polymer. Self-assembly in such polymers is characterized by complex interplay between microphase separation between the different blocks and crystallization of one of the blocks [12, 13]. Understanding how these different phenomena interact with one another to determine the final morphology is important. These three examples of block copolymers which involve non-flexible blocks are schematically represented in Fig. 1.2.

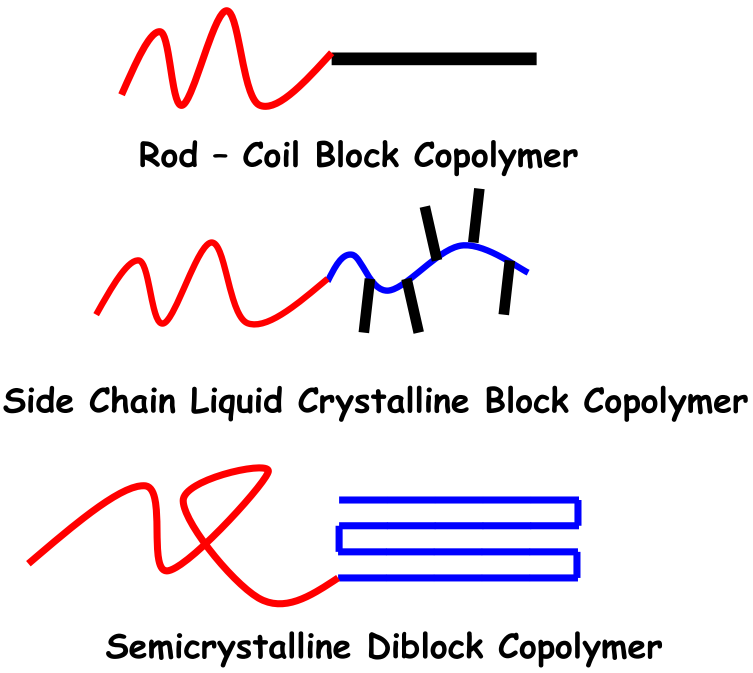

Figure 1.2: Schematics of rod-coil block copolymer, side-chain liquid crystalline block copolymer, and semicrystalline diblock copolymer.

Self-assembly in all these three categories of block copolymers will be considered in this thesis.

Another crucial factor which can potentially impact the morphology of block copolymers is the presence of confining surfaces [14, 15, 16]. In such cases, thermodynamics of polymers is influenced both by the nature of the confining surfaces, as well as the thickness of the polymer film. As seen from above examples, it is clear that from both technological as well as fundamental viewpoint it is necessary to understand how these complex phenomena such as crystallization, liquid crystalline ordering, microphase separation, and surface ordering interplay with one another to determine the phase behavior of these complex polymers.

One of the important objectives of this thesis to develop theoretical frameworks which would enable us to understand the complex self-assembly in such block copolymers. Computational modeling has emerged as important tool in predicting the structure and properties of complex fluids such as polymers, colloids, and biological materials [17]. Fully atomistic methods (like Molecular Dynamics) are computationally expensive to understand the equilibrium phase behavior of such types of block copolymers [18]. Field theoretic based models have been successfully utilized to predict the equilibrium phase behavior of melts and solutions of flexible block copolymers in bulk and under confinement [17, 18]. We will be utilizing self-consistent field theory (SCFT) framework to develop theoretical models to understand the phase behavior in some of these technologically important polymers, for which the present understanding is limited.

The second important objective of my thesis to provide theoretical frameworks in some of the above systems which help us in correlating their nanoscale structure to their final macroscopic properties (mechanical, electrical etc). There is a need to understand the structure-property link in these polymers to make them technologically viable. Computational modeling can play a huge role in understanding the structure-property link in these systems [19, 20]. Mechanical properties of semicrystalline multiblock copolymers are dependent on the crystallinity of one of the blocks, overall block architecture, and other molecular parameters [11, 21]. Another important example is the role of microstructure in semiconducting rod-coil block copolymers in determining its photovoltaic efficiency. In both these systems, we attempt to develop appropriate theoretical models to understand the structure-property link in order to optimize the material performance. We discuss these interesting problems in the next subsections, where the overall goals of this thesis are further elucidated.

1.1 Predicting Self-Assembly in Complex Block Copolymers

In this section, we discuss the different systems of block copolymers that were studied in this thesis. We illustrate in some detail the motivation behind studying each of these systems and our approach to understand the thermodynamics of these complex systems. In this part of thesis, we seek to improve our understanding of fundamental phenomena like microphase separation, liquid crystalline ordering, polymer crystallization, and interfacial effects and how they interplay with each other to determine the overall phase behavior.

1.1.1 Block Copolymer Thin Films in Presence of Compressible Solvent

Block copolymer thin films have tremendous applications in the areas of lithography, coating, and templates. The overall stability and ordering within block copolymer films is determined by the nature of confining surfaces and the thickness of the film [22]. Recently, there has been significant attention directed towards utilization of "benign" solvent like supercritical CO_2 (a compressible solvent) for polymer processing [14, 23, 24]. In the case of diblock copolymer *bulk* systems which exhibit upper critical order-disorder temperature behavior (UODT, i.e. order upon cooling), the compressible solvent has been shown to screen the unfavorable interactions between the two blocks, resulting in lowering the temperature needed for microphase separation. However, experiments of Arceo and Green [14] have demonstrated the opposite effect in free standing films of flexible diblock copolymer (PS-*b*-PMMA), i.e. the UODT is significantly enhanced with respect to the bulk.

Computational modeling can provide an insight into this seemingly contradictory phase behavior of thin films of block copolymers in the presence of the compressible solvent. Previous mean field theory models considered cases where block copolymer was confined between two hard surfaces [16, 25]. However, to truly understand the phase behavior and stability of free standing thin films in presence of a solvent, one needs to have a model for supported thin films (or free standing films) [26]. In Chapter. 2, we show how we developed a novel model to treat supported thin films of block copolymers in presence of compressible solvent. Using a free energy framework, we were able to characterize the stability and various ordering transitions in thin films of block copolymers in a compressible solvent environment and compare the results with bulk phase behavior [27].

1.1.2 Side Chain Liquid Crystalline Block Copolymers

Liquid crystalline polymers (LCP) are a special class of polymers possessing mesogenic units capable of orientational ordering in addition to morphological assembly. Such polymers have attracted significant attention in view of their potential applications in electrooptical display devices and high strength fibers [28]. Side-chain liquid crystalline block copolymers are unique class of liquid crystalline polymers consisting of side chain mesogenic units grafted typically through alkyl spacers on a flexible backbone [29]. Several experimental groups have studied the phase behavior and properties of side chain liquid crystalline block copolymers [29, 30, 31]. Such block copolymers have been touted to have potential applications in industrial electooptical and display applications because of their capability to form microphase separated structures. Conventional devices suffer from two drawbacks - maintaining constant cell thickness and maintaining the orientations of mesogens throughout the device. Block copolymer structure can alleviate both the issues. Block copolymer microstructure provides constant cell thickness and it also stabilizes the mesogen ordering and provides structural integrity [29].

Side-chain LC block copolymers exhibit rich self-assembly characteristics that manifest an interplay between the backbone flexible block copolymer ordering and liquid crystalline ordering between side chain mesogenic units. The morphologies are similar to that of flexible block copolymer in addition of smectic orientational ordering confined between block copolymer mesophases [29, 30, 31]. In contrast to the significant theoretical developments accompanying self-assembly in flexible block copolymers, methods and models for predicting the self-assembly behavior of side chain liquid crystalline block copolymers are very limited. Applying Monte Carlo and Molecular Dynamics methods for this polymers would be extremely computationally expensive. Modeling the phase behavior of this polymer is complex on two accounts - (i) how does self-assembly of diblock copolymer backbone influence the LC ordering in side chains, and (ii) how does orientational ordering in side chains affect the phase behavior of block copolymers? We propose a combined study based on self-consistent mean field theory (SCFT) and strong segregation theory (SST) to understand the self-assembly characteristics of side chain liquid crystalline (SCLC) block copolymers. As we show in Chapter. 3, our SCFT model takes into account how liquid crystalline ordering and microphase separation interplay with each other to determine the final phase behavior. The strong segregation theory is utilized to provide rationalizations for the results provided by SCFT numerical simulations.

1.1.3 Semicrystalline Block Copolymers

Crystallizing one of the components of the block copolymer leads to profound changes in the structure of the block copolymer [6]. There has been enormous research activity on semi-crystalline diblock copolymers on the experimental side [32, 33, 34, 35]. It is observed that combining two self-organizing mechanisms, such as crystallization and microphase separation, into a single polymer can lead to extremely rich morphological richness and kinetic complexities. However, unlike the crystalline homopolymers, where the final morphology is dependent on the kinetic pathway, in the case of semi-crystalline block copolymer, equilibrium considerations play a major role in deciding the final morphology [34]. Understanding self-assembly in semicrystalline block copolymer is essential to make them useful for thermoplastic elastomeric applications [36, 37].

There is no comprehensive theory for crystallization in block copolymers that can account for the configuration of the crystallites inside mesophases, i.e. both the extent of folding and the nature of orientation with respect to interface, as well account for non-lamellar phases observed in the experiments [12]. The earliest theoretical models were based on scaling analysis or mean field theory to determine the amorphous and the crystalline domain thickness as a function of the degree of polymerization [38, 39, 40].

We model semicrystalline diblock copolymers as combination of flexible rubbery unit linked to a crystalline unit, which is modeled as a semiflexible chain with a temperature dependent rigidity and orientational interactions between parallel bonds [21]. The model proposed for crystalline chain is in line with ideas proposed by Flory [41] and recently adapted by Frenkel and coworkers [42, 43]. We show in Chapter. 4 how our model is able to predict structure formation in semicrystalline diblock copolymer and how our results compare with previous theories and experimental results.

1.1.4 Thin Films of Rod-Coil Block Copolymers

Self-assembly of rod-coil block copolymers is gaining attention due to potential applications in organic electronic devices [2, 7, 8]. Theory and experiments have suggested an extremely rich morphological phase behavior due to interplay between microphase separation and liquid crystalline ordering within the conjugated rod block [44, 7, 8]. Unlike the case of flexible diblock copolymer, the rigid nature of one of the block dictates the phase behavior and domain size in rod-coil block copolymers.

For applications in organic electronic devices, these polymers need to be patterned onto thin films [2, 45, 46]. So it is important to study the effect of confinement and surface interactions on rod-coil block copolymers phase behavior. Confined thin film of rod-coil block copolymers is an extremely constrained system [47]. There are additional complications due to the rigid nature of the rod like block and hard confining surfaces. If the thickness of the film is incommensurate with bulk domain spacing, this can lead to change in domain spacing or the orientation might get flipped to form perpendicular lamellae [45, 47]. Also the orientation of the rod block with respect to lamellar interface can change under confinement. In free standing films of rod-coil block copolymers, it has been observed that on increasing the thickness of the film, the amount of perpendicular lamellae in the thin film increase [45]. To understand these effect and obtain the optimal morphologies for photovoltaic devices (Refer Section. 1.2.2), we extend the field theoretic formalism of Pryamitsyn and Ganesan [8] to account for confinement and surface preference effects. We analyze how the morphologies and orientation of rod-like units shift from the bulk.

1.2 Computational Modeling of Structure-Property Relationship in Block Copolymers

Tuning structure property relationships in block copolymers is an important step towards making them technologically viable. Computational modeling can play a significant role in complementing experiments in order to optimize the morphologies of a particular type of polymer for desired macroscopic properties. In the following two subsections, we describe our proposals for optimizing the morphologies of semicrystalline multiblock copolymers and rod-coil block copolymers to improve their mechanical and photovoltaic properties respectively.

1.2.1 Mechanical Properties of Semicrystalline Multiblock Copolymers

Conventional thermoplastic elastomeric block copolymers, such as poly-(styrene-b-butadiene-b-styrene) (SBS), poly(styrene-b-isoprene-b-styrene) (SIS) etc. typically use microphase separated morphologies in which the glassy hard blocks which act as crosslinks for the soft rubbery blocks. This arrangement leads to the high levels of elasticity and toughness desired of thermoplastics for applications [48, 49, 50]. The more recent developments aim to mimic such characteristics in multiblock copolymers by either linking crystalline polyolefinic end blocks to soft polyolefinic middle blocks [51, 37] or by linking brittle glassy hydrogenated polystyrene blocks to softer crystalline polyethylene blocks [48, 11, 52]. These newer class of materials have been reported to have low Young's moduli, large strains at break, and excellent elastic recovery properties rivalling even commercial thermoplastic elastomers [51]. Many experimental studies have clearly shown that there is a strong correlation between the chain conformations of multiblock copolymers and their mechanical properties and modes of material failure. It has been shown that mechanical toughness is directly linked to *bridging* conformations in these copolymers [53]. For instance, experiments studying PCHE(C)-PE(E) multiblock copolymers have shown that the failure mode changes from a brittle to ductile upon changing the architecture from a triblock copolymer (which contains "bridged" planes only in the E domains) to pentablock copolymers (which contains "bridged" planes in both E and C domains) [48, 52]. In addition, a recent study by Phatak and coworkers found that irrespective of the chain architecture of these multiblock copolymers, a universal correlation can be established between the tensile strength of the material and the fraction of bridging in semicrystalline E domains [11].

There have been several prior theoretical studies quantifying the different chain conformations in microphase separated phases of *flexible* multiblock copolymers utilizing mean field theories [19, 54]. While much of the above studies have focused on the case of flexible multiblock copolymers, to our knowledge, none of the prior theoretical studies have explicitly addressed the issues of bridging and looping conformations in the more experimentally relevant system of *semicrystalline* multiblock copolymers. The ability of one (or more) of the blocks to crystallize and fold is expected to significantly impact the quantitative details pertaining to the fraction of bridges and loops. We extend the model developed for semicrystalline diblock copolymer (Section. 1.1.3) for multiblock (triblock and pentablock) copolymers and correlate the architecture and crystallinity of one of the blocks with the amount of bridging fractions in different domains of these multiblock copolymers.

1.2.2 Morphology-Property Correlations in Rod-Coil Block Copolymers for Photovoltaic Applications

Photovoltaics or solar cells are being increasingly seen as important candidates for source of renewable energy. Organic solar cells are gaining popularity since they are relatively inexpensive and can be fabricated onto flexible substrates over high surfaces areas using high throughput solution processing techniques [55, 56]. However presently the efficiencies of polymer solar cells are lower than conventional devices, and hence there is a need to understand the relationship between microstructure of polymeric devices and their final properties in order to design efficient polymer photovoltaic devices. It has been shown that having a microphase separated structure (or heterojunction) significantly improves the photovoltaic efficiency in polymeric devices [2, 55, 57].

One interesting system which have the potential to provide a ordered heterojunction structure for photovoltaic devices are the semiconducting block copolymers [2, 58, 59, 60]. Block copolymers are capable of undergoing self-assembly at the length scale of $\sim$ 10 nm [5]. The rigid rod-like conjugated polymer (donor) is covalently linked to a flexible block which is functionalized by fullerene (C_{60}) molecules which act as transport media for electrons [2]. It was shown that the donor-acceptor block copolymer showed enhanced photovoltaic efficiency relative to blend if its individual polymers (Refer Fig. 1.3) [2, 59]. The efficiencies are still on the lower side and there is a need to optimize the conjugate polymer (rod)-coil block copolymer to obtain better properties. Computational modeling is a powerful tool to study both the self-assembly of block copolymers as well as providing insights into the device physics of polymeric devices. Drift-diffusion models have been utilized earlier to study the photovoltaic properties of bilayer device [61], bulk heterojunction [62], and flexible block copolymers [58]. We build upon these models to understand the effect of self-assembly in rod-coil block copolymers on their photovoltaic

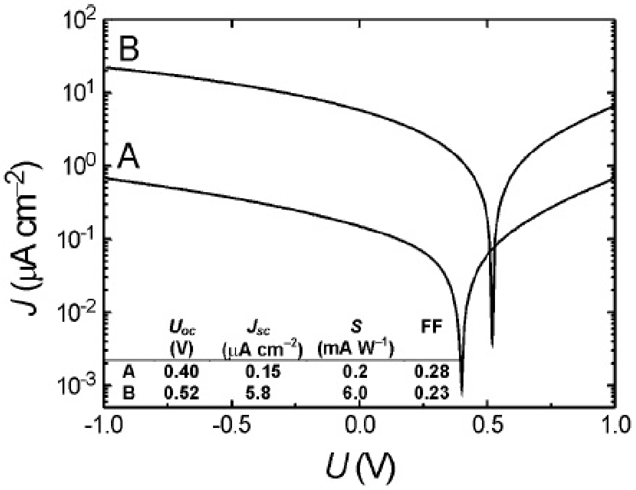

Figure 1.3: Current-voltage characteristics of donor-acceptor block copolymer (B) compared that with blend (A) of donor and acceptor. Both the short circuit current J_{SC}, and open circuit voltage V_{OC} are higher for the block copolymer as compared to the blend. (Adapted from Ref. [2])

properties. The goal is to optimize the self-assembly in thin films of rod-coil block copolymers to obtain high values of photovoltaic efficiencies. The morphologies of rod-coil block copolymers under confinement are obtained using self-consistent field theory as described in the previous section (Section. 1.1.4) [17, 18, 8]. Another major improvement in our model is that we consider the effect of anisotropic nature of the conjugate polymer on the mobility of charge carrier and exciton diffusivity. We relate the mobility of charge carriers to density of the two species and to the orientational ordering in conjugate rod molecules. The final photovoltaic properties depend upon the interplay of density inhomogeneities and anisotropic charge transport.

1.3 Thesis Organization

Chapter 2: Block Copolymer Thin Films in the Presence of Compressible Solvents [27]

In Chapter 2, we provide a theoretical framework to understand the role of compressible solvents like supercritical CO_2 on ordering and stability of symmetric diblock copolymer thin films. We combine a simple lattice-gas model for binary fluid mixtures to model compressible solvent and polymer mean field theory for block copolymer melts to study the stability of diblock copolymer thin films. Unlike previous models [25, 16] which consider physically confined thin films, we study the more experimentally relevant system of "supported" thin films in a bath of compressible fluid environment. Using a free energy analysis, we obtain the stable and unstable thicknesses for given solvent conditions. We study the onset of instability (dewetting of film into layered phases) in thin films as a function of solvent conditions and characterize it as Layered Dewetting Transition (LDT) [27]. Our results indicate the role of interplay of confinement, the compressibility of solvent, and its selectivity towards one block on ordering and stability of block copolymer thin films. Our simulation results can explain the contradictory phase behavior of diblock copolymer in bulk vs. thin film in presence of a compressible solvent.

Chapter 3: Side Chain Liquid Crystalline Block Copolymers [10]

In this Chapter, we focus on developing theoretical models to understand the phase behavior and thermodynamics of side chain liquid crystalline block copolymers. Our model is based on self-consistent field theory (SCFT) and we complement it with strong segregation theory (SST) to characterize the self assembly process in this class of complex polymers. Our model considers a micromechanical representation of flexible coil-coil block copolymers with rod-like units grafted to one of the blocks. Our model elucidates how microphase separation and liquid crystalline ordering interplay with each another to determine the final morphological structure. The morphological phase diagrams derived in this chapter are qualitatively consistent with the reported experimental results. We study the role of molecular weight of polymer, length of rodlike units, relative volume fractions of each block, and the energetic and orientational interaction on the self-assembly process. We utilize the SST model to provide a physical explanation for understanding our numerical simulation results.

Chapter 4: Mechanical Properties of Semicrystalline Multiblock Copolymers [21] To study structure development in semicrystalline diblock copolymer, we utilized a model based in self-consistent field theory to evaluate the phase behavior. Our model treats the flexible chain as Gaussian chain, and the crystalline chain as a semiflexible chain with temperature dependent rigidity and orientational interactions between parallel bonds in order to mimic crystallization in rigid chains. We obtain that rigidity of chain of one of the blocks can significantly change domain spacing as compared to flexible coil-coil diblock copolymers. We show scaling arguments to justify our numerical results on domain scaling as a function of crystallinity (rigidity) and compare the scaling analysis with previous theories and experimental results.

Extending the SCFT framework developed for semicrystalline diblock copolymers, we study structure development in various architectures (ABA, BAB, ABABA, BABAB) of semicrystalline triblock and pentablock copolymers. where A is the flexible block and B is the crystalline block. We utilize SCFT to evaluate the bridging fractions in various domains of these multiblock copolymers. The impact of crystallinity (rigidity) of one of the blocks and the sequence of multiblock copolymers on the bridging fractions is evaluated. Based on these numerical simulations, we can provide a strategy to optimize the toughness in such materials.

Chapter 5: Thin Films of Rod-Coil Block Copolymers In this Chapter, we extend the formalism of Prymatisyn et al. [8] to study the self-assembly mechanism in thin films of rod-coil block copolymers. We study the role of confining surfaces and thickness of film on the morphology of block copolymer and the orientation of rigid rod units. The phase behavior is compared with respect to bulk behavior of rod-coil block copolymers. We also research the nature of surface potentials and the different types of boundary conditions under the SCFT framework required to study the transition between parallel lamellae and perpendicular lamellae.

Chapter 6: Morphology Property Correlations of Rod-Coil Block Copolymers for Photovoltaic Applications We utilize the thin film morphologies obtained for rod-coil block copolymers (from Chapter 5) to study their photovoltaic properties. The charge carrier mobilities and exciton mobility are intricately linked to the density variations of rod and coil blocks and also to the orientational ordering of the conjugated rod block. We present a generalization of drift-diffusion model to allow for potential anisotropy in charge and exciton transport. We study the role of nature of morphology, the domain size, domain orientation, degree of phase separation, and anisotropic charge transport on eventual photovoltaic properties. We provide guidelines to optimize the self-assembly in confined films of rod-coil block copolymers to obtain high values of photovoltaic current in such devices.

Chapter 2

Block Copolymer Thin Films in Presence of Compressible Solvents

2.1 Introduction

Thermodynamics of block copolymer systems have been the subject of extensive studies from both technological as well as fundamental viewpoints [5]. For A-*b*-B diblock copolymers, the self-assembly behavior has been well-characterized and is determined by the fraction of A monomers (f), and by the incompatibility of the different blocks, quantified by $\chi_{AB}N$, where χ_{AB} denotes the Flory-Huggins interaction parameter between A and B blocks and N the degree of polymerization ($\chi_{AB} \propto 1/T$, where T denotes the temperature) [5]. Below the temperature corresponding to order-disorder transition (ODT), diblock copolymers phase separate into ordered structures consisting of A-rich and B-rich phases [5]. The influence of a variety of external conditions on the phase morphology of diblock copolymers have also been studied. Addition of good or neutral solvents to block copolymers have been shown to reduce the ODT, an effect rationalized as due to the dilution of the A-B contacts [63, 64].

The influence of confining surfaces has also been studied, for which the phase morphology of block copolymer melts have been shown to be influenced by both the interactions with the confining surfaces and the thickness of the film [65, 15, 14, 25, 66].

Recently, significant attention has been directed towards the use of compressible solvent media such as supercritical CO_2 as an environmentally benign option for polymer synthesis and processing [67, 23, 24]. A unique feature of such fluids is that the solvent density and its “quality” for the polymer can be varied by changes in compressibility resulting from external conditions such as pressure and temperature [68]. In diblock copolymer systems which exhibit an upper critical order-disorder temperature (UODT, i.e. order upon cooling), the solvent has been shown to screen the unfavorable enthalpic interactions between dissimilar polymer segments, reducing the ODT and leading to a phase mixing of the system [23, 24]. In the systems which exhibit a lower disorder-order temperature (LDOT, i.e. order upon heating), compressible solvents have been demonstrated to change the ODT significantly due to a differential dilation of the copolymer segments [23].

The present work was motivated by recent experimental observations by Arceo et al. [14] which demonstrated that in the presence of compressible, supercritical CO_2, the ODT of thin films of the diblock copolymer PS-*b*-PMMA (a UODT system) is enhanced significantly relative to the bulk ODT. At a given value of $\chi_{AB}N$, for which the bulk system was in the disordered phase, they observed that the thin film broke up into a terraced morphology with a second layer of finite thickness supported on a brush layer on the substrate. They equated the formation of such a terraced topography of islands and holes as a lowering of the ODT of thin films relative to bulk. To understand the mechanisms governing these observations, in this work we examine the hypothesis that under confinement, the compressibility of the solvent can interplay strongly with other influences such as the solvent selectivity leading to nontrivial changes in stability of thin films. With this motivation, in this chapter we use a numerical mean-field approach to study the onset of instability (dewetting of film into layered phases) in thin (confined) polymer films supported on neutrally selective substrate in the presence of a selective, compressible solvent. We term this instability temperature in block copolymer thin films as "layered dewetting temperature (LDT)" (to distinguish from ODT, a term synonymous with a sharp ordering transition). We specifically consider only the case of a symmetric diblock copolymer, and use a one-dimensional calculation to probe the stability in thin film systems and onset of formation of *parallel* lamellar phases in the bulk systems.

2.2 Description of Theoretical Framework

A novel theoretical approach is utilized to study the phase and stability behavior of block copolymer thin films in presence of compressible solvent. Unlike many previous studies considering phase behavior in physically "confined" systems, [25, 16] our framework considers a model of the more realistic "supported film" of diblock copolymers in a bath of compressible fluid environment

[69]. We consider a mixture of diblock copolymers and a compressible solvent in a semi-infinite system, where the solvent is a poor solvent for the copolymer (and hence they phase separate), and the copolymer units have attractive interactions with the substrate (and hence they segregate towards the substrate). These characteristics mimic very closely the experimental situation of Arceo et al., [14] where they studied phase behavior of PS-*b*-PMMA diblock copolymer film in the presence of supercritical CO_2, which is a poor solvent for both the blocks. In addition, CO_2 has a preferential interactions with one of the blocks (PMMA), an effect incorporated by introducing a relative solvent selectivity for one of the blocks. Our system differs slightly from the experiments of Arceo et al., in that the experimental conditions involved a substrate which had preferential interactions with one of the components. In contrast, to minimize the number of parameters in our model, we limit ourselves to the situation where the substrate is symmetric with respect to its interactions with the blocks.

2.2.1 Model for Compressible Solvent

The solvent phase is assumed to be compressible, and its equation of state is modeled using an incompressible, binary solvent-void mixture, where the volume fraction of the solvent varies in response to the external pressure. We use a lattice-gas model for the binary solvent(S)-void(V) mixture with the incompatibility between them denoted as χ_{SV} [70, 71]. This model has a simple analytical equation of state which enables us to relate its chemical potential

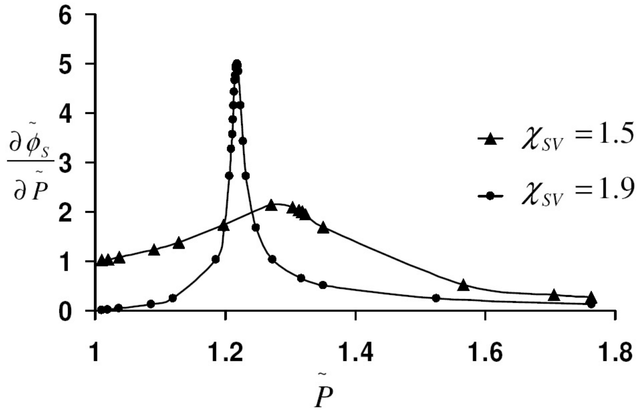

Figure 2.1: Plot of $d\tilde{\phi}_S/dP$ vs P. The peak is sharper and higher for $\chi_{SV} = 1.9$ than for $\chi_{SV} = 1.5$. $\chi_{SV} = 1.9$ is closer to the critical point.

and compressibility to the external conditions such as pressure and temperature (i.e. $1/\chi_{SV}$). Explicitly, if we consider a binary mixture of a solvent and voids with the identical monomeric volumes denoted ρ^{-1}, the activity coefficient z of the solvent can be obtained as:

$$\ln z = \ln \frac{\tilde{\phi}_S}{1 - \tilde{\phi}_S} + \chi_{SV}(1 - 2\tilde{\phi}_S), \tag{2.1}$$

where $\tilde{\phi}_S$ denotes the volume fraction of the solvent. The dimensionless pressure (denoted $\tilde{P}$) and isothermal compressibility (κ_T) are obtained by using thermodynamic definitions as:

$$\tilde{P} = \frac{P}{\rho k_B T} = 1 - \chi_{SV}\tilde{\phi}_S^2 - \ln(1 - \tilde{\phi}_S), \tag{2.2}$$

$$\tilde{\kappa}_T = \frac{\kappa_T}{1/\rho k_B T} = \frac{1 - \tilde{\phi}_S}{\tilde{\phi}_S[1 - 2\chi_{SV}(1 - \tilde{\phi}_S)\tilde{\phi}_S]}. \tag{2.3}$$

To illustrate the qualitative features of the above model, in Fig. 3.1 we display the quantity $d\tilde{\phi}_S/dP$ (proportional to the compressibility of solvent) as a function of pressure for different values of χ_{SV}. We observe that $d\tilde{\phi}_S/dP$ increases with an increase in the pressure P, reaches a maximum and then decreases thereafter. This manifestation of an intervening maximum is commonly termed the "density fluctuation ridge" in the literature, [68, 72] and has also been observed in the fluid properties of CO_2. It is evident from the Fig 3.1 that the "ridge" is more pronounced for the case of $\chi_{SV} = 1.9$ which is closer to the critical point as compared to $\chi_{SV} = 1.5$ (for our lattice-gas model, the critical point corresponds to $\chi_{SV} = 2.0$ and $\tilde{P} = 1.193$). This behavior is again qualitatively consistent with previous experimental work involving supercritical CO_2 [68, 73].

2.2.2 SCFT framework

The above model for the compressible solvent is combined with mean-field theory for block copolymers [25, 16] to analyze the stability of block copolymer films exposed to a bath of the solvent. For this, we consider an *incompressible* mixture of solvent, voids and block copolymers in a *semi-grand canonical ensemble*, where the solvent activity coefficient and the total number of block copolymers are constrained to specified values. We consider symmetric A-*b*-B diblock copolymers ($f = 0.5$), and denote by n and ϕ the number of chains and the the volume fraction of the block copolymers relative to the total volume of the system. The degree of polymerization of block copolymer is denoted as N.

It is assumed that both A and B components have the same statistical length b, and that their segments occupy the same volume $\rho^{-1} = b^3$ as that of the solvent and voids. All lengths are non-dimensionalized by the radius of gyration R_g of the copolymer. The polymer-solvent and polymer-void interactions are chosen to be identical and is denoted as χ_{SP}^{+}. These interactions are chosen to model a highly incompatible polymer-solvent mixture which brings about phase separation between polymer-rich and solvent-rich phases [26]. However, the solvent is also assumed to be relatively selective to one of the polymer segments (assumed to be the A segment), with the solvent selectivity quantified by a parameter denoted χ_{SP}^{-}. Negative values of χ_{SP}^{-} models the preferential affinity of the solvent towards the A-segments. The void is assumed to be non-preferential to either of the block copolymer components. Both segments of diblock copolymer are assumed to have identical interactions with the substrate, which corresponds to neutrally interacting walls.

In a mean-field approximation, the free energy (expressed on a per diblock chain basis) for the thin film of block copolymer-compressible solvent mixture can be written as:

$$
\begin{aligned}
F/nk_BT = &-\ln \mathcal{Q}[W_A, W_B] - \frac{zN}{\phi}\mathcal{Q}_S[W_S] + \frac{1}{\phi V}\int d\mathbf{r}\{\chi_{AB}N\Phi_A(\mathbf{r})\Phi_B(\mathbf{r}) \\
&+ \chi_{SP}^{+}N(\Phi_S(\mathbf{r}) + \Phi_V(\mathbf{r}))(\Phi_A(\mathbf{r}) + \Phi_B(\mathbf{r})) + \chi_{SP}^{-}N\Phi_S(\mathbf{r})(\Phi_A(\mathbf{r}) - \Phi_B(\mathbf{r})) \\
&+ \chi_{SV}N\Phi_S(\mathbf{r})(1 - \Phi_A(\mathbf{r}) - \Phi_B(\mathbf{r}) - \Phi_S(\mathbf{r})) - N(H_A(\mathbf{r})\Phi_A(\mathbf{r}) + H_B(\mathbf{r})\Phi_B(\mathbf{r})) \\
&- (W_A(\mathbf{r})\Phi_A(\mathbf{r}) + W_B(\mathbf{r})\Phi_B(\mathbf{r}) + W_S(\mathbf{r})\Phi_S(\mathbf{r})) + N(1 - \Phi_A(\mathbf{r}) - \Phi_B(\mathbf{r}) - \Phi_S(\mathbf{r})) \\
&\times [\ln(1 - \Phi_A(\mathbf{r}) - \Phi_B(\mathbf{r}) - \Phi_S(\mathbf{r})) - 1]\}.
\end{aligned}
\tag{2.4}
$$

In the above equation, $\Phi_A(\mathbf{r})$, $\Phi_B(\mathbf{r})$, $\Phi_S(\mathbf{r})$, and $\Phi_V(\mathbf{r})$ represent the local volume fractions of A, B, S and V respectively. The potential fields acting on the A, B segments and the S molecules are denoted by $W_A(\mathbf{r})$, $W_B(\mathbf{r})$ and $W_S(\mathbf{r})$ respectively. $\mathcal{Q}$ is the partition function of a single polymer chain in the external fields $W_A(\mathbf{r})$ and $W_B(\mathbf{r})$, and $\mathcal{Q}_S$ is the partition function of a solvent molecule in external potential field $W_S(\mathbf{r})$. The surface potential fields are denoted by $H_i(\mathbf{r})$, where $i = A$ and B. These functionals are chosen to be identical in form to that proposed by Matsen [16]. The surface potential is applied only on the lower wall (i.e. substrate), so that the block polymer is attracted to the substrate. The final term in the free energy equation is the translational entropy contribution due to the presence of voids.

$\mathcal{Q}$ stands for the partition function of a single diblock chain in the external fields $W_A(\mathbf{r})$ and $W_B(\mathbf{r})$, and is given as

$$\mathcal{Q} = \frac{1}{V}\int d\mathbf{r}q(\mathbf{r},1) \tag{2.5}$$

where, $q(\mathbf{r},s)$ is the end-segment distribution function that gives the probability that a section of a polymer chain, of length 's' and containing a free chain end has its connected end at $\mathbf{r}$. This distribution function satisfies the modified diffusion function [25, 16, 18].

$$\frac{\partial}{\partial s}q(\mathbf{r},s) = \begin{cases} \nabla^2 q(\mathbf{r},s) - W_A(\mathbf{r})q(\mathbf{r},s) & \text{if } 0 \leq s \leq f \\ \nabla^2 q(\mathbf{r},s) - W_B(\mathbf{r})q(\mathbf{r},s) & \text{if } f \leq s \leq 1 \end{cases} \tag{2.6}$$

$\mathcal{Q}_S$ is the partition function of a single solvent molecule in the external potential field $W_S(\mathbf{r})$.

$$\mathcal{Q}_S = \frac{1}{V}\int d\mathbf{r}\exp\left(-\frac{W_S(\mathbf{r})}{N}\right) \tag{2.7}$$

The surface potential of A-segments and B-segments ($H_A(\mathbf{r})$ and $H_B(\mathbf{r})$) are applied only on the substrate wall. The functional form of surface field $H_i(\mathbf{r})$ ($i = A$ or B) is chosen as

$$H_i(\mathbf{r}) = \begin{cases} \Lambda_i(1+\cos(\pi x/\epsilon))/\epsilon & \text{if } 0 \leq x \leq \epsilon \\ 0 & \text{if } \epsilon \leq x \end{cases} \tag{2.8}$$

In the above equation, Λ_A and Λ_B control the strength of surface potential fields for A-segments and B-segments respectively. ϵ is the width of "surface layer" - the region over which the surface potential field acts. For a positive value of Λ_i, the surface has affinity for that particular polymer component.

In the mean-field approximation, the segment densities and potential fields are determined by a set of self consistent equations [25, 16, 18, 17]. The densities and potential fields are replaced by their saddle points for which the value of free energy functional is minimum. These equations are obtained by taking the functional derivative of free energy with respect to each of the density and potential fields and equating them to zero. These resulting self-consistent equations are laid out below :

$$\Phi_A(\mathbf{r}) = -\phi V \frac{\mathcal{D}\mathcal{Q}}{\mathcal{D}W_A} \tag{2.9}$$

$$\Phi_B(\mathbf{r}) = -\phi V \frac{\mathcal{D}\mathcal{Q}}{\mathcal{D}W_B} \tag{2.10}$$

$$\Phi_S(\mathbf{r}) = z\exp\left(-\frac{W_S(\mathbf{r})}{N}\right) \tag{2.11}$$

$$\begin{aligned} W_A(\mathbf{r}) = {} & \chi_{AB}N\Phi_B(\mathbf{r}) + (\chi_{SP}^{+}N + \chi_{SP}^{-}N)\Phi_S(\mathbf{r}) - \chi_{SV}N\Phi_S(\mathbf{r}) - NH_A(\mathbf{r}) \\ & - N\ln(1 - \Phi_A(\mathbf{r}) - \Phi_B(\mathbf{r}) - \Phi_S(\mathbf{r})) \end{aligned} \tag{2.12}$$

$$\begin{aligned} W_B(\mathbf{r}) = {} & \chi_{AB}N\Phi_A(\mathbf{r}) + (\chi_{SP}^{+}N - \chi_{SP}^{-}N)\Phi_S(\mathbf{r}) - \chi_{SV}N\Phi_S(\mathbf{r}) - NH_B(\mathbf{r}) \\ & - N\ln(1 - \Phi_A(\mathbf{r}) - \Phi_B(\mathbf{r}) - \Phi_S(\mathbf{r})) \end{aligned} \tag{2.13}$$

$$W_S(\mathbf{r}) = \chi_{SP}^{+} N(\Phi_A(\mathbf{r}) + \Phi_B(\mathbf{r})) + \chi_{SP}^{-} N(\Phi_A(\mathbf{r}) - \Phi_B(\mathbf{r})) + \chi_{SV} N(1 - 2\Phi_S(\mathbf{r}) - \Phi_A(\mathbf{r}) - \Phi_B(\mathbf{r})) - N \ln(1 - \Phi_A(\mathbf{r}) - \Phi_B(\mathbf{r}) - \Phi_S(\mathbf{r})) \tag{2.14}$$

To model the influence of the substrate boundary upon the polymer conformations, Dirichlet boundary condition is applied for the end-segment distribution function of the polymer conformations. The semi-infinite nature of film is modeled by a Neumann condition on the other boundary [26]. To model bulk phase behavior of the block copolymer-solvent mixture, periodic boundary conditions are applied. To numerically implement SCFT, the system is divided into a 1-D lattice. Starting with a set of random values for potential fields $W_i(\mathbf{r})$, the segment densities and potential fields are evolved using the above self-consistent equations. At equilibrium, the value of free energy is minimum. The partition function for diblock copolymer, $\mathcal{Q}$ and the segment densities are calculated by solving the modified diffusion equation. A fourth order accurate Adams-Bashford algorithm is utilized to solve this partial differential equation [74]. For the case of bulk systems, periodic boundary condition is applied, while for thin films, $q(\mathbf{r}, s) = 0$ is applied on the substrate and $dq/dr = 0$ at the other end. We utilized the following values for discretization in space $\Delta x = 0.05R_g$ and a step-size of $\Delta s = 0.0025$. Each run took approximately 2 hours of computer time to achieve convergence of 10^{-5} in the value of free energy per chain.

2.3 Free energy analysis

In our semi-grand canonical framework, the thickness (Δ) of the copolymer film is not an externally controllable quantity. the thickness of the block copolymer film is not a specified quantity, but is rather determined by the equilibrium conditions corresponding to the solvent-polymer phase equilibrium. To extract the free energy per unit area corresponding to the block copolymer film, we follow the following procedure: For given solvent conditions and A-B interactions ($\chi_{AB}N$), the free energy per unit area of the film is dependent on the thickness x of the slab of the block copolymer film considered. In Figure 3.2, we display a representative plot for this dependence of the free energy per unit area (denoted by F') as a function of x. It is observed that when the slab of material considered falls wholly within the diblock copolymer film, F' is an oscillatory function of x (mimicking the composition profile within the film), whereas for the situation where the slab considered falls in the solvent rich phase F' varies linearly with x. The latter embodies the contributions arising from the free energy per unit area of the block copolymer film (a x independent quantity), and the free energy contribution arising from the solvent-void interactions (which is extensive and scales linearly with x). A linear fitting was used to extract these independent contributions to F'. This is shown in the inset of Figure 3.2, which displays the “linear” region of the F'. Explicitly, we represent

$$F' = F + F_S x, \tag{2.15}$$

where F_S represents the free energy of solvent-void phase per unit length and F represents the surface energy of the film per unit area. We used this (intercept) F as the surface free energy for our subsequent analysis.

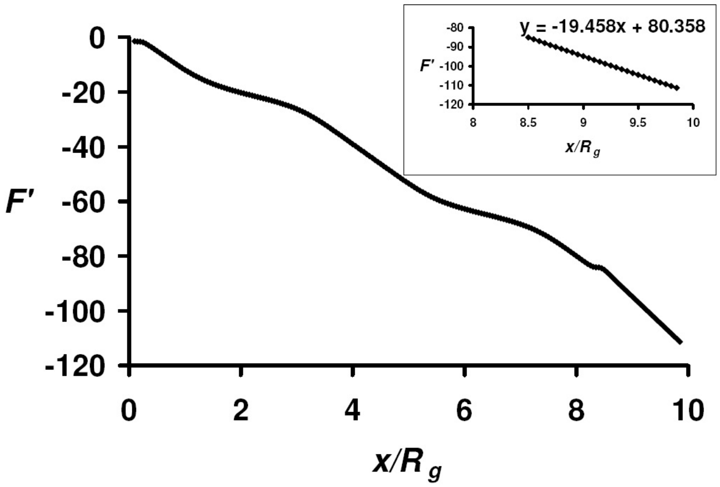

Figure 2.2: Free energy per unit area of the film as a function of x - distance from the substrate. The value of Flory-Huggins interaction parameter is $\chi_{AB}N = 12$ and the volume fraction of copolymer is $\phi = 0.35$. The solvent condition is fixed corresponding to $\chi_{SV} = 1.9$, $z = 1.2118$, $\tilde{P} = 1.35$, $\chi_{\bar{S}P}N = -25$.

We now briefly review the manner in which F determines the onset of instabilities in block copolymer thin films. It is well known that for solvent-free block copolymer melts, the presence of a substrate which exhibits preferential selectivity to one of the segments, induces exponentially decaying composition oscillations even when the temperature is above the bulk ODT [66, 75, 22]. When the block copolymer is confined between two such substrates, interference of such concentration oscillations induced by the surfaces leads to a thickness dependence of the overall free energy of the film, [65, 14, 66] and can lead to macroscopic dewetting instabilities where the film breaks up into a discontinuous layer forming ‘islands’ and ‘holes’ [65, 14, 76, 15, 77]. The criteria for instability to develop in a thin film of thickness (Δ) is expressed in terms of second derivative of free energy with respect to thickness: [66]

$$\frac{\partial^2 F}{\partial \Delta^2} < 0 \tag{2.16}$$

In contrast, for temperatures below the bulk ODT, the free energy of the thin film system exhibits periodic oscillations as a function of the film thickness. The minima of the free energy-thickness dependencies correspond to the stable thicknesses while the maxima correspond to the unstable thicknesses.

In our study, we consider neutrally selective surfaces and probe the effect of the selective solvent upon instability and ordering in thin films. In contrast to the above discussed situation (for selective surfaces), for solvent-free block copolymer melts in the presence of neutrally selective surfaces, there are no free energy oscillations induced in the film at temperatures above the bulk ODT. However, for temperatures below the ODT, the free energy of the thin film system does exhibit periodic oscillations as a function of the film thickness, with the minima corresponding to the stable thicknesses while the maxima correspond to the unstable thicknesses. To compare with this expectation, Figure 3.3 displays the dependence of the free energy per unit area (F) of our solvent+block copolymer film as a function of the amount of copolymer present inside the film (denoted Φ_P, determined in a manner similar to F and

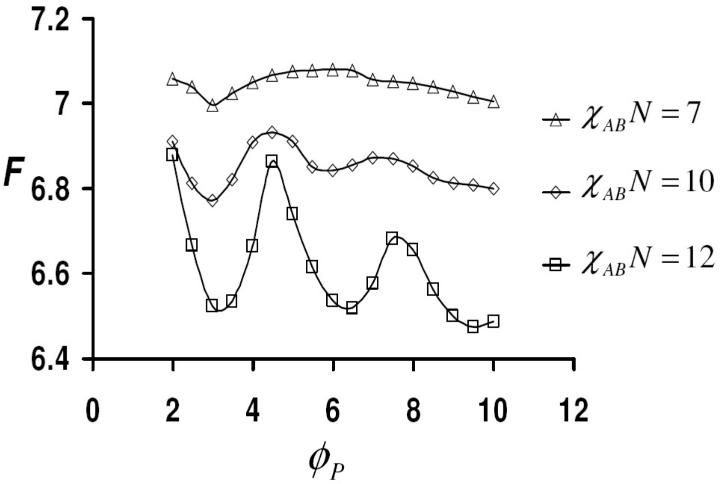

Figure 2.3: Free energy as a function of total polymer concentration Φ_P for three different values of $\chi_{AB}N$.The solvent condition is fixed corresponding to $\chi_{SV} = 1.0$, $z = 0.814$, $\tilde{P} = 1.35$, $\chi_{SP}^{-}N = -25$. These values of F are corrected with the bulk value of free energy

is taken as a measure of the thickness of the film) for three different values of Flory-Huggins parameter $\chi_{AB}N$. The solvent conditions are fixed such that the parameters: $\chi_{SV} = 1.0$, $z = 0.814$, $\tilde{P} = 1.35$, and $\chi_{SP}^{-}N = -25$.

Overall, the trends evident in Fig. 3.3 are similar to the behavior expected for a pure block copolymer melt near a selective substrate. In Figure 3.3, for $\chi_{AB}N = 7$, we observe only one minimum ($\Delta_{\min}$) in the free energy profile, corresponding to the stable thickness. For thickness smaller than $\Delta_{\min}$, holes appear on the surface coexisting with regions of thickness $\Delta = \Delta_{\min}$ [65]. For thickness larger than $\Delta_{\min}$, the film would prefer breaking into a region of minimum stable thickness and a region of infinite thickness, corresponding to macroscopic dewetting. The second case ($\chi_{AB}N = 10$) corresponds to a diblock copolymer film near its layered dewetting temperature (LDT, defined below), where the second minimum in the free energy thickness dependence gets more pronounced. For the case of $\chi_{AB}N = 12$, the free energy dependence on film thickness exhibits periodic oscillations, indicative of ordering in thin films. The minima in this curve correspond to stable thicknesses involving different numbers of A-B layers, while the interspersed maxima correspond to unstable thicknesses. For thickness intermediate between two minima, common tangent construction can be used to determine the breakup of a film into regions of stable thicknesses. Such a framework ensures the equality of chemical potential of both the block copolymer and the solvent in the coexisting thicknesses.

In the results presented below, we interpret LDT as the $\chi_{AB}N$ at which a periodic double-well minimum appears in the free energy-thickness dependence plot. This criterion identifies the $\chi_{AB}N$ for which films intermediate in thickness to the minima breaks up into coexisting thicknesses corresponding to the minima. In the experimental results corresponding to our study, the breaking up of the unstable film into such layers of periodic thicknesses was construed as an indication of self-organization within the film, and was identified as the ODT of the thin film by Arceo et al. [14]. Based on such an identification, we study the effect of solvent properties on the LDT. Due to the number of components and their interactions, the above model has a vast parameter space with potentially rich behavior. To render the parameter space manageable, we fix the degree of polymerization at $N = 100$. The size of the overall system is fixed at $\Delta' = 20R_g$, where R_g is the radius of gyration of the copolymer. The value of the following polymer-void and polymer-solvent repulsive interaction parameter is kept fixed: $\chi^+_{SP} = 2.0$. In this work, we focus on the interplay between compressibility, density fluctuation effects of the solvent and other physical conditions such as solvent selectivity (χ^-_{SP}) upon the thin film phase behavior.

2.4 Results

In Figure 3.4a we compare the differences in phase behavior between the thin film and bulk systems in the presence of compressible solvent. For a specified value of relative solvent selectivity $\chi^-_{SP}N$ and the solvent-void interaction parameter χ_{SV}, it is observed that the LDT in thin films occurs at a lower value of $\chi_{AB}N$ compared to the corresponding bulk system ODT. Moreover, with increasing pressure, this layered dewetting transition is also seen to be shifted to lower values of $\chi_{AB}N$. In Figure 3.4a, the comparison between thin film and bulk systems is presented for two different values of χ_{SV}, from which it is observed that increasing χ_{SV} also lowers the value of $\chi_{AB}N$ for onset of instability. It is pertinent to note our results suggest that the layered dewetting transition for thin films can occur at $\chi_{AB}N$ values lower than both the conditions at which the block copolymer solvent mixture orders in bulk as well as the ordering temperature of a thin film of pure block copolymer orders in vacuum ($\chi_{AB}N = 10.5$). This result is qualitatively consistent with experimental observations of Arceo et al., that the ordering transition temperature of block copolymer thin film increases relative to bulk in the presence of slightly selective supercritical CO_2 solvent [14].

To rationalize the above results, we note that in contrast to the situation for neutral (non-selective) solvents discussed earlier, [63, 64] a selective solvent can lead to a preferential swelling of one of the components relative to the other, leading to an effectively enhanced repulsion between the blocks. Indeed, it has been found that a highly selective solvent can lead to ordering in block copolymer at lower values of $\chi_{AB}N$ than even the pure block copolymer [63]. Our results are rationalized by noting that for a specified solvent condition, the amount of solvent inside the copolymer thin film is higher than that of the corresponding bulk system. For thin films, the polymer density vanishes at the substrate, and there is an increase in solvent density both near the substrate and at the polymer-vapor interface due to entropic considerations [69].

The solvent effect is clearly demonstrated in Figure 3.4b, where the total solvent volume fraction (Φ_S) in the film is plotted as a function of pressure for the cases considered in Figure 3.4a. For a given χ_{SV}, it is seen that the solvent volume fraction is always higher in the thin film ($\phi = 0.15$) as compared to its bulk analog. Since in our study, the solvent is relatively preferential to A-segments, the A-block is "pulled" towards both the substrate and the free surface. So even in the absence of a preferential surface potential, the presence of a selective solvent creates effectively an enhanced pseudo-repulsion between the A and B copolymer segments. We implicate the solvent sorption and selectivity induced enhanced repulsion to be responsible for earlier observation

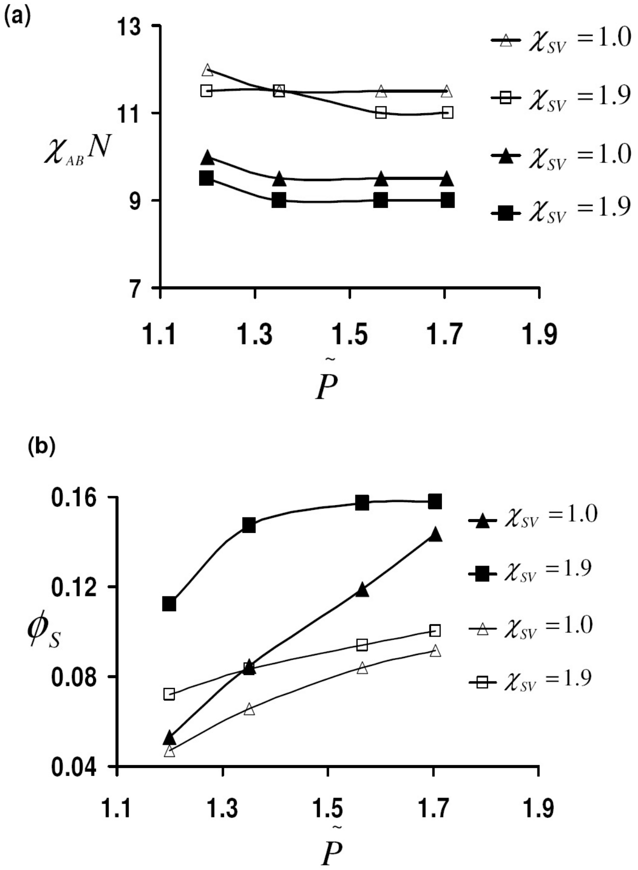

Figure 2.4: (a) The LDT (thin film systems, closed symbols) and ODT (bulk systems, open symbols) $\chi_{AB}N$ versus pressure ($\tilde{P}$) for. (b) The solvent volume fraction Φ_S *vs.* pressure for the cases shown in Part (a). The volume fraction of the block copolymer relative to the total volume of the system is fixed at $\phi = 0.15$.

of instability in thin films.

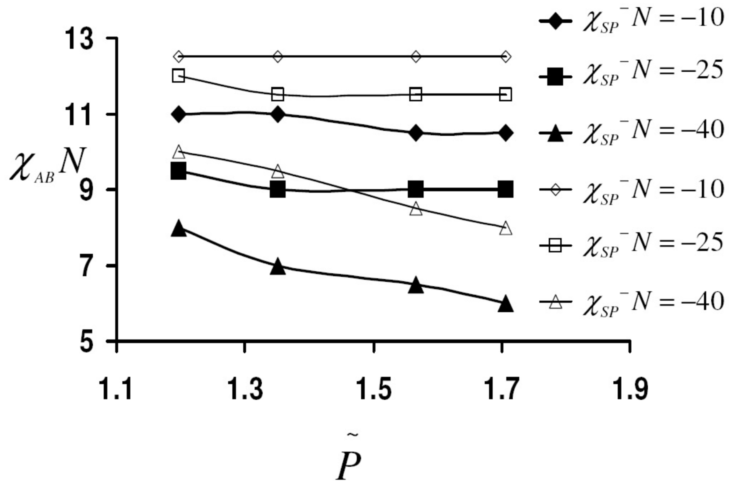

Figure 2.5: The LDT (thin film systems, closed symbols) and ODT (bulk systems, open symbols) $\chi_{AB}N$ as a function of pressure $\tilde{P}$ for different values of $\chi_{SP}^{-}N$ in thin film (closed symbols) and bulk systems (open symbols). The value of χ_{SV} is fixed at 1.5.

The effects of χ_{SV} and external pressure on the phase behavior in thin films can now be explained. We note that χ_{SV} reflects the distance of supercritical fluid from critical conditions, with the critical temperature corresponding to a value of $\chi_{SV} = 2.0$. The amount of solvent intake into the film is directly related to the value of solvent activity coefficient (z), which in turn is directly proportional to the volume fraction of solvent in the solvent-void phase. At a given value of solvent pressure, increasing χ_{SV} increases the repulsive interactions between solvent and voids, and hence, the volume fraction of solvent in the supercritical solvent phase increases. This correspondingly enhances the amount of solvent sorption in the film. This effect is shown in Figure 3.4b, where at a given pressure, the amount solvent sorption is higher for $\chi_{SV} = 1.9$ than for $\chi_{SV} = 1.0$ for both bulk and thin film system. Since the value of $\chi_{AB}N$ for which ordering occurs in thin film is a function of the amount of solvent inside the film, it is clear that increasing χ_{SV} shifts the layered dewetting temperature to lower values of $\chi_{AB}N$ (Figure 3.4). Along similar lines, at a given χ_{SV}, higher pressure implies lower compressibility, and hence the volume fraction of solvent in the supercritical phase (and the amount of solvent absorbed in the film) is higher. Therefore, increasing pressure leads to lowering of the layered dewetting temperature, albeit this shift is not substantial.

The above results indicate that the relative selectivity of a solvent can also play an important role in this instability of block copolymer thin films. These effects are clearly displayed in Figure 2.5, where it is seen that increasing the selectivity of solvent can shift the ordering transition to much lower values of $\chi_{AB}N$. While a similar trend is also observed for bulk systems, the shift in ordering transitions are more significant for thin films as compared to bulk (Figure 2.5). These trends are again consistent with our earlier discussion on the interplay between larger sorption of solvent and relative selectivity to one block. Increasing the solvent selectivity renders this effect more pronounced, leading to larger shifts in ordering transitions in thin films.

2.5 Conclusions

In summary, we employed self-consistent mean field theory in combination with a lattice gas model for a compressible solvent to examine the phase behavior and stability of thin films and bulk systems in the presence of a compressible fluid. Our formalism considers a supported film rather than that of a confined one as considered in many prior researches. This framework allows for a more realistic approach to study the stability in thin film morphologies. A free-energy analysis was used to analyze the stability and layered dewetting transitions occurring in diblock copolymer thin films. Our results are in qualitative agreement with experimental results [14] which demonstrated that there is an upward shift of the thin film layered dewetting temperature relative to the bulk ODT in a compressible solvent environment. These experiments were rationalized by suggesting that compressible solvent enhances the disparity in interactions between different diblock segments in thin films more than bulk, leading to significant differences in phase transitions. This reasoning is consistent with our results that the relative selectivity has a very important effect on the phase behavior of the block copolymers. These effects suggest that the interplay of solvent properties and confinement can lead to a richer phase behavior for block copolymer systems, thereby opening up the possibility for another parametric control of the self-assembly morphologies in such systems.

Chapter 3

Self-Assembly of Side-Chain Liquid Crystalline Block Copolymers

3.1 Introduction

The self-assembly behavior of *flexible* diblock and multiblock copolymers have been extensively studied from both a theoretical and experimental viewpoint. Their morphological characteristics are known to be parameterized by the fraction of the different blocks and by the incompatibility between the different blocks. Some of the commonly observed self-assembled microstructures in such polymers include lamellar phases, hexagonally packed cylinders, body centered cubic spheres and bicontinuous gyroid phases [1]. In contrast, liquid crystalline polymers (LCP) are a special class of polymers possessing mesogenic units capable of orientational ordering in addition to morphological assembly. Such polymers have attracted significant attention in view of their potential applications in electro-optical display devices and high strength fibers [78]. The self-assembly characteristics of block copolymers containing such LC units are expected to be richer than flexible diblock copolymers due to the combined possibility of microphase separation along with orientational ordering of the segments. For instance, rod-coil diblock copolymers have displayed morphological characteristics distinct from that of conventional flexible block copolymer mesophases which includes phases such as arrowhead, zig-zag, wavy lamellar and smectic bilayers [8, 79, 80].

Side-chain liquid crystalline (SCLC) block copolymers are a special class of liquid crystalline polymers consisting of side-chain mesogenic units attached typically through an alkyl spacer to an amorphous backbone. Several experimental groups have synthesized and studied the properties of side chain liquid crystalline block copolymers [29, 81, 31, 30]. In contrast to the morphologies exhibited by rod-coil block copolymers, side-chain liquid crystalline block copolymers exhibit richer self-assembly characteristics that manifest an interplay between the backbone block copolymer ordering and liquid crystalline ordering between side chain rod units [82]. Overall, at low volume fractions of the amorphous coil block (i.e. the ungrafted flexible block), hexagonally closed packed cylinders of the coil phase have been observed inside a continuous matrix made of the LC block [31, 30, 3, 83, 84]. The rod segments were observed to be oriented parallel to the block copolymer interface and along the axis of the cylinders [83, 84]. Increasing the volume fraction of the amorphous coil block have been shown to lead initially to perforated lamellar morphologies (possibly metastable states), in which alternating lamellar phases are interspersed with cylindrical domains in which the coil block is confined [3]. In most experiments, further increase in the volume fraction of the coil block leads to a broad lamellar regime which persists up to relatively low volume fractions of the block on which the mesogens are grafted (hereafter referred to as LC block). Moreover, it has been observed that the lamellar domains typically stabilize the formation of Smectic C* phases where the orientation of the rod segments are parallel to the block copolymer interface [29, 9]. However, in some cases, especially when the rods are connected through a longer alkyl spacer to the main chain backbone, rod orientations perpendicular to the block copolymer interface have also been observed [9]. At high volume fractions of the amorphous coil block, cylindrical microdomains of LC blocks, with the mesogens parallel to the axis of cylinders have been observed [31]. Moreover in most of the experiments reported, orientational ordering of the rod segments occurs at or after the order-disorder transition (ODT) for the microphase separation, suggesting that the onset of compositional ordering significantly influences the orientational ordering of the rods.

In contrast to the significant theoretical developments accompanying self-assembly in flexible block copolymers, methods and models for predicting the self-assembly behavior of side chain liquid crystalline block copolymers are very limited. A scaling-based free energy model was developed for the side chain liquid crystalline block copolymers by Anthamatten and coworkers [85]. This model accounts for the orientational interaction of mesogens, stretching of the amorphous chains, surface tension of the interfaces between the incompatible blocks and the elastic deformation of the LC phase [85]. Free energies were estimated for different morphologies and phase diagrams were constructed which were reported to be in qualitative agreement with the experiments. On a slightly different front, some theoretical models based on self-consistent field theory (SCFT) and random phase approximation (RPA) have considered the self-assembly characteristics of comb-coil block copolymers (which can be argued to be architecturally similar to side chain liquid crystalline block copolymers) [86, 87, 88]. The SCFT model considered the general case of combs grafted at arbitrary locations along the backbone. Due to computational limitations, such a model could only study the self-assembly behavior of the polymer with a few number of grafted units [86]. The RPA formalism on the other hand is limited to weak segregation regime, and requires one to consider known structures whose free energies are then compared [88]. Consequently, it is somewhat limited to "discover" structures in complex polymers such as SCLC multiblock copolymers.

In this chapter, we propose a combined study based on self-consistent mean field theory (SCFT) and strong segregation theory (SST) to understand the self-assembly characteristics of side chain liquid crystalline (SCLC) block copolymers. SST is analytical in nature and therefore identifies the physics behind the self-assembly characteristics. SST has been shown to be very successful in describing the phase behavior of diblock and multiblock copolymers accurately at stronger segregations [1, 89, 90]. For SCLC polymers, the strong segregation approximation we use is expected to be more accurate for relatively shorter rod molecules grafted to the main chain backbone. In contrast, the self-consistent mean field theory is numerical, but in principle is valid for all degrees of segregation and rod lengths. We view these methods as complementary, and use them together to provide a complete overview of the self-assembly behavior.

Figure 3.1(a) displays the molecular structure of a SCLC block copolymer used in the experiments of Hammond and coworkers, in which a styrene block is linked to a methacrylate block on which mesogenic chiral biphenyl benzoate molecules are grafted through an alkyl spacer [3]. Inspired by the structure of such molecules, we develop a SCFT model based on the micromechanical representation of the SCLC block copolymer as having a coil block (A) linked to another coil block (B). The monomers of the coil block (B) are assumed to be linked to each other through flexible spring like units. Each monomer of the B coil is also assumed to be attached to a mesogenic unit (R) (shown schematically in Figure 3.1(b)). As we demonstrate later, this approach eliminates the constraint of incorporating only a "few" grafted side chains (which typically increases the computational requirements), and instead models the experimental conditions more realistically. The SST model adopts a more simplistic view by ascribing the effect of rods to two contributions: (i) An increased monomeric volume of the B segments; (ii) The influence of changes in orientational entropies and interaction energies due to ordering of the rods within mesophases. These contributions are then combined with the classical theory of ordering in flexible diblock copolymers to discern the self-assembly characteristics in the system.

The rest of the chapter is organized as follows. In section II we demon-

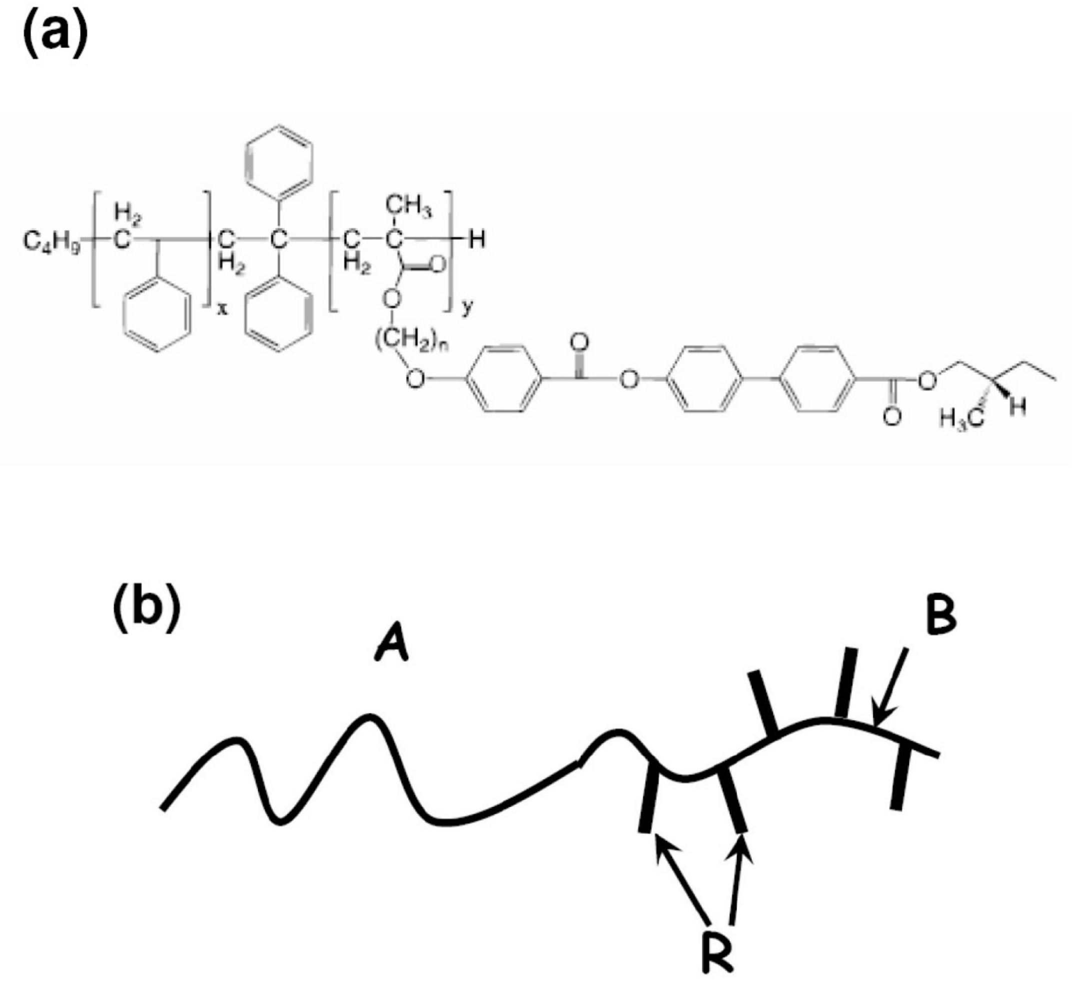

Figure 3.1: (a) Molecular structure of a SCLC copolymer used in the experiments of Hammond and coworkers [3]. (b) A schematic of our model for side chain liquid crystalline polymer. N_A monomers of A block is attached with a B block having N_R number of attached mesogenic units.

strate the manner in which the thermodynamical features of the above model can be recast into a field theory model which can be treated by mean-field approximation to lead to a self consistent field theory for SCLC block copolymer. In section III, we present results for the self-assembly characteristics by assuming two dimensional morphologies. Our results relate the morphological characteristics of SCLC block copolymers to various parameters such as its overall molecular weight, the length of the rod units, the volume fraction of each block and the orientational interaction between LC moieties. We explore a limited subset of the parametric space and we present results which are in good agreement with experimental results. These results suggest that our model provides a means to deduce the morphologies and orientational characteristics for other parametric conditions of SCLC block copolymer. In section IV we present a description of the model for SST calculations, the accompanying results and a comparison to the corresponding SCFT results.

3.2 Description of SCFT Model and Framework

In this section, we present a field theoretic formulation of the model for the side chain liquid crystalline diblock copolymer described in the introduction (Figure 3.1(b)). The theoretical framework parallels the earlier developments in models for flexible diblock copolymers and rod-coil copolymers [16, 8], however differing in the presence of side chain rod units at every monomer of one of the blocks.

We consider a canonical ensemble of an incompressible melt of n side chain liquid crystalline block copolymers in a volume V. Each polymer is assumed to be made of a block of a flexible chain (referred to as the A block) attached to another flexible block (B) to which the rod-like units (R) are attached. Closely modeling the experiments of SCLC polymers, we assume that side chain mesogenic units are attached to every monomer of the B block. Between two rod units, the backbone of the B polymer is modeled as a flexible Hookean spring. The monomeric units of the flexible coil (A and B) are both assumed to be characterized by the same statistical segment length b. For simplicity, we assume that both coil and rod monomers occupy the same volume (ρ_0^{-1}). Based on this assumption, we define the characteristic length of a rod monomer "a", such that $ad^2 = \rho_0^{-1}$ (d being the diameter of the rod). The rod unit is then assumed to contain "m" such monomers. This parameterization is identical to that employed in earlier models of rod-coil block copolymers [8, 91]. In this notation, if there are N_A monomers of A and N_R number of rod units (equal to number of B monomers), then the overall number of units of the SCLC polymer is

$$N = N_A + N_R(m+1) \tag{3.1}$$

The volume fraction of the amorphous block is denoted as f_A $(= N_A/N)$, and the volume fractions of the B and R monomers are denoted as f_B $(= N_R/N)$ and f_R $(= mN_R/N)$ respectively.

The flexible (A and B) parts of the copolymer are parameterized with a continuous variable "s" which monotonically increases along the length of the polymer. Explicitly, $s = 0$ at the beginning of A-block, $s = N_A$, at the junction of the two blocks and $s = N_A + N_R$ at the end of B block. Using this parameterization, the function $\mathbf{R}_\alpha(s)$ (where $\alpha = 1, 2, ..., n$ indexes the different polymers) is used to describe the conformations of the flexible A block and backbone monomers. Each rod block whose ends are at $\mathbf{R}_\alpha(s)$ ($N_A < s \leq N_A + N_R$), are assumed to be oriented along a unit orientational vector denoted as $\mathbf{u}_\alpha(s)$. Based on these notations, the non-dimensional volume fractions for A, B and R segments are denoted $\hat{\phi}_A(\mathbf{r})$, $\hat{\phi}_B(\mathbf{r})$, and $\hat{\phi}_R(\mathbf{r})$, and are defined as

$$\begin{aligned}
\hat{\phi}_A(\mathbf{r}) &= \frac{1}{\rho_0} \sum_{\alpha=1}^{n} \int_0^{N_A} ds\, \delta(\mathbf{r} - \mathbf{R}_\alpha(s)), \\
\hat{\phi}_B(\mathbf{r}) &= \frac{1}{\rho_0} \sum_{\alpha=1}^{n} \int_{N_A}^{N_A+N_R} ds\, \delta(\mathbf{r} - \mathbf{R}_\alpha(s)), \\
\hat{\phi}_R(\mathbf{r}) &= \frac{1}{\rho_0} \sum_{\alpha=1}^{n} \int_{N_A}^{N_A+N_R} ds \int_0^m dp\, \delta(\mathbf{r} - \mathbf{R}_\alpha(s) - ap\mathbf{u}_\alpha).
\end{aligned} \tag{3.2}$$

In addition, to describe the orientational interactions between the rods, we invoke an orientational order parameter $\hat{\mathbf{S}}(\mathbf{r})$ defined as:

$$\hat{\mathbf{S}}(\mathbf{r}) = \frac{1}{\rho_0} \sum_{\alpha=1}^{n} \int_{N_A}^{N_A+N_R} ds \int_0^m dp\, \delta(\mathbf{r} - \mathbf{R}_\alpha(s) - ap\mathbf{u}_\alpha) \left[\mathbf{u}_\alpha \mathbf{u}_\alpha - \frac{\mathbf{I}}{3}\right]. \tag{3.3}$$

The overall melt is assumed to be incompressible i.e.,

$$\hat{\phi}_A(\mathbf{r}) + \hat{\phi}_B(\mathbf{r}) + \hat{\phi}_R(\mathbf{r}) = 1. \tag{3.4}$$

Energetic interactions in the above model are assumed to be comprised of the following components: (i) Stretching free energy of the flexible chain ($H_0(\mathbf{R})$): Within the Gaussian chain model, this is given as: [8, 92]

$$H_0[\mathbf{R}] = \frac{3}{2b^2} \sum_{\alpha=1}^{n} \int_0^{N_A+N_R} ds \left| \frac{d\mathbf{R}_\alpha(s)}{ds} \right|^2 . \tag{3.5}$$

(ii) The enthalpic energy associated with the unfavorable interactions between the different blocks: We quantify these interactions in terms of two Flory-Huggins interaction parameters, χ_{ABR} representing the interaction between A block and the combined units of B and R blocks, and χ_{BR} representing the interaction between B and R units. In principle, a more general representation will involve three parameters describing the interactions between A and B, B and R, and A and R units. However, we adopt the proposed representation to simplify the parameter space. In terms of these interaction parameters, the enthalpic contributions to the free energy can be expressed as:

$$\begin{aligned} H_1[\mathbf{R}] &= \chi_{ABR}\rho_0 \int d\mathbf{r}\, \hat{\phi}_A(\mathbf{r})(\hat{\phi}_B(\mathbf{r}) + \hat{\phi}_R(\mathbf{r})), \qquad (3.6) \\ H_2[\mathbf{R}] &= \chi_{BR}\rho_0 \int d\mathbf{r}\, \hat{\phi}_B(\mathbf{r})\hat{\phi}_R(\mathbf{r}). \end{aligned}$$

The above expressions are combined with the condition of incompressibility and are reexpressed as:

$$
\begin{aligned}
H_1[\mathbf{R}] &= -\Big(\frac{\chi_{ABR}\rho_0}{4} - \frac{\chi_{BR}\rho_0}{16}\Big) \int d\mathbf{r}\, [\hat{\phi}_A(\mathbf{r}) - (\hat{\phi}_B(\mathbf{r}) + \hat{\phi}_R(\mathbf{r}))]^2, \quad (3.7) \\
H_2[\mathbf{R}] &= -\frac{\chi_{BR}\rho_0}{4} \int d\mathbf{r}\, [\hat{\phi}_B(\mathbf{r}) - \hat{\phi}_R(\mathbf{r})]^2.
\end{aligned}
$$

In the following, we discuss our results with parameter space of the modified interaction parameters, $\chi_1 \equiv \chi_{ABR} - \chi_{BR}/4$ and $\chi_2 \equiv \chi_{BR}$, in terms of which the above equations can be written as :

$$
\begin{aligned}
H_1[\mathbf{R}] &= -\frac{\chi_1\rho_0}{4} \int d\mathbf{r}\, [\hat{\phi}_A(\mathbf{r}) - (\hat{\phi}_B(\mathbf{r}) + \hat{\phi}_R(\mathbf{r}))]^2, \\
H_2[\mathbf{R}] &= -\frac{\chi_2\rho_0}{4} \int d\mathbf{r}\, [\hat{\phi}_B(\mathbf{r}) - \hat{\phi}_R(\mathbf{r})]^2.
\end{aligned} \tag{3.8}
$$

Variations in χ_1 (the only interaction effect studied in this study) are assumed to arise from changes in the interaction between A block and combined units of B and R; (iii) To model the orientational interactions between the rod-like mesogenic units, we utilize a Maier-Saupe type interaction potential. The latter is a mean-field representation where entropic costs arising from non-aligned configurations of rods are ascribed to an energetic cost involving the orientational order parameter $\hat{\mathbf{S}}(\mathbf{r})$ (Eq.(3)). Explicitly,

$$
H_3[\mathbf{R}] = -\frac{\mu\rho_0}{2} \int d\mathbf{r}\, \hat{\mathbf{S}}(\mathbf{r}) : \hat{\mathbf{S}}(\mathbf{r}), \tag{3.9}
$$

where, the Maier-Saupe parameter μ represents the strength of orientational interactions, with high values of μ favoring a stronger alignment of the rods.

The above approach for modeling orientational interactions has been shown to provide semi-quantitatively accurate results for rod-coil block copolymers even possessing reasonably long rods [8]. For SCLC block copolymer systems, which typically involves much shorter rod-like units, this approximation is expected to be even more accurate in describing the orientational interactions.

In sum, the overall partition function for our model can be written as

$$\mathcal{Z} \propto \int \mathcal{D}\mathbf{R}_\alpha(s) d[\mathbf{u}_\alpha(s)] \exp[-\beta(H_0+H_1+H_2+H_3)]\delta[\hat{\phi}_A(\mathbf{r})+\hat{\phi}_B(\mathbf{r})+\hat{\phi}_R(\mathbf{r})-1] \tag{3.10}$$

Using standard field-theoretic techniques, the quadratic interactions in the Hamiltonian can be decoupled by introducing fluctuating chemical potential fields conjugate to the density and orientational order parameters [18]. In a non-dimensional representation, where all lengths are non-dimensionalized using the unperturbed radius of gyration $R_g = b(N/6)^{0.5}$, and the contour variables s and p are non-dimensionalized using the overall molecular weight N, the partition function can be expressed as a functional integral

$$\mathcal{Z} \propto \int_{-\infty}^{\infty} \mathcal{D}[W_1] \int_{-\infty}^{\infty} \mathcal{D}[W_2] \int_{-\infty}^{\infty} \mathcal{D}[\pi] \int_{-\infty}^{\infty} \mathcal{D}[\mathbf{M}] \exp[-\beta H(W_1, W_2, \pi, \mathbf{M})] \tag{3.11}$$

where

$$\begin{aligned} H(W_1, W_2, \pi, \mathbf{M}) = -CV \ln \mathcal{Q} + \frac{C}{\chi_1 N} \int d\mathbf{r}\, W_1^2(\mathbf{r}) + \frac{C}{\chi_2 N} \int d\mathbf{r}\, W_2^2(\mathbf{r}) \\ - iC \int dr\, \pi(\mathbf{r}) + \frac{C}{2\mu N} \int d\mathbf{r}\, \mathbf{M}(\mathbf{r}) : \mathbf{M}(\mathbf{r}). \end{aligned} \tag{3.12}$$

In the above expression, $C \equiv \rho_0 R_g^3/N$ and V is the non-dimensional system volume. $W_1(\mathbf{r})$ represents the potential field conjugate to the difference in volume fractions of the A and B+R blocks ($\hat{\phi}_A(\mathbf{r}) - (\hat{\phi}_B(\mathbf{r}) + \hat{\phi}_R(\mathbf{r}))$), and $W_2(\mathbf{r})$ represents the potential field conjugate to the difference in volume fractions of B and R components ($\hat{\phi}_B(\mathbf{r}) - \hat{\phi}_R(\mathbf{r})$). The incompressibility is enforced by the pressure like chemical potential field $\pi(\mathbf{r})$ [18]. $\mathbf{M}(\mathbf{r})$ is a tensor field conjugate to the orientational order parameter $\hat{\mathbf{S}}(\mathbf{r})$ [8]. In the above expression, $\mathcal{Q}$ represents the single chain partition function of a polymer in the external fields $W_1(\mathbf{r})$, $W_2(\mathbf{r})$, $\pi(\mathbf{r})$ and $\mathbf{M}(\mathbf{r})$, and is given by

$$\begin{aligned}\mathcal{Q}[W_1, W_2, \pi, \mathbf{M}] \propto \int \prod_{\alpha=1}^{\alpha=n} d[\mathbf{u}_\alpha(s)] d\mathbf{R}_\alpha(s) \exp\Bigg[-\frac{1}{4}\int_0^{f_A+f_B} ds \left(\frac{d\mathbf{R}_\alpha}{ds}\right)^2 - \int_0^{f_A} ds\, (-W_1(\mathbf{R}_\alpha(s)) \\ + i\pi(\mathbf{R}_\alpha(s))) - \int_{f_A}^{f_A+f_B} ds\, (W_1(\mathbf{R}_\alpha(s)) - W_2(\mathbf{R}_\alpha(s)) + i\pi(\mathbf{R}_\alpha(s))) \\ - \int dr\, (W_1(\mathbf{r}) - W_2(\mathbf{r}) + i\pi(\mathbf{r}))\hat{\phi_R}(\mathbf{r}) + \int dr\, \mathbf{M}(\mathbf{r}) : \hat{\mathbf{S}}(\mathbf{r}) \,\Bigg]. \end{aligned} \tag{3.13}$$

We denote the potential fields acting on A, B and R segments as $W_A(\mathbf{r})$, $W_B(\mathbf{r})$ and $W_R(\mathbf{r})$ respectively, and are in turn related to the $W_1(\mathbf{r})$, $W_2(\mathbf{r})$ and $\pi(\mathbf{r})$ fields as

$$\begin{aligned} W_A(\mathbf{r}) &= -W_1(\mathbf{r}) + i\pi(\mathbf{r}), \qquad (3.14) \\ W_B(\mathbf{r}) &= W_1(\mathbf{r}) - W_2(\mathbf{r}) + i\pi(\mathbf{r}), \\ W_R(\mathbf{r}) &= W_1(\mathbf{r}) + W_2(\mathbf{r}) + i\pi(\mathbf{r}). \end{aligned}$$

We observe that Eq.(13) can be simplified by noting that the orientational degrees of freedom of each of the rod units on the backbone are independent of each other. This allows us to express Eq.(13) as

$$\begin{aligned}\mathcal{Q} \propto \int d\mathbf{R}_\alpha \mathrm{exp}\left[-\frac{1}{4}\int_0^{f_A+f_B} ds\left(\frac{d\mathbf{R}_\alpha}{ds}\right)^2 - \int_0^{f_A} ds\, W_A(\mathbf{R}_\alpha)\right. \\ - \int_{f_A}^{f_A+f_B} ds\, W_B(\mathbf{R}_\alpha) + N\int_{f_A}^{f_A+f_B} ds\ \ln g(\mathbf{R}_\alpha)\,]\end{aligned} \tag{3.15}$$

where

$$g(\mathbf{r}) = \int d\mathbf{u}\mathrm{exp}\left[-\int_0^{f_R/N_R} dp\left(W_R(\mathbf{r}+\beta p\mathbf{u}) - \mathbf{M}(\mathbf{r}+\beta p\mathbf{u}) : \left(\mathbf{u}\mathbf{u} - \frac{\mathbf{I}}{3}\right)\right)\right], \tag{3.16}$$

In the above representation, $\ln g(\mathbf{r})$ can be construed as a pseudo "effective potential" acting on a monomer of the B block at position $\mathbf{r}$ arising due to the statistical weight of the rod units linked to it. In the above equation, β ($\equiv aN/b(N/6)^{1/2}$) is the non-dimensional parameter characterizing the length of a rod block.

We observe that the expression Eq.(15) for the partition function of a single polymer chain resembles the partition function for a flexible diblock copolymer, with an overall chemical potential acting on the B segments which includes the rod contributions: $W_B^*(\mathbf{r}) = W_B(\mathbf{r}) - N\ln g(\mathbf{r})$. Moreover, since $g(\mathbf{r})$ involves only an integral over $\mathbf{u}$, Eq.(16) can be evaluated using straightforward numerical techniques. Consequently, the above single chain partition function (Eq.(15)) can be evaluated by solving diffusion-like equations for the end-segment distribution functions, [18, 92] which are very similar in structure to that of a flexible diblock copolymer. Explicitly, if $q(\mathbf{r}, s)$ represents the statistical weight for a chain of length 's' to have its end at position $\mathbf{r}$,

$$\frac{\partial}{\partial s} q(\mathbf{r}, s) = \begin{cases} \nabla^2 q(\mathbf{r}, s) - W_A(\mathbf{r}) q(\mathbf{r}, s), & 0 \le s \le f_A \\ \nabla^2 q(\mathbf{r}, s) - W_B^*(\mathbf{r}) q(\mathbf{r}, s), & f_A \le s \le f_A + f_B. \end{cases} \tag{3.17}$$

In terms of $q(\mathbf{r}, s)$, we have,

$$\mathcal{Q} = \frac{1}{V} \int d\mathbf{r}\, q(\mathbf{r}, f_A + f_B). \tag{3.18}$$

While all our developments so far are exact, except insofar as the approximations inherent in the micromechanical representation, we now invoke the mean-field approximation, wherein the partition function ($\mathcal{Z}$) is approximated by evaluating the functional integral at its saddle point [18, 17]. This leads to a set of equations relating the potential fields $W_1(\mathbf{r})$, $W_2(\mathbf{r})$, $\pi(\mathbf{r})$ and $\mathbf{M}(\mathbf{r})$ and the species volume fractions and orientational order parameter $\hat{\phi}_A(\mathbf{r})$, $\hat{\phi}_B(\mathbf{r})$, $\hat{\phi}_R(\mathbf{r})$ and $\hat{\mathbf{S}}(\mathbf{r})$ to be solved in a self-consistent manner. Explicitly, the self-consistent equations are:

$$\begin{aligned} \frac{2}{\chi_1 N} W_1(\mathbf{r}) &= \phi_A(\mathbf{r}) - [\phi_B(\mathbf{r}) + \phi_R(\mathbf{r})] \\ \frac{2}{\chi_2 N} W_2(\mathbf{r}) &= \phi_B(\mathbf{r}) - \phi_R(\mathbf{r}) \\ \phi_A(\mathbf{r}) + \phi_B(\mathbf{r}) + \phi_R(\mathbf{r}) &= 1 \\ \frac{1}{\mu N} \mathbf{M}(\mathbf{r}) &= \mathbf{S}(\mathbf{r}). \end{aligned} \tag{3.19}$$

In the above expression, $\phi_i(\mathbf{r})$ represents the local volume fractions of the different components, while $\mathbf{S}(\mathbf{r})$ is the local orientational order parameter. The local volume fractions of the flexible components can be calculated in a manner similar to the situation of pure flexible diblock copolymers: [1]

$$\begin{aligned}\phi_A(\mathbf{r}) &= \frac{V}{Q}\int_0^{f_A} ds\, q(\mathbf{r},s)q^\dagger(\mathbf{r},f_A+f_B-s), \qquad (3.20)\\ \phi_B(\mathbf{r}) &= \frac{V}{Q}\int_{f_A}^{f_A+f_B} ds\, q(\mathbf{r},s)q^\dagger(\mathbf{r},f_A+f_B-s).\end{aligned}$$

In the above equations, $q^\dagger(\mathbf{r},s)$ is the end-segment distribution function and represents the statistical weight for a chain of length 's' to have its end at position at $\mathbf{r}$. It is defined in the same way as $q(\mathbf{r},s)$, except that s is measured from the end of B-block, and satisfies

$$\frac{\partial}{\partial s}q^\dagger(\mathbf{r},s) = \begin{cases} \nabla^2 q^\dagger(\mathbf{r},s) - W_B^*(\mathbf{r})q^\dagger(\mathbf{r},s), & 0 \le s \le f_B \\ \nabla^2 q^\dagger(\mathbf{r},s) - W_A(\mathbf{r})q^\dagger(\mathbf{r},s), & f_B \le s \le f_A+f_B. \end{cases} \qquad (3.21)$$

The volume fractions and orientational order parameters of the rod units can be obtained as

$$\begin{aligned}\phi_R(\mathbf{r}) = N\int d\mathbf{u}\int_0^{f_R/N_R} dp\,\frac{\phi_B(\mathbf{r}-\beta p\mathbf{u})}{g(\mathbf{r}-\beta p\mathbf{u})}\\ \exp\left[-\int_0^{f_R/N_R} dp'\left(W_R(\mathbf{r}-\beta p\mathbf{u}+\beta p'\mathbf{u}) - \mathbf{M}(\mathbf{r}-\beta p\mathbf{u}+\beta p'\mathbf{u}) : \left(\mathbf{u}\mathbf{u}-\frac{\mathbf{I}}{3}\right)\right)\right],\end{aligned} \qquad (3.22)$$

and

$$\mathbf{S}(\mathbf{r}) = N \int d\mathbf{u} \int_0^{f_R/N_R} dp \, \frac{\phi_B(\mathbf{r} - \beta p \mathbf{u})}{g(\mathbf{r} - \beta p \mathbf{u})} \left(\mathbf{u}\mathbf{u} - \frac{\mathbf{I}}{3} \right)$$
$$\exp\left[- \int_0^{f_R/N_R} dp' \left(W_R(\mathbf{r} - \beta p \mathbf{u} + \beta p' \mathbf{u}) - \mathbf{M}(\mathbf{r} - \beta p \mathbf{u} + \beta p' \mathbf{u}) : \left(\mathbf{u}\mathbf{u} - \frac{\mathbf{I}}{3} \right) \right) \right]. \tag{3.23}$$

The physical interpretation of the above two expressions is that the density (or the orientational density parameter) of the rod segment "p" at position $\mathbf{r}$ and oriented at an angle $\mathbf{u}$, is directly linked to the density of backbone ($\phi_B(\mathbf{r})$) at the position $\mathbf{r} - \beta p \mathbf{u}$. The integrals in the above equations then accounts for all the possible orientation of the rods and all the monomers of the rod, with the exponential terms accounting for the probability that a rod segment whose link with the flexible backbone located at $\mathbf{r} - \beta p \mathbf{u}$ is oriented at an angle $\mathbf{u}$.

In essence, our model formulation transforms the influence of side chain units as a potential onto the B segments, necessitating solution of only two diffusion equations ($q(\mathbf{r}, s)$ and $q^\dagger(\mathbf{r}, s)$) for the polymer. This contrasts with earlier models of comb-like polymer where the combs were assumed to be grafted at arbitrary locations and requires solution of multiple diffusion equations [86].

3.2.1 Details of Numerical Calculations and Parameters

The self-consistent equations (Eq.(19)) are solved by a real space evolution method developed by Fredrickson and coworkers [18]. This method entails starting with random initial conditions for the potential fields, which are then evolved until the self-consistent solutions to Eq.(18) are achieved. The pseudo evolution equations employed in this scheme are of the form:

$$\begin{aligned}
\frac{\partial W_1(\mathbf{r})}{\partial t} &= -\lambda_{W1}\left(\frac{2}{\chi_1 N}W_1(\mathbf{r}) - [\phi_A(\mathbf{r}) - (\phi_B(\mathbf{r}) + \phi_R(\mathbf{r}))]\right), \quad (3.24)\\
\frac{\partial W_2(\mathbf{r})}{\partial t} &= -\lambda_{W2}\left(\frac{2}{\chi_2 N}W_2(\mathbf{r}) - [\phi_B(\mathbf{r}) - \phi_R(\mathbf{r})]\right),\\
\frac{\partial \pi(\mathbf{r})}{\partial t} &= \lambda_\pi[1 - \phi_A(\mathbf{r}) - \phi_B(\mathbf{r}) - \phi_R(\mathbf{r})],\\
\frac{\partial \mathbf{M}(\mathbf{r})}{\partial t} &= -\lambda_M\left(\frac{\mathbf{M}(\mathbf{r})}{\mu N} - \mathbf{S}(\mathbf{r})\right).
\end{aligned}$$

In the above equations, the fictitious mobility coefficients (λ_π) for the incompressibility field $\pi(\mathbf{r})$ was typically chosen as between 0.2-0.3, and the mobility coefficients ($\lambda_{W1}, \lambda_{W2}$ and λ_M) for other fields were chosen to be between 0.1-0.15. We employed a box size of $8R_g \times 8R_g$ for our simulations. The discretization along the length of flexible backbone Δs was chosen to be 0.005. The diffusion equations in two dimensions were solved by an operator splitting strategy [93]. Despite the fact that simulations were carried out assuming two dimensional variations in volume fractions and orientational order parameter, the orientational vector was allowed to be a unit vector in the three dimensional plane. Hence the average orientational order parameter $\mathbf{S}(\mathbf{r})$ and its conjugate potential field $\mathbf{M}(\mathbf{r})$, are symmetric, traceless 3×3 matrices. Integrations over orientational vector $\mathbf{u}(\mathbf{r})$ were evaluated by utilizing a ten-point Gaussian quadrature [93].

The overall self-assembly behavior is governed by a vast parametric space which includes f_A, $\chi_1 N$, $\chi_2 N$, N_R, m, μN and β. The first two parameters also arise in the context of the phase behavior of the flexible diblock copolymers, while the other parameters arise in the specific context of the SCLC block copolymer. In the results discussed in the next section, the ratio $\mu N/\chi_1 N$ was kept fixed at a value of 15. The non-dimensional length of the rod unit was fixed at $\beta = 5$ for the case of higher molecular weight. The interaction parameter between the flexible backbone and the side chain mesogenic units was also kept fixed throughout the simulations as $\chi_2 N = 20$.

To determine the onset and characteristics of microphase separation transition, both the equilibrium component volume fraction profiles and the free energies are used. To identify the orientational ordering transition, we calculate an order parameter: $\bar{S}(\mathbf{r}) = 1.5\lambda_{max}(\mathbf{r})$, where $\lambda_{max}(\mathbf{r})$ denotes the maximum eigenvalue of the tensor $\mathbf{S}(\mathbf{r})$. This order parameter, when normalized by rod volume fraction $\phi_R(\mathbf{r})$ equals unity for the case of complete alignment of the rods, and is zero for random orientation of rods. The orientation of the rod units are along the eigenvector corresponding to the maximum eigenvalue of the orientational order tensor $(\lambda_{max}(\mathbf{r}))$. In the following section, we present results obtained by assuming that the solutions of the self consistent field theory equations exhibit a 2-D symmetry.

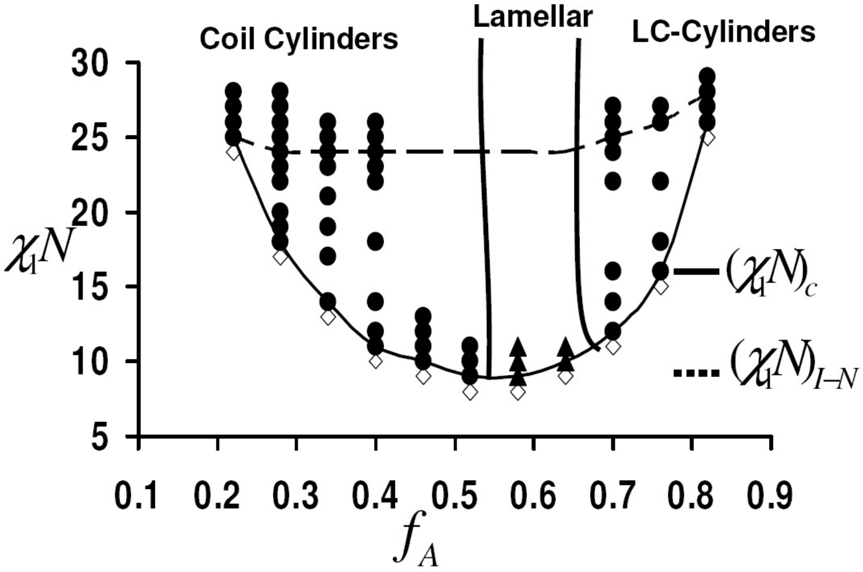

Figure 3.2: Self assembly phase diagram obtained from 2D calculations. The parameters are $N = 200$ and $m = 5$. The solid line represents the transition from disordered phase to microphase separation, and the dashed line represents the transition to smectic ordering. Open diamonds represents disordered phase, while triangles represent lamellar phases and the circles represent the cylindrical morphologies discussed in the text.

3.3 Results and Discussion

3.3.1 Phase Diagram and Morphologies

In the present section, we present results which show the effects of varying the volume fraction of A block (f_A) and the interaction parameter ($\chi_1 N$) on the nature of morphologies formed and the orientational ordering of the mesogenic units. In Figure 3.2, we present the self-assembly phase diagram for the case of $N = 200$ and $m = 5$. The boundaries indicated between the different phases are just meant to be guidelines to the eye and do not represent real phase boundaries obtained as output of our simulations. The solid line represents the transition from isotropic to phase separated morphology (denoted as $(\chi_1 N)_C$), and the dashed line represents the onset of orientational ordering of the mesogenic units (denoted as $(\chi_1 N)_{I-N}$). From Figure 3.2, it can be observed that the critical value of Flory-Huggins interaction parameter $(\chi_1 N)_C$ needed for microphase separation transition is less than or equal to the value of $(\chi_1 N)_{I-N}$ for the onset of smectic ordering, suggesting that the formation of microphases was a necessary condition for the development of orientational ordering. Overall, we also observe that the phase diagram is not symmetric in the volume fractions of the A and B blocks.

At low volume fractions of the A block ($0.22 \leq f_A \leq 0.52$), hexagonally packed cylinders of A phase surrounded by continuous matrix of LC (B+R) block are formed. Figure 3.3(a) displays a representative 2D volume fraction profile (in the x-y plane) for such a morphology. In Figure 3.3(b), the z-component ($\mathbf{S}_z(\mathbf{r})$) of the eigenvector corresponding to the orientation is displayed. From Figure 3.3(b), it is evident that in the region outside the cylinder (B+R phase), the value of $\mathbf{S}_z(\mathbf{r})$ is unity, which implies that the rods prefer to orient themselves along the axis of coil cylindrical domains. The schematic shown in Figure 3.3(c) depicts the conformations of the chains and the orientational arrangement of side chain units outside the cylindrical domains. This orientation can be rationalized by observing that the alternative, involving the tangential orientation of the mesogens would lead to defects and would be unfavorable relative to the observed axial orientation of the rods. This morphology and the orientation of the rods (Figure 3.3(c)) have been reported by many researchers [31, 30, 9, 83, 84].

In the intermediate region of the phase diagram ($0.52 \leq f_A \leq 0.64$), lamellar phases of amorphous and LC blocks are observed in conjunction with an orientational ordering within the lamellar domains. Figure 3.4(a) displays the 2-D density profile for lamellar structure observed at a volume fraction of $f_A = 0.64$ and $\chi_1 N = 10$. In Figure 3.4(b), the z-component ($\mathbf{S}_z(\mathbf{r})$) of the eigenvector corresponding to the orientation is displayed. In the region of LC phase (B+R), the value of $\mathbf{S}_z(\mathbf{r})$ is unity, suggesting that the rod units are aligned parallel to the block copolymer interface and out of the plane of the paper. Figure 3.4(c) shows a schematic of the chain conformations and the orientation of rods within the lamellar microphases. This orientation can be rationalized as arising from the tendency of the flexible backbone (B segments) to stretch outwards from the interface, thus aligning the side-chain mesogenic

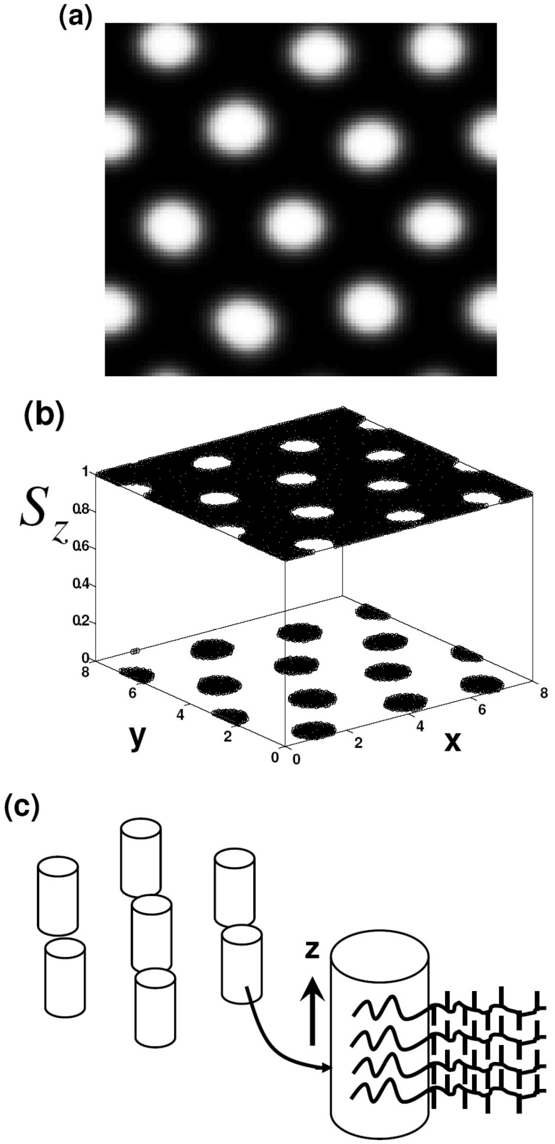

Figure 3.3: (a) Hexagonally packed coil cylinders in a continuous LC block phase. $N = 200$, $m = 5$, $f_A = 0.22$ and $\chi_1 N = 25$. (b) The z-component ($\mathbf{S}_z(\mathbf{r})$) of the eigenvector corresponding to $\lambda_{max}(\mathbf{r})$. In regions where LC phase appears, the value of $\mathbf{S}_z(\mathbf{r})$ is 1.0, which implies that the orientation is along the z-axis. (c) A schematic representation for this morphology along with the nature of orientation of side chain liquid crystalline units within these microphases.

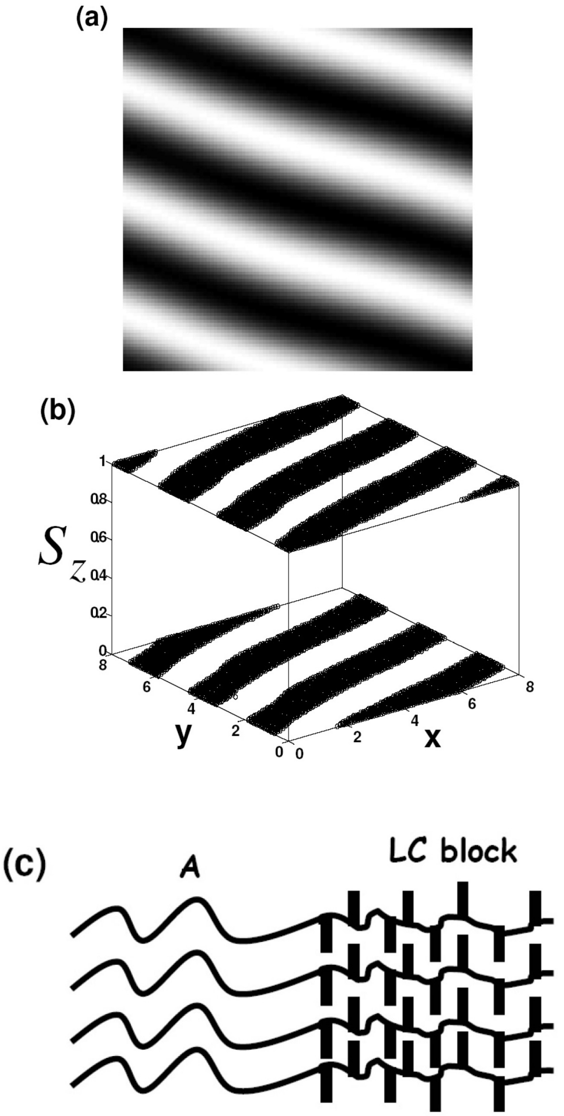

Figure 3.4: (a) Lamellar morphology for amorphous and LC blocks. The parameters are $N = 200$, $m = 5$, $f_A = 0.64$ and $\chi N = 10$. The rods are oriented parallel to interface between the two blocks. (b) A plot of the z-component ($\mathbf{S}_z(\mathbf{r})$) of the eigenvector corresponding to $\lambda_{max}(\mathbf{r})$. In regions, where the LC phase appears, the orientation is along the z-axis. (c) A schematic representing microphase separation and orientational ordering.

units in the direction parallel to the block copolymer interface. The results of Figure 3.4 are also consistent with experimental observations which have reported such morphologies and orientations for SCLC block copolymers with a short alkyl spacers [3].

In the case of a simple flexible diblock copolymer, lamellar phases are typically observed in the center of the phase diagram ($0.35 \lesssim f_A \lesssim 0.65$). In contrast, we observe for the case of side-chain liquid crystalline block copolymers, that lamellar phases are formed at values of f_A slightly greater than 0.5. This asymmetry in the phase diagram can be ascribed to the fact that the attachment of the rod units renders the LC block much more bulkier than the amorphous coil block. Consequently even a volume fraction of $f_A = 0.5$ involves an asymmetric diblock copolymer with $N_A > N_R$ (i.e. N_B), thereby favoring curved phases. Since the effective volume fractions of A and the B+R blocks are the same, in this scenario, the shorter block (i.e. the B unit) tends to favor being on the outside of the cylinders. Hence, cylindrical domains of amorphous coil blocks are observed in the regime of the phase diagram where the volume fraction f_A is close to and even greater than 0.5.

At values of the volume fraction of the A block corresponding to the majority phase ($0.7 \leq f_A \leq 0.82$), we observe hexagonal phases where the LC block is confined in a cylindrical morphology within a continuous matrix of flexible A block. In Figure 3.5(a), we present representative volume fraction profiles for such hexagonally packed LC cylinders for $\chi_1 N = 18$ and $f_A = 0.76$. In Figure 3.5(b) we present a 3D plot of $\mathbf{S}_z(\mathbf{r})$, which is the z-component of the normalized eigenvector corresponding to $\lambda_{max}(\mathbf{r})$. If the variations in the density profile are assumed to be in the x-y plane, then the orientation of the rod units are observed to be along the z-axis, i.e. the axis of the cylindrical domains. A schematic of this hypothesized conformations of the chains and the orientational characteristics of the rods are depicted in Figure 3.5(c). In this arrangement, the flexible backbone (B) is stretched away from the curved block copolymer interface to minimize contacts between A units and B+R units. Within the cylindrical domains, the rod units have the option of either orienting tangential to the interface or in the axial direction. However, a tangential orientation inside the cylindrical domains is expected to lead to significant energy costs due to defects, and is unfavorable relative to the observed axial orientation of the rods. Experimental observations of such LC cylinder morphologies are reported by Ober and coworkers for a volume fraction of the coil block at $f_A = 0.78$ [31]. They have also speculated that the smectic ordering within the cylindrical domains will be similar to the manner depicted in the schematic shown in Figure 3.5(c). It is pertinent to note that by assuming 2D variations in composition profiles we preclude observation of profiles which involve phase separation between the rods (R) and the backbone coils (B).

In sum, the above morphologies are observed to be a combination of morphologies observed for flexible diblock copolymers along with orientational ordering of the rod units. On the other hand, these morphologies differ significantly from that observed in rod-coil copolymers, wherein, due to more severe steric constraints, mainly lamellar-like morphologies are observed. Moreover, in all our results we observed that microphase separation (ODT) was necessary for development of orientational ordering (I-N), which is also consistent with experimental results wherein it has been observed that well defined lamellae microphase was required to stabilize the formation of smectic C phase [3]. In contrast, in rod-coil copolymers a precursor nematic phase was typically observed prior to microphase separation [7]. The absence of such a precursor disordered nematic phase for SCLC block copolymers can be rationalized as due to the shorter length and lower volume fraction of rod units. Consistent with this hypothesis, the value of averaged orientational order parameter ($< \bar{S}(\mathbf{r}) >$) at the I-N transition was typically found to be in the range 0.2-0.5, much lower than the values observed for rod-coil block copolymers [8].

3.3.2 Effect of molecular weight

We briefly discuss the effect of molecular weight N on the above morphologies by comparing the transition lines for the cases of $N = 100$ and $N = 200$ for a fixed value of rod length ($m = 5$) in Figures 3.6a and b. Overall, for both the molecular weights we observe that the system exhibits similar kinds of morphologies in similar ranges of volume fractions. For the case of smaller N, the transition for smectic ordering ($(\chi_1 N)_{I-N}$) is seen to move downward and even coincide with the microphase separation transition $(\chi_1 N)_C$ at very low volume fractions of coil. We note that this behavior is consistent with the experiments of Zheng and coworkers who had observed that for lower molecular weights and higher LC block volume fractions, the ODT coincided

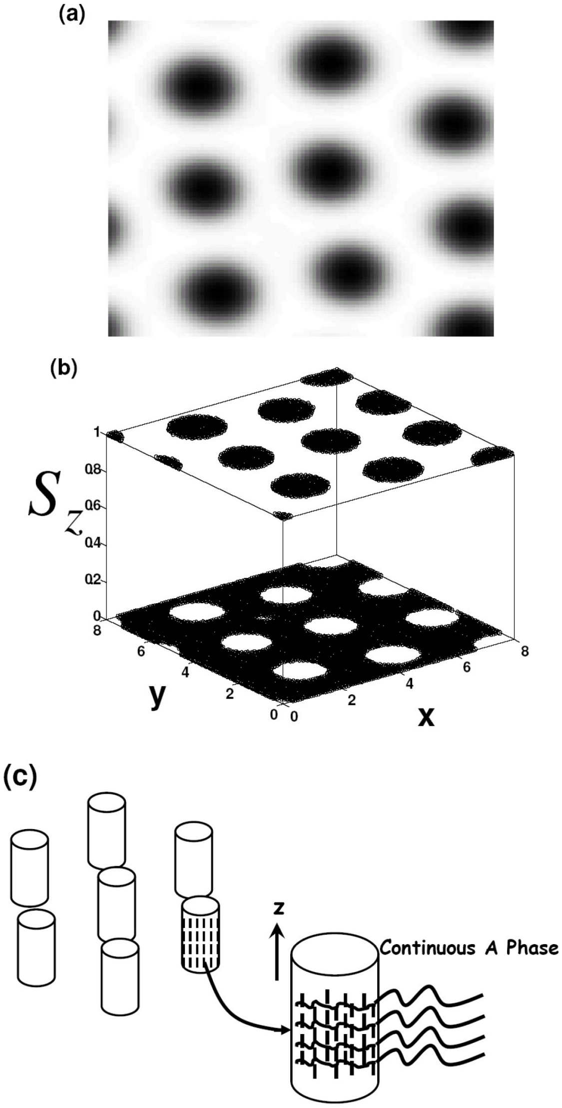

Figure 3.5: (a) Hexagonally packed LC cylinders in a matrix of A block. The parameters are $N = 200$, $m = 5$, $f_A = 0.76$ and $\chi_1 N = 18$. (b) A plot of the z-component ($\mathbf{S}_z(\mathbf{r})$) of the eigenvector corresponding to $\lambda_{max}(\mathbf{r})$. In regions, where the LC phase appears, the orientation is along the z-axis. (c) A schematic representation of the observed morphology.

with the I-N transition temperature [29]. To rationalize this decrease in the critical $(\chi_1 N)_{I-N}$ for orientational ordering, we note that whereas the onset of microphase separation is governed by value of $\chi_1 N$, the onset of orientational ordering can be understood to be governed by the Maier-Saupe parameter μ (for a fixed length of the rod m – cf. discussion following eq. (3.27)). The ease of undergoing orientational ordering relative to microphase separation is thus governed by the factor $\mu/\chi_1 N$. For the present case, since the ratio μ/χ_1 is kept fixed, the orientational ordering relative to the microphase separation is governed by the factor $1/N$. Hence, on decreasing N, the orientational ordering is seen to be favored. We also observe that for $N = 100$, at lower volume fractions of the coil block ($0.22 \leq f_A \leq 0.28$), the earlier onset of orientational ordering also drives the ODT to lower values of $\chi_1 N$.

As more explicitly demonstrated in our SST model, for the parameterization adopted in this study the effective repulsion between the coil and LC blocks depend on the orientational order parameter (cf. Section 3.4.2). Consequently, a nonzero value of the orientational order parameter renders the effective repulsion stronger and hence lowers $(\chi_1 N)_C$.

3.3.3 Summary of Results From Other Parametric Studies

We also determined the effects of using different values for the rod lengths ($m = 3, 9$ and 11) and Maier-Saupe parameters ($\mu/\chi = 10$) upon the phase diagram (in each individual case the remaining parameters were fixed at values

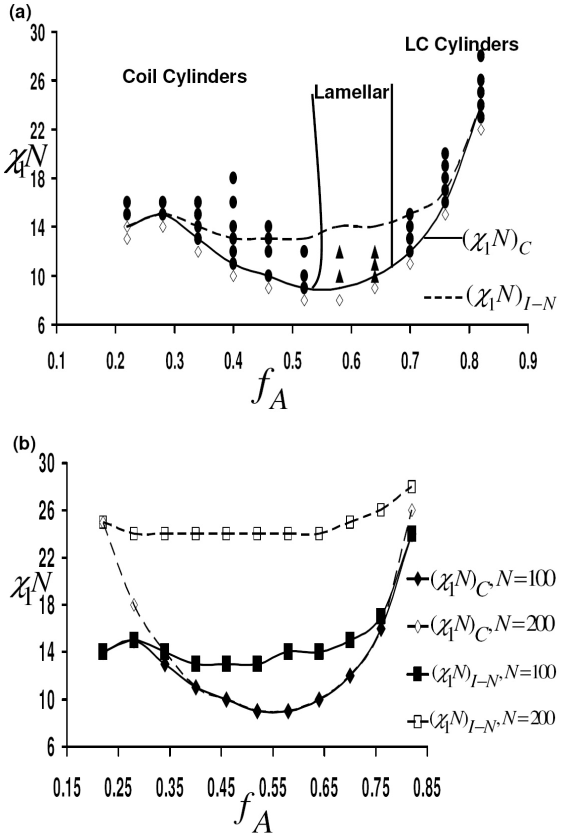

Figure 3.6: (a) Self assembly phase diagram obtained from 2D calculations for the parameters are $N = 100$ and $m = 5$. Microphase separation and isotropic-smectic transition occurred at the same value of $\chi_1 N$ for this parametric case. (b) Comparison of microphase separation transition and isotropic-nematic transition (I-N) of the rods units for two cases: $N = 200$ and $m = 5$, and $N = 100$ and $m = 5$.

corresponding to Fig. 3.2). In all cases, the results obtained could be understood in an intuitive manner (and more explicitly through the SST model presented next section), and hence we restrict ourselves to a brief discussion of our findings. For all the cases examined, microphase separation transition was found to be a necessary condition for the occurrence of I-N transitions. Overall, the self-assembly morphologies and the order-order transitions were only slightly influenced by parameters such as m and μ. Moreover, except for small values of f_A, the microphase separation transition temperature ($(\chi_1 N)_C$) was only weakly affected by the values of the rod length m and the Maier-Saupe parameter μ. In contrast, the orientational ordering transition ($(\chi_1 N)_{I-N}$) was observed to monotonically decrease upon increasing either the length of the rod block and/or Maier-Saupe parameter. The stronger tendency for orientational ordering can be rationalized as arising from the stronger excluded volume interactions and the more pronounced tendency to orient in longer rods and/or for stronger interactions. In contrast, since in majority of the phase diagram microphase separation transition occurred when the rod units were still in the isotropic phase, and such a transition was much less influenced by the rod length.

3.4 Strong Segregation Theory For Ordering in SCLC

We note that strong segregation theories (SST) have played an important role in the theoretical descriptions of morphologies observed in multicomponent polymeric materials [1, 90, 94, 95]. The results presented in the preceding section suggested that morphologies observed in SCLC parallels those observed in flexible diblock copolymers, except with the additional possibility of orientational ordering within the mesophases. These results motivated us to examine whether a SST approach can be developed for predicting the morphologies observed in SCLC.

3.4.1 Model and Governing Equations

To enable a SST development, we distill the model and physics of self-assembly in SCLC polymers into a few key features and assumptions: (i) The rod units are assumed to contribute to an increased monomeric volume of the B segments. In turn, the latter affects the interfacial tension of AB interphases; (ii) The effective interaction between A and B blocks depends upon the orientational order parameter in the corresponding phase; (iii) The orientational ordering of the rod mesophases can be discerned by adopting the classical Maier-Saupe theory adopted to account for the volume fraction of rods in the mesophase; (iv) As always, SST is expected to be valid only for the situation of strongly segregated phases wherein the interfacial thickness is small [89]. In

Section 3.4.3 we discuss some limitations of these model assumptions.

Our approach involves an estimation of the free energies of: (a) Disordered-Isotropic, (b) Disordered-Nematic, (c) Ordered-Isotropic, and (d) Ordered-Nematic phases to determine the preferred phase. In SST, all free energies are evaluated either for a compositionally homogeneous state or a completely segregated state. In either case, estimation of the effective volume fractions and the enthalpic interactions prove straightforward. For ordered phases, the additional free energy contributions arising from the interfacial tension and stretching free energies have been evaluated for flexible diblock copolymers and can be adapted to our context.

Isotropic-Nematic Transitions Among the different possible phases, the transitions between the isotropic and nematic phases (in both the disordered and ordered regimes) are governed only by the Maier-Saupe parameter μ and the effective rod volume fractions in that phase. Explicitly, in the Maier-Saupe approximation the orientational free energy can be expressed on a *per rod basis* as: [96]

$$\beta F_{\text{orient}} = \int d\theta f(\theta) \ln[f(\theta)] \sin\theta - \frac{m\mu\phi_R}{2} S^2, \tag{3.25}$$

where $f(\theta)$ denotes the angular distribution of the rod orientations and normalized such that

$$\int d\theta f(\theta) \sin\theta = 1 \tag{3.26}$$

and

$$S = \int d\theta f(\theta) P_2(\cos\theta) \sin\theta, \tag{3.27}$$

where $P_2(x)$ denotes the Legendre polynomial of second order. Minimizing over $f(\theta)$ yields a first order phase transition between an isotropic and nematic phase at

$$(m\mu\phi_R)_C = 4.541. \tag{3.28}$$

The effective volume fractions of the rods can be estimated in the disordered and ordered phases as $\phi_R^D = m(1-f_A)/(m+1)$ and $\phi_R^O = m/(m+1)$ respectively. Whence, for a given χ (recall that our parameterization fixes the ratio μ/χ), the relative preference (within either a disordered or ordered phase) for an isotropic vs. nematic phase and the respective orientational order parameters can be evaluated *apiori* by checking if $m\mu(\phi_R^D, \phi_R^O) > 4.541$ and subsequently minimizing the above functional eq. (3.25) to determine the order parameter within that phase. Subsequently, to discern the order-disorder transition (ODT) it just suffices to compare the free energies of an ordered and a disordered phase with *predetermined* orientational ordered parameters S_O and S_D respectively.

Order-Disorder Transitions To determine the order disorder transitions we adopt many of the earlier developments in the context of flexible diblock copolymers, while making allowance for the possible difference in free energies due to the differences in order parameters S_O and S_D. We use a model of a flexible A-BR block copolymer containing N segments with the segmental volume of the A units ρ_0^{-1} and the segmental volume of the BR units $(m{+}1)\rho_0^{-1}$. The volumes of A block (V_A), BR block (V_{BR}) and the entire copolymer chain

V_C are:

$$V_A = \frac{N_A}{\rho_0}; V_{BR} = \frac{N_R(m+1)}{\rho_0}; V_C = V_A + V_{BR} \tag{3.29}$$

The unperturbed radius of gyration of the A, B and the total chain are:

$$(R_g^2)_A = \frac{N_A b^2}{6}; (R_g^2)_B = \frac{N_R b^2}{6}; (R_g^2)_C = \frac{(N_A + N_R)b^2}{6} = \frac{b^2 N}{6} \frac{1 + m f_A}{1 + m}. \tag{3.30}$$

Hence, the copolymer chain may be viewed as a flexible Gaussian chain of $N(1 + mf_A)/(1 + m)$ effective monomers.

The difference in free energies between the ordered and disordered phases are expressed as:

$$\frac{(F^{\text{ord}} - F^{\text{dis}})}{k_B T} = \Delta F_{\text{bulk}} + F_{\text{int}} + F_{\text{elastic}}. \tag{3.31}$$

In the above, ΔF_{bulk} denotes the bulk free energy difference between the ordered and disordered phases, F_{int} and F_{elastic} represents the interfacial and elastic free energy costs in the ordered phases. ΔF_{bulk} can be estimated as (on a per chain basis):

$$\Delta F_{\text{bulk}} = -f_A(1-f_A)\chi_1 N + \frac{\mu m^2 N}{2(m+1)^2}(1-f_A)[(1-f_A)S_D^2 - S_O^2] + \frac{N(1-f_A)}{m+1}[\sigma(S_D) - \sigma(S_O)]. \tag{3.32}$$

In the above, the first term arises from the enthalpic contributions due to repulsions between A and (B+R) segments. The second term represents the difference in the Maier-Saupe interactions due to a possible difference in the orientational order parameter between the disordered and ordered phases. The third term represents the orientational entropy of the rods in the different phases, with

$$\sigma = \int d\theta f(\theta) \ln[f(\theta)] \sin\theta. \tag{3.33}$$

[The last two terms in eq. (3.32) are identical to those in eq. (3.25)]. It is evident from the first two terms of eq. (3.32) that the effective repulsions between the A and BR blocks are dependent upon the value of the orientational order parameter S. This feature can be seen more clearly by noting that the enthalpic contributions to the bulk free energy in our model is of the form:

$$\rho_0^{-1} F_{\text{bulk}}^{\text{enth}} = -\frac{\chi_1}{4}[\phi_A - (\phi_B + \phi_R)^2] - \frac{\mu}{2}\phi_R^2 S^2. \tag{3.34}$$

In the approximation used in the SST model, $\phi_R = m\phi_B = m(1-\phi_A)/(m+1)$. This allows us to rewrite eq. (3.34) as:

$$\rho_0^{-1} F_{\text{bulk}}^{\text{enth}} = -\big(\frac{\chi_1}{4} + \frac{\mu m^2}{8(m+1)^2}S^2\big)[\phi_A - (\phi_B + \phi_R)^2] + \text{ other terms}, \tag{3.35}$$

rendering more clearly that the repulsions between A and BR blocks are governed by an effective interaction parameter χ_{eff}

$$\chi_{\text{eff}} = \frac{\chi_1}{4} + \frac{\mu m^2}{8(m+1)^2}S^2. \tag{3.36}$$

To estimate F_{int} we rely on our model of a conformationally asymmetric diblock copolymer for which Helfand and Sapse have computed the interfacial tension [95]. Explicitly, the interfacial tension γ_{ABR} for a conformationally asymmetric diblock copolymer with monomeric densities ρ_0 and $(m+1)^{-1}\rho_0$ with an effective interaction parameter χ_{eff} is given as:

$$\frac{\beta\gamma_{ABR}}{\rho_0 b} = \sqrt{\frac{\chi_{\text{eff}}}{6}}\frac{2[(m+1)^{3/2}-1]}{3m(m+1)}. \tag{3.37}$$

Strictly speaking, the above expression is only approximate for our situation where the inhomogeneous variations in the orientational order parameter S is also expected to influence the interfacial tension between the phases. The latter is an effect not accounted within our SST model.

To estimate the elastic energy contribution F_{elastic} (and the area per chain required to compute F_{int} from eq. 3.37) requires us to consider different possibilities for ordered phases. In line with our SCFT calculations, we restrict our consideration to the cases of lamellar structures, A-cylinders and BR cylinders. For each of these situations, we adapt the calculations of F_{elastic} presented by Semenov [90].

(i) Lamellar Phases: For a lamellar phase of period $2h$, the thicknesses of A and BR brushes can be estimated as $h_A = f_A h$ and $h_{BR} = (1-f_A)h$. The stretching free energy per chain in this configuration is:

$$F_{\text{elastic}} = \frac{h^2}{4(R_g^C)^2}\left(\frac{f_A\,(mf_A+1)}{(m+1)} + (1-f_A)\,(mf_A+1)\right) \tag{3.38}$$

The interfacial area per chain is, $(N_A + N_R(m+1))/\rho_0 h$, which yields,

$$F_{\text{int}} = \frac{2\left(1-\sqrt{1+m}+m\,(2+m)\right)\sqrt{\chi_{\text{eff}}N}}{3m\sqrt{1+m}\sqrt{1+m\,f_A}}\,\frac{R_g^C}{h} \tag{3.39}$$

(ii) Cylindrical phases: The free energy (per chain) of a *convex* molten cylindrical brush made of a polymer with N_x monomers and with inner radius R_i and outer radius R_o is: [90]

$$F_{\text{out}}^{\text{cyl}} = \frac{3(R_o^2 - R_i^2)\log(R_o/R_i)}{4b^2 N_x}. \tag{3.40}$$

The free energy (per chain) of a *concave* molten cylindrical brush made of a polymer with N_x monomers and a radius R_i is:

$$F_{\text{in}}^{\text{cyl}} = \frac{\pi^2}{16b^2}\frac{R_i^2}{N_x}. \tag{3.41}$$

(a) A cylinders: For cylindrical structures with A chains forming the internal phase of the cylinder with a radius R_i, the thickness of the external (BR phase) cylinder (i.e. $R_o - R_i$ above) can be estimated as $R_i/\sqrt{f_A}$. The interfacial area per chain is: $2f_A N/\rho_0 R_i$.

(b) BR cylinders: For cylindrical structures with BR chains forming the internal phase of the cylinder with a radius R_i, the thickness of the external (A phase) cylinder (i.e. $R_o - R_i$ above) can be estimated as $R_i/\sqrt{1-f_A}$. The interfacial area per chain is: $2(1-f_A)N/\rho_0 R_i$.

The sum total of elastic and interfacial free energy costs in different phases (as function of h and R_i respectively) can be minimized with respect to the h and/or R_i to yield the preferred period and hence the elastic and interfacial free energy costs of forming the ordered structure (to maintain brevity we do not display the explicit expressions for the periods and radii in the text).

A comparison of the relative free energies of the ordered phases then allows one to discern the preferred ordered phase if the system were to order. The free energy cost of the preferred ordered phase when combined with ΔF_{bulk} allows us to compare the relative preference for ordering and hence the order-disorder transition temperatures. In the next subsection, we mainly discuss the physical insights derived from such a model and a brief comparison to the SCFT results.

3.4.2 Physical Insights From SST

Within the assumptions of our model, the main outcome of our SST calculations is the identification of the primary driving forces behind the orientational and compositional ordering. As seen from eq. (3.28), the orientational ordering is dependent only on the parameters μ, m and ϕ_R. The only effect of compositional ordering transitions upon the I-N transition is suggested to be a renormalization of the effective volume fraction of the rods ϕ_R which differs between the ordered (but is independent of the nature of the ordered phase) and disordered phases. Moreover, in the ordered phase ϕ_R is independent of the volume fraction of the A phase f_A. These features rationalize the fact that in the phase diagrams presented in Figs. 3.2 and 3.6, where the I-N transitions occur within the ordered phases, the lines corresponding to I-N transitions (I-N) appear practically independent of f_A.

The above arguments also allow us to comment on the onset of I-N transitions relative to the order-disorder transition. Indeed, our SST model suggests that while it is certainly easier for orientational ordering to occur in the compositionally ordered phases (due to a larger effective ϕ_R), nevertheless orientational ordering in the compositionally disordered phases is also possible for appropriate parameters of μ, m and ϕ_R^D. Moreover, since $\phi_R^D \propto 1 - f_A$, such a transition is more likely for smaller values of f_A. This conclusion is broadly consistent with the results presented in section 3.3.2 and the experimental observations of Zheng and coworkers who had observed that for lower molecular weights and higher LC block volume fractions, the ODT coincided with the I-N transition temperature [29].

The SST model predicts the orientational ordering to depend only on the Maier-Saupe interaction parameter μ and to be independent of the χ parameter (our SCFT model fixes the ratio μ/χ thereby endowing a fictitious dependence on χ). On the other hand, from eq. (3.32) it is seen that the ODT can indeed be influenced by the orientational ordering if the rods are either orientationally ordered in the disordered phase itself or if the transition to the compositionally ordered phase is also accompanied by a I-N transition. In either of these instances, the orientational order parameters S_D and S_O will be such that $S_O > S_D$. From eqs. (3.32) and (3.36) it can be seen that this results in a free energy preference for compositionally segregated phases, and in turn can be viewed as an increase in the effective χ parameter between the A and B blocks. Finally, for the situation when the ODT occurs between two isotropic phases, our SST model suggests that the self-assembly characteristics (including order-order transitions) expected to semi-quantitatively resemble the phase behavior of conformationally asymmetric diblock copolymers. The phase diagrams presented in Figs. 3.2 and 3.6 certainly accord with this expectation.

3.4.3 Comparisons of SST Results to SCFT

While the SST is much simpler to implement than SCFT calculations and provides physical insights, the model assumptions restrict its applicability to only a special class of situations. Even discounting the typical limitations of SST (i.e. its validity only for extremely strong segregations) [89], a significant assumption of our model is in our characterization that the main effect of the rod units is in its contribution to an increased monomeric volume of the B segments. This assumption is expected to be valid only under the combined situation of short rods and near perfect orientational ordering in the compositionally ordered mesophases — a combination which is extremely hard to achieve in reality. Indeed, when rods transverse more than (approximately) the segment length b of the flexible components in the XY plane (the plane of compositional ordering) they can no longer be regarded as just contributing volume to "a segment" of the backbone. Moreover, the interplay of rod orientations and the compositional inhomogeneity near the interfaces is also certain to render the expression (3.37) suspect for our system. Whereas, the SCFT model suffers from no such limitations and can in principle handle arbitrarily long rods and segregations.

Considering the above aspects, it is to be expected that the comparison between SCFT and SST would at best be qualitative with the correspondences becoming better for shorter rod conditions. Since in our SST model, the rod length scales with the m parameter this would be expected for smaller m values. In Fig. 3.7a, b and c we display results which illustrate this expectation. Figure 3.7a presents the SST results corresponding to the SCFT results presented Fig. 3.6 where $m = 5$ and $N = 100$. In contrast, Figs. 3.7b and 3.7c present the SCFT and SST results corresponding to $N = 100$ and $m = 3$. It can be seen that while in both cases SST predicts the qualitative trends very well (including the ODT values, a regime where SST is actually expected to be inaccurate), a quantitative correspondence is achieved between the morphologies displayed in Figs. 3.7b and c which correspond to the case of shorter rods. However, the I-N lines are observed to be shifted upward in the SCFT results compared to the SST results. This observation can be rationalized by noting that the I-N lines in SST assumed a perfect segregation of the components right at the ODT. In reality, this condition is not met until much higher $\chi_1 N$.

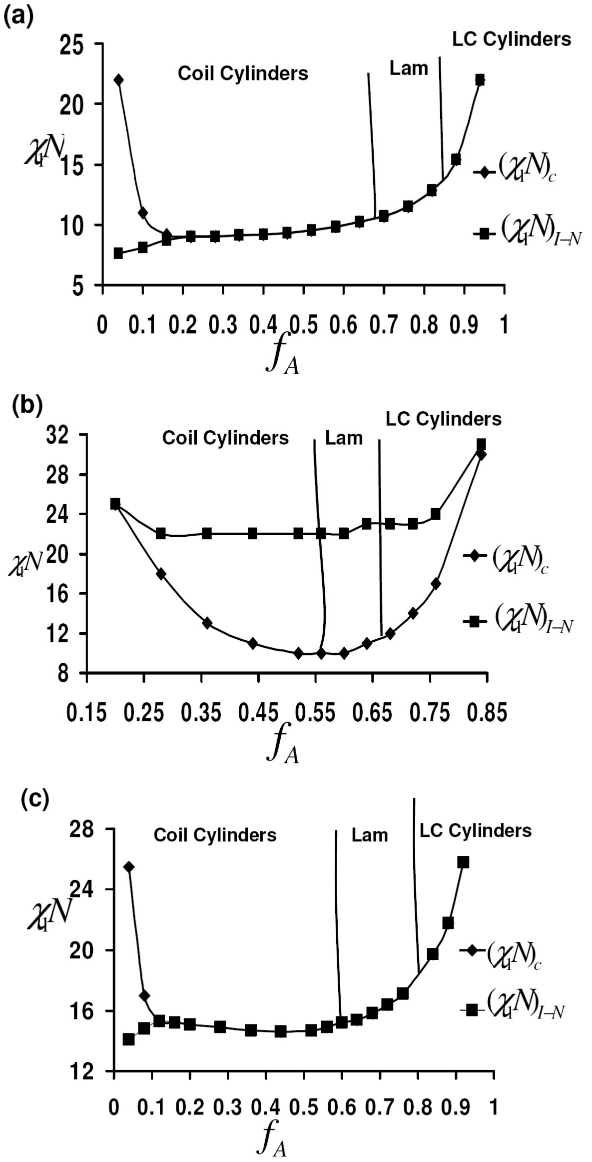

Figure 3.7: (a) SST phase diagram for the parameters $N = 100$ and $m = 5$. (b) SCFT phase diagram for the case $N = 100$, $m = 3$ and $\beta = 1$. (c) SST phase diagram for the case $N = 100$ and $m = 3$. In (a) and (c) the I-N transition lines coincide with the ODT's for a major portion of the phase diagram.

3.5 Conclusions

In this chapter, we have proposed a self-consistent field theoretic model and a SST based analytical theory to understand the thermodynamic behavior of side chain liquid crystalline diblock copolymers. In the SCFT model, the effect of side chain mesogenic units were accounted by incorporating rod-like units attached to every monomer of the flexible backbone. This model allowed us to combine the orientational ordering interactions of the rod segments with the mean field theory of flexible diblock copolymer. We solved the model to study the various 2D morphologies and the orientational characteristics of the rod segments as a function of molecular weight, rod length, interaction parameters and volume fraction of each block. The morphologies observed were similar to the ones found for the case of flexible diblock copolymer, with additional possibility for smectic orientational ordering. An important result of our simulation was that for the parameter space probed, the microphase separation was a necessary condition for the development of orientational ordering. Cylindrical morphologies with the LC block in the dispersed or the continuous phases were observed. The orientational ordering was always observed to be parallel to the block copolymer interface, and in the case of cylinders, parallel to the axis of cylinders. The orientational ordering transition was observed to be favored by reducing the molecular weight of the polymer and/or by increasing the rod length. Another interesting result was the effect of orientational interactions in influencing the ODT of the block copolymer in the regime of higher volume fractions of the LC block. While we presented limited representative parametric results, the advantage of the SCFT model is that it makes the exploration of the vast parametric space involved in the system easily amenable. Moreover, extensions to SCLC with a longer alkyl spacer (modeled as another polymer) [29], multiblock SCLC, solutions of SCLC etc. can be accomplished in a straightforward manner.

The SST model was based on a simpler representation of the SCLC block copolymer as a conformationally asymmetric block copolymer. The rod units were assumed to mainly influence the effective volumes of the individual monomers except in the situation wherein the orientational ordering occurred on or before the ODT. We adapted the classical SST ideas for flexible diblock copolymers to discern the qualitative features of the phase diagram. The main utility of the SST model was in its ability to provide physical insights and thereby rationalize the observations accompanying our SCFT model. We also clarified the parametric conditions under which the SST model is expected to accord with the SCFT results and provided evidence supporting our claims. This semi-quantitative comparisons obtained between SCFT and SST model does suggest that the ordering in a wider class of SCLC block copolymers may fruitfully be understood by combining many of the earlier developments in the context of flexible block copolymers with that of orientational ordering in liquid crystals.

Chapter 4

Mechanical Properties of Semicrystalline Multiblock Copolymers

4.1 Introduction

Recent developments in catalysts have led to the synthesis of multiblock copolymers containing semicrystalline polyolefins as potential thermoplastic elastomeric materials [51]. Conventional thermoplastic elastomeric block copolymers, such as poly-(styrene-b-butadiene-b-styrene) (SBS), poly(styrene-b-isoprene-b-styrene) (SIS) etc. typically use microphase separated morphologies in which the glassy hard blocks which act as crosslinks for the soft rubbery blocks. This arrangement leads to the high levels of elasticity and toughness desired of thermoplastics for applications [48, 49, 50]. The more recent developments aim to mimic such characteristics in multiblock copolymers by either linking crystalline polyolefinic end blocks to soft polyolefinic middle blocks [51, 36] or by linking brittle glassy hydrogenated polystyrene blocks to softer crystalline polyethylene blocks [48, 11, 52]. These newer class of materials have been reported to have low Young's moduli, large strains at break, and excellent elastic recovery properties rivalling even commercial thermoplastic elastomers [51]. Not surprisingly, understanding the link between the block architecture, block physical properties, and the resulting mechanical properties of such materials is currently an area of active research.

Many experimental studies have clearly shown that there is a strong correlation between the chain conformations of multiblock copolymers and their mechanical properties and modes of material failure. Explicitly, chains in multiblock copolymers can either be in free (F), bridged (B) or loop (L) conformations (indicated in Fig. 4.1 for diblock, triblock and pentablock copolymers). Of these conformations, *bridges* have been directly implicated in the context of mechanical properties. Physically, it may be understood that the domains of block copolymers that do not contain bridges provide easy planes for failure and hence lower mechanical strengths [53]. For instance, experiments studying PCHE(C)-PE(E) multiblock copolymers have shown that the failure mode changes from a brittle to ductile upon changing the architecture from a triblock copolymer (which contains "bridged" planes only in the E domains) to pentablock copolymers (which contains "bridged" planes in both E and C domains) [48, 52]. Moreover, addition of even 10% pentablock copolymers to the triblock copolymers have been shown to lead to significant increases in the value of strain at failure for the composite, apparently due to the reduction in the number of such failure planes [53]. More directly, a recent study by Phatak and coworkers focussed on the bridging conformations in the crystalline E domains of triblock, tetrablock, and pentablock copolymers and found that irrespective of the chain architecture a universal correlation can be established between the tensile strength of the material and the fraction of bridging in semicrystalline E domains [11].

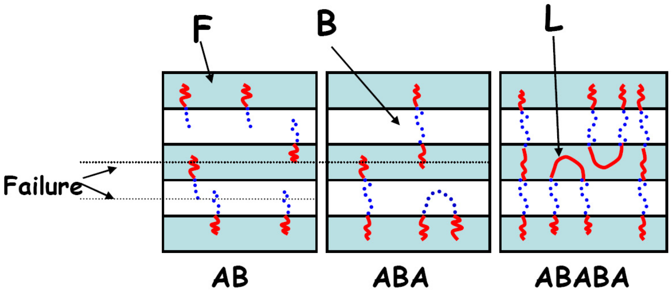

Figure 4.1: Schematic of bridging (B), looping (L), and free (F) conformations in AB diblock, ABA triblock, and ABABA pentablock copolymers. A bridging (B) conformation occurs when the ends of a middle block in a multiblock copolymer lie on different interfaces, whereas in a looped (L) configuration, both the ends lie on the same interface. In a free (F) conformation, only end of a chain is tethered to an interface, while other end is free. Solid line represents A chain, while the dotted line represents B chain. The dashed horizontal lines represents the planes of failure in the two domains in diblock and triblock copolymers.

There have been several prior theoretical studies quantifying the different chain conformations in microphase separated phases of *flexible* multiblock copolymers. Zhulina and Halperin [54] utilized a self-consistent field (SCF) based approach to obtain a scaling of equilibrium bridging fraction (f_{br}) in flexible ABA triblock copolymers as a function of chain length, N. They predicted that the equilibrium bridging fraction was quite small in the strong segregation limit. Spontak et al. [97] modified the calculations of Zhulina and Halperin, and obtained a much higher value for equilibrium bridging fraction in ABA copolymer. Matsen and Schick [98] employed a lattice based SCFT formalism and found that fraction of bridging in lamellar phases of triblock copolymer was typically in the range $f_{br} \approx 0.4$, and had only a weak dependence on the chain length and relative volume fraction of each block. Later studies extended the methodology to study cylindrical and spherical morphologies in triblock copolymers, and found that the results did not depend sensitively on the degree of segregation or the relative volume fraction [99]. Recently, Drolet and Fredrickson adopted a similar SCFT based approach to suggest strategies to modulate the bridging fraction in ABABA pentablock copolymers to potentially optimize the toughness and strength of the material [19].

While much of the above studies have focused on the case of flexible multiblock copolymers, to our knowledge, none of the prior theoretical studies have explicitly addressed the issues of bridging and looping conformations in the more experimentally relevant system of *semicrystalline* multiblock copolymers. While some of the qualitative features of earlier studies are expected to hold equally well for semicrystalline copolymers, the ability of one (or more) of the blocks to crystallize and fold is expected to impact the quantitative details pertaining to the fraction of bridges and loops. A predictive approach to characterize such features is however necessary to optimize the properties in the proposed applications for semicrystalline multiblock copolymers.

In this chapter, we seek to use a simple model to mimic polymer crystallization (elaborated in the next section) to explicitly address the issue of bridge and loop conformations in semicrystalline multiblock copolymers. Our study specifically considers the chain conformations in the lamellar morphologies of ABA, BAB, ABABA and BABAB copolymers (with B representing the crystallizable unit), and demonstrate that chain folding of the semicrystalline unit can have a significant effect (relative to the case of flexible multiblock copolymers) upon the number of bridges in the semicrystalline and flexible domains. Our results underline the importance of accounting for crystallization effects in optimizing the properties of multiblock copolymers, and our model provides a simple framework to do so in the context of more complex morphologies and/or systems involving blends of different copolymers.

The rest of the chapter is arranged as follows: In the next section, we elucidate the important features of our model. We present the mathematical and numerical details in Section III. The section IV focusses on the effect of chain sequence and crystallinity (or rigidity) of B chains on the bridging fractions in triblock and pentablock copolymers. We discuss and compare our observed results with existing theoretical and experimental studies.

4.2 Background and Description of Model

There has been a long history of theoretical models aiming to describe the crystallization of polymers. Broadly speaking, such models can be classified into two categories, viz., equilibrium and kinetic approaches. Equilibrium approaches of polymer crystallization view the phenomenon as one determined by equilibrium thermodynamics of the interplay between polymer conformational statistics, packing effects, and the interchain interactions. One of the earliest such ideas was implemented by Flory who studied the statistical mechanics of a semiflexible chain on a lattice [41]. Flory postulated that chain stiffness and packing entropy are the primary driving forces for polymer crystallization, and that the attractive forces between chain segments (enthalpic effect) only serve to modify the location of the transition. More advanced models invoking lattice approaches [100, 101], density functional formalisms [102, 103], and Monte Carlo simulation approaches [104, 105] have served to refine some of the deficiencies in the Flory's original model and predict more detailed features of polymer crystallization. Kinetic approaches to polymer crystallization on the other hand are motivated by experimental observations which have suggested that in many cases, crystallization of homopolymers results in a kinetically arrested state with morphologies such as folded lamellae or spherulites. Appropriate models and simulations have been developed to explain the characteristics and the growth of such arrested states [106, 107, 108, 109].

In contrast to crystallizable homopolymers, in many situations, semicrystalline block copolymers exhibit equilibrium structures characterized by an interplay between block copolymer microphase separation and the crystallization of one of the components [12, 34, 33, 110]. In such structures, the equilibrium chain folding is set by a compromise between the extended chain configuration favored by the crystalline component [106] and the random coil configuration favored by the amorphous polymer [12, 34]. Depending on the interplay between these features, one could potentially have a scenario where crystallization precedes microphase separation or alternatively the crystallization may occur within the microphase separated morphologies. The earliest theoretical works in this context were based on scaling theories aimed towards determining the domain scaling in semicrystalline diblock copolymers as a function of the degree of polymerization of the two blocks [38, 39]. Subsequently, a self-consistent mean field theory for the folded lamella phase was developed by Whitmore and Noolandi [40], and found slightly different scaling exponents for domain thickness as a function of degree of polymerization than the earlier scaling models. Monte Carlo simulations have also been used to determine the orientation of crystallites inside a semicrystalline diblock copolymer [105].

Self-consistent field theory (SCFT) has emerged as a powerful computational tool to study the equilibrium thermodynamic properties and structure of block copolymer melts, solutions, and semiflexible block copolymers [17, 18, 1, 111]. Since the structure development in semicrystalline block copolymers is an equilibrium process [38], one might hope that an extension of SCFT to crystallizable block copolymers would open up the avenue for *apriori* predictions of the structure (and properties) of multiblock copolymers without requiring one to posit the folded states of the polymer. Unfortunately, this is not a straightforward task since much of the advances in SCFT relies on the assumption that monomer scale packing effects are not relevant in determining the mesoscopic structures of the multicomponent polymers [17]. In contrast, crystallization is a phenomenon where such packing effects play a crucial role in determining both the onset and the structure of the crystallites [102, 103]. While some notable efforts have pursued the idea of developing generalized versions of density functional theories for polymers, such models would require significant numerical effort for maintaining the exploratory nature of SCFT [103, 102]. Consequently, in this study we choose to adopt a model which exhibits characteristics which have similarities to polymer crystallization but nevertheless is tractable enough to effect a numerical solution of the SCFT to obtain information on the chain conformations in multiblock copolymers for calculating bridging fractions.

We model semicrystalline block copolymers as a combination of a flexible rubbery unit (A) and a crystalline unit (B). We assume that the enthalpic interactions between the A and B units can be characterized by a Flory Huggins interaction in the form of a χ parameter which drives their segregation [111]. In line with earlier studies, we adopt the model of a flexible Gaussian chain to model the A polymer. The model we adopt for the B polymer is inspired by the ideas proposed by Flory in the context of homopolymer crystallization and more recently adapted by Frenkel and coworkers in their simulation studies [104, 105, 43]. Specifically, we assume that the B polymer possesses an inherent rigidity which favors chain conformations with some persistence length. Moreover, we also assume that the chain rigidity increases upon lowering the temperature, thereby enhancing the propensity to form extended chain configurations at lower temperatures. While these two ingredients suffice for the block copolymer to form phases with folded B chains (within microphase separated morphologies), in the absence of packing effects, the folds in such chains will not exhibit any translational or orientational order. To improve this deficiency, we assume the existence of an attractive orientational interaction between the B segments in the form of Maier-Saupe potential which favors the formation of parallel bonds [96]. In other contexts [112], preliminary explorations with a more realistic Onsager-type interaction gave qualitatively similar results with however significantly enhanced numerical complexity. Consequently, we decide to adopt the simpler Maier-Saupe potential for results presented in this chapter. With appropriate choices of bending penalty and Maier-Saupe parameter, the semiflexible polymer will undergo isotropic-nematic (I-N) transition upon lowering the temperature [96] which we assign as a signature of the crystallization transition [43].

The above simplifications and rationale lead to the model of semicrystalline block copolymers as a combination of semiflexible and flexible polymer units, with a temperature dependent rigidity and orientational interaction between the semiflexible units. Strictly speaking, upon lowering the temperature our block copolymer model exhibits only a transition to a *smectic phase* rather than a crystalline phase. Capturing the translational order and/or the modeling accurately the density of the crystalline phases however requires incorporating nonlocal packing interactions along the lines of the sophisticated density functional theories mentioned above [102, 103]. However, to maintain numerical simplicity, and moreover since we wish to focus on one-dimensional lamellar phases, as an approximation we neglect such nonlocal packing effects.

However, we also demonstrate in a later section, that our model captures the formation of microphase separated morphologies within which the crystalline component forms folds which are oriented with respect to each other, and allows us to analyze the effect of such conformations on the bridge and loop properties.

We note that there have been prior researches (albeit, motivated on different grounds) on implementing SCFT for models similar to the one we have adopted [112, 111]. Matsen conducted an SCFT study of melt of semiflexible diblock copolymers to understand the effect of rigidity on domain spacing and interfacial width [111]. Duchs and Sullivan adopted an SCFT formalism for dilute solutions of semiflexible diblock copolymers to understand the phase transitions in rod-coil block copolymers [112]. Both these models utilized the wormlike chain description to study semiflexible chains. However, there are subtle differences between our model and previous models. Matsen did not consider orientational interaction between semiflexible segments in the formulation. Duchs et al. utilized Onsager excluded volume interaction (and the absence of any segregative enthalpic interactions) to induce local alignment of polymer chains in contrast to the Maier Saupe potential that we utilize in our model. Moreover, both Matsen and Duchs considered only the case of diblock copolymers (in contrast to the focus on multiblock copolymers) and modeled both components as semiflexible polymers.

4.3 Model and Numerical Details

In this section, we outline the field theoretic formulation for a flexible-semiflexible diblock copolymer. The extension to triblock and pentablock copolymers is straightforward. The SCFT formulation for semiflexible polymer are adapted from earlier theoretical developments [113, 111, 114].

We consider a canonical ensemble of an incompressible melt of n chains of symmetric ($f = 0.5$) flexible(A)-semiflexible(B) diblock copolymer in a volume V. The monomer units of flexible and semiflexible chain are characterized by different statistical length b and a, respectively. For simplicity, each flexible and semiflexible monomer is assumed to have the same monomeric volume, ρ_0^{-1}. The degree of polymerization of the block copolymer is denoted by N. The size asymmetry of the two blocks is denoted by a nondimensional parameter, β ($\equiv aN/b(N/6)^{1/2}$). In the following description, all the lengths are nondimensionalized by the unperturbed radius of gyration ($R_g = b(N/6)^{0.5}$).

The diblock copolymer is parameterized with a continuous variable "s" along the contour of the polymer. The variable "s" is nondimensionalized by the overall degree of polymerization, N. Explicitly, $s = 0$ at the beginning of the flexible A block, $s = f$ at the junction of the two blocks, and $s = 1$ at the end of semiflexible block B. Using this parametrization, the space curves $\mathbf{R}_\alpha(s)$ (where $\alpha = 1, 2, ..., n$ indexes different polymers) are used to describe the different conformations of the polymer. The microscopic nondimensional volume fractions of A, B, and the orientational order parameter for B block are respectively defined as

$$\begin{aligned}
\hat{\phi}_A(\mathbf{r}) &= \frac{N}{\rho_0}\sum_{\alpha=1}^{n}\int_0^f ds\,\delta(\mathbf{r}-\mathbf{R}_\alpha(s)), \qquad (4.1)\\
\hat{\phi}_B(\mathbf{r}) &= \frac{N}{\rho_0}\sum_{\alpha=1}^{n}\int_f^1 ds\,\delta(\mathbf{r}-\mathbf{R}_\alpha(s)),\\
\hat{\mathbf{S}}(\mathbf{r}) &= \frac{N}{\rho_0}\sum_{\alpha=1}^{n}\int_f^1 ds\,\delta(\mathbf{r}-\mathbf{R}_\alpha(s))\left[\mathbf{u}_\alpha\mathbf{u}_\alpha-\frac{\mathbf{I}}{3}\right].
\end{aligned}$$

The overall melt is assumed to be incompressible i.e.,

$$\hat{\phi}_A(\mathbf{r})+\hat{\phi}_B(\mathbf{r})=1. \qquad (4.2)$$

The flexible block is modeled as Gaussian chain which possesses a stretching free energy given by [17, 1]

$$H_0[\mathbf{R}]=\frac{3}{2Nb^2}\sum_{\alpha=1}^{n}\int_0^f ds\left|\frac{d\mathbf{R}_\alpha(s)}{ds}\right|^2. \qquad (4.3)$$

The bending rigidity or the persistence length of the semiflexible B chain is denoted by λ (nondimensionalized by N). It measures the stiffness of the chains and represents the distance along the contour of a semiflexible (worm-like) chain over which the orientational correlations decay [17, 99]. Increasing the rigidity (or decreasing the temperature) favors the extended conformation of the coils. If the vector $\mathbf{u}_\alpha(s)$ denotes the orientation of the αth polymer at contour position s, then the total bending energy for semiflexible component of the block copolymer can be expressed as

$$H_1[\mathbf{R}] = \frac{\lambda}{2}\sum_{\alpha=1}^{n}\int_f^1 ds \left|\frac{d\mathbf{u}_\alpha(s)}{ds}\right|^2. \tag{4.4}$$

The repulsive interactions between the two different types of blocks are quantified using the Flory-Huggins interaction parameter χ, which denotes the enthalpic strength of repulsive interactions. The enthalpic contribution to the free energy is given as

$$H_2[\mathbf{R}] = \frac{-\chi\rho_0}{4}\int d\mathbf{r}[\hat{\phi}_A(\mathbf{r}) - \hat{\phi}_B(\mathbf{r})]^2. \tag{4.5}$$

A key ingredient which mimics the formation of parallel folds in our model is an attractive interaction between parallel segments. Previous studies have included attraction between segments in parallel orientation to describe polymer crystallization in homopolymers and block copolymers [105, 43, 102]. Our model incorporates such an anisotropic interaction by using Maier-Saupe potential, which is a mean-field theory description for modeling anisotropic orientational interactions [96]. The strength of such orientational interactions depend on the parameter Maier-Saupe μ, the magnitude of which quantifies the attraction between oriented segments. Explicitly this interaction term can be written as,

$$H_3[\mathbf{R}] = -\frac{\mu\rho_0}{2}\int d\mathbf{r}\, \hat{\mathbf{S}}(\mathbf{r}) : \hat{\mathbf{S}}(\mathbf{r}). \tag{4.6}$$

The overall partition function for this system can be written as

$$\mathcal{Z} \propto \int \mathcal{D}\mathbf{R}_\alpha(s) d[\mathbf{u}_\alpha(s)] \exp[-\beta(H_0 + H_1 + H_2 + H_3)] \delta[\hat{\phi}_A(\mathbf{r}) + \hat{\phi}_B(\mathbf{r}) - 1]$$
$$\delta\left[\mathbf{u}_\alpha(s) - \frac{1}{aN}\frac{d}{ds}\mathbf{R}_\alpha(s)\right] \delta[|\mathbf{u}_\alpha(s)| - 1]. \tag{4.7}$$

The first delta function in Eq. (4.7) ensures the incompressibility in the system, while the other two delta functions ensure that $\mathbf{u}_\alpha(s)$ is a unit vector, and that each contour segment has fixed length a.

In a field-theoretic framework, quadratic interactions above can be decoupled by introducing fluctuating chemical potential fields conjugate to the density and the orientational order parameters [18]. Self-consistent field equations can subsequently be obtained as a saddle-point of the resulting field equations. Since the details of these transformation are similar to those elaborated in earlier researches, [17, 18] we eschew repeating them here. The result of such an implementation leads to the following equations for the local volume fractions of A and B components, $\phi_A(\mathbf{r})$ and $\phi_B(\mathbf{r})$, and the local orientational order parameter $\mathbf{S}(\mathbf{r})$:

$$\begin{aligned}
\phi_A(\mathbf{r}) &= \frac{1}{Q}\int_0^f ds\, q_A(\mathbf{r}, s) q_A^\dagger(\mathbf{r}, 1-s), \qquad (4.8)\\
\phi_B(\mathbf{r}) &= \frac{4\pi}{Q}\int_f^1 ds \int d\mathbf{u}\, q_B(\mathbf{r}, \mathbf{u}, s) q_B^\dagger(\mathbf{r}, \mathbf{u}, 1-s),\\
\mathbf{S}(\mathbf{r}) &= \frac{4\pi}{Q}\int_f^1 ds \int d\mathbf{u}\, q_B(\mathbf{r}, \mathbf{u}, s)\left(\mathbf{u}\mathbf{u} - \frac{\mathbf{I}}{3}\right) q_B^\dagger(\mathbf{r}, \mathbf{u}, 1-s).
\end{aligned}$$

In the above, $q_A(\mathbf{r}, s)$ represents the statistical weight for an A chain of length "s" in an external potential field $W_A(\mathbf{r})$ to have its end at position $\mathbf{r}$, and satisfies the equation:

$$\frac{\partial}{\partial s} q_A(\mathbf{r}, s) = \nabla^2 q_A(\mathbf{r}, s) - W_A(\mathbf{r}) q(\mathbf{r}, s); \quad q_A(\mathbf{r}, s = 0) = 1 \tag{4.9}$$

$q_B(\mathbf{r}, \mathbf{u}, s)$ represents the end-segment distribution function for a B polymer of length "s" to have its end at position $\mathbf{r}$, with orientation $\mathbf{u}$ [17, 111] in an external potential field $W_B(\mathbf{r})$ and an orientational tensor field $\mathbf{M}(\mathbf{r})$ and satisfies a modified diffusion equation of the form:

$$\begin{aligned} \frac{\partial}{\partial s} q_B(\mathbf{r}, \mathbf{u}, s) = -\beta \mathbf{u} . \nabla q_B(\mathbf{r}, \mathbf{u}, s) - \left(W_B(\mathbf{r}) - \mathbf{M}(\mathbf{r}) : \left[\mathbf{u}\mathbf{u} - \frac{\mathbf{I}}{3} \right] \right) q_B(\mathbf{r}, \mathbf{u}, s) \\ + \frac{1}{2\lambda} \nabla^2_{\mathbf{u}} q_B(\mathbf{r}, \mathbf{u}, s); \quad q_B(\mathbf{r}, \mathbf{u}, s = f) = \frac{q_A(\mathbf{r}, s = f)}{4\pi}. \end{aligned} \tag{4.10}$$

$q_A^\dagger(\mathbf{r}, s)$, and $q_B^\dagger(\mathbf{r}, \mathbf{u}, s)$ are analogous to $q_A(\mathbf{r}, s)$, and $q_B(\mathbf{r}, \mathbf{u}, s)$ respectively, except that s is measured from the other end (beginning of semiflexible B chain). The initial conditions for these end-segment distribution functions are defined as

$$\begin{aligned} q_B^\dagger(\mathbf{r}, \mathbf{u}, s = 0) &= \frac{1}{4\pi}, \\ q_A^\dagger(\mathbf{r}, s = f) &= \int d\mathbf{u} \, q_B^\dagger(\mathbf{r}, \mathbf{u}, s = f). \end{aligned} \tag{4.11}$$

$\mathcal{Q}$ represents the single chain partition function which is calculated as

$$\mathcal{Q} = \frac{1}{V}\int d\mathbf{r}\int d\mathbf{u}\, q_B(\mathbf{r},\mathbf{u},s) \tag{4.12}$$

The self-consistency aspect of the above equations is ensured by postulating that the potential fields $W_A(\mathbf{r}), W_B(\mathbf{r})$, and $\mathbf{M}(\mathbf{r})$ are in turn related to $\phi_A(\mathbf{r}), \phi_B(\mathbf{r})$ and $\mathbf{S}(\mathbf{r})$ through:

$$\begin{aligned} \frac{1}{\chi N}[W_B(\mathbf{r}) - W_A(\mathbf{r})] &= \phi_A(\mathbf{r}) - \phi_B(\mathbf{r}) \\ 1 &= \phi_A(\mathbf{r}) + \phi_B(\mathbf{r}) \\ \frac{1}{\mu N}\mathbf{M}(\mathbf{r}) &= \mathbf{S}(\mathbf{r}). \end{aligned} \tag{4.13}$$

4.3.1 Expansion in Spherical Harmonics

To evaluate the single chain partition function($\mathcal{Q}$) (Eq. (4.12)), volume fraction ($\phi_B(\mathbf{r})$) (Eq. (4.9)), and orientational order parameter ($\mathbf{S}(\mathbf{r})$) (Eq. (4.9)) for the semiflexible B block, we need to solve for the diffusion equation for $q_B(\mathbf{r},\mathbf{u},s)$, and $q_B^{\dagger}(\mathbf{r},\mathbf{u},s)$ (Eq. (4.10)). For this purpose, we expand the orientation dependencies of these end segment distribution functions in spherical harmonics (Strictly speaking, for the one dimensional morphologies considered in this chapter, an expansion in Legendre polynomials would suffice). However, to maintain generality, we present the appropriate equations in the full three dimensional space: [112, 115]

$$q_B(\mathbf{r},\mathbf{u},s) = \sum_{l,m} q_{lm}(\mathbf{r},s)Y_{l,m}(\mathbf{u}); \quad q_B^\dagger(\mathbf{r},\mathbf{u},s) = \sum_{l,m} q_{lm}^\dagger(\mathbf{r},s)Y_{l,m}(\mathbf{u}). \quad (4.14)$$

The initial condition for the coefficients are $q_{lm}(\mathbf{r}, s = f) = (1/\sqrt{4\pi})q_A(\mathbf{r}, s = f)\delta_{l0}\delta_{m0}$. On expanding the differential equation for $q_B(\mathbf{r},\mathbf{u},s)$ in spherical harmonics, we obtain

$$\begin{aligned}\frac{\partial q_{lm}(\mathbf{r},s)}{\partial s} &= -\beta \sum_{l',m'} \sqrt{\frac{2l'+1}{2l+1}} C^{1,l',l}_{0,0,0} \left[C^{1,l',l}_{0,m',m} \frac{\partial}{\partial z} + \frac{1}{\sqrt{2}}(C^{1,l',l}_{-1,m',m} - C^{1,l',l}_{1,m',m}) \frac{\partial}{\partial x} \right. \\ &\quad \left. + \frac{i}{\sqrt{2}}(C^{1,l',l}_{-1,m',m} + C^{1,l',l}_{1,m',m}) \frac{\partial}{\partial y} \right] q_{l'm'}(\mathbf{r},s) - \frac{N}{2\lambda}(l)(l+1)q_{lm}(\mathbf{r},s) \\ &\quad - W_B(\mathbf{r})q_{lm}(\mathbf{r},s) + \sum_{l',m'} \mathbf{M} : \mathbf{A}\, q_{l'm'}(\mathbf{r},s).\end{aligned} \quad (4.15)$$

$C^{l'',l',l}_{m'',m',m}$ above denote the Clebsch-Gordan coefficients.[112, 115] The elements of the symmetric matrix $\mathbf{A}$ are:

$$\begin{aligned}
A_{11} &= \sqrt{\frac{2l'+1}{2l+1}} C^{2,l',l}_{0,0,0} \left[\frac{1}{\sqrt{6}} \left(C^{2,l',l}_{-2,m',m} + C^{2,l',l}_{2,m',m} \right) - \frac{1}{3} C^{2,l',l}_{0,m',m} \right] \\
A_{22} &= -\sqrt{\frac{2l'+1}{2l+1}} C^{2,l',l}_{0,0,0} \left[\frac{1}{\sqrt{6}} \left(C^{2,l',l}_{-2,m',m} + C^{2,l',l}_{2,m',m} \right) + \frac{1}{3} C^{2,l',l}_{0,m',m} \right] \\
A_{33} &= \frac{2}{3} \sqrt{\frac{2l'+1}{2l+1}} C^{2,l',l}_{0,0,0} C^{2,l',l}_{0,m',m} \\
A_{12} &= \frac{i}{\sqrt{6}} \sqrt{\frac{2l'+1}{2l+1}} C^{2,l',l}_{0,0,0} \left[C^{2,l',l}_{-2,m',m} - C^{2,l',l}_{2,m',m} \right] \\
A_{13} &= \frac{1}{\sqrt{6}} \sqrt{\frac{2l'+1}{2l+1}} C^{2,l',l}_{0,0,0} \left[C^{2,l',l}_{-1,m',m} - C^{2,l',l}_{1,m',m} \right] \\
A_{23} &= \frac{i}{\sqrt{6}} \sqrt{\frac{2l'+1}{2l+1}} C^{2,l',l}_{0,0,0} \left[C^{2,l',l}_{-1,m',m} - C^{2,l',l}_{1,m',m} \right].
\end{aligned} \tag{4.16}$$

The single chain partition function is then evaluated as

$$\mathcal{Q} = \frac{\sqrt{4\pi}}{V} \int d\mathbf{r}\, q_{00}(\mathbf{r}, 1), \tag{4.17}$$

and the local volume fractions and orientational order parameter fields are calculated as

$$\begin{aligned}
\phi_B(\mathbf{r}) &= \frac{4\pi}{\mathcal{Q}} \int_f^1 ds \sum_{l,m} (-1)^m q_{lm}(\mathbf{r}, s) q^{\dagger}_{lm}(\mathbf{r}, 1-s), \\
\mathbf{S}(\mathbf{r}) &= \frac{4\pi}{\mathcal{Q}} \int_f^1 ds \sum_{l,m} \sum_{l',m'} (-1)^{m'} \mathbf{A} q_{lm}(\mathbf{r}, s) q^{\dagger}_{l'm'}(\mathbf{r}, 1-s).
\end{aligned} \tag{4.18}$$

This formulation of diffusion equation for semiflexible chain is quite similar to the one adopted by Duchs et al.[112], except for the appearance of $\mathbf{M}(\mathbf{r})$ (arising from Maier-Saupe potential), instead of an Onsager term in their treatment.

4.3.2 Numerical Implementation

Daoulas et al. [113] pointed out numerical instability issues with forward time-centered scheme (FTCS) adopted in the earlier work [112]. Therefore, we utilize the Lax-Wendroff numerical scheme suggested by Daoulas et al.[113, 116] to solve for the coefficients $q_{lm}(\mathbf{r}, s)$ for a specified values of the potential fields ($W_B(\mathbf{r})$, $\mathbf{M}(\mathbf{r})$). We utilized Crank-Nicholson scheme to numerically integrate the modified diffusion equation for propagators for the flexible coil, $q_A(\mathbf{r}, s)$ and $q_A^\dagger(\mathbf{r}, s)$ [93]. The contour discretization (normalized by N) along the flexible polymer was chosen to be 0.0025, while the contour discretization (normalized by N) along the semiflexible chain was chosen to be in the range 6.25×10^{-4}-0.001. The space discretization (normalized by R_g) was chosen to be 0.066.

The self-consistent potential fields $W(\mathbf{r})$, $\pi(\mathbf{r})$, and $\mathbf{M}(\mathbf{r})$, Eq. (4.13) are solved to achieve self-consistency are obtained by using a real-space approach developed by Fredrickson and coworkers [18]. The pseudo evolution equations involved in the scheme are:

$$\begin{aligned}
\frac{\partial W_A(\mathbf{r})}{\partial t} &= -\lambda_{WA}(W_A(\mathbf{r}) - \chi N(\phi_B(\mathbf{r}) + \pi(\mathbf{r})), \qquad (4.19) \\
\frac{\partial W_B(\mathbf{r})}{\partial t} &= -\lambda_{WB}(W_B(\mathbf{r}) - \chi N(\phi_A(\mathbf{r}) + \pi(\mathbf{r})), \\
\frac{\partial \pi(\mathbf{r})}{\partial t} &= \lambda_\pi[1 - \phi_A(\mathbf{r}) - \phi_B(\mathbf{r})], \\
\frac{\partial \mathbf{M}(\mathbf{r})}{\partial t} &= -\lambda_M \left(\frac{\mathbf{M}(\mathbf{r})}{\mu N} - \mathbf{S}(\mathbf{r}) \right).
\end{aligned}$$

where λ_{WA}, λ_{WB}, λ_π, and λ_M are fictitious mobility coefficients. Iteration of the above equations results in the equilibrium values of self-consistent potentials ($W_A(\mathbf{r})$, $W_B(\mathbf{r})$, $\pi(\mathbf{r})$, and $\mathbf{M}(\mathbf{r})$), and hence, the volume fraction and orientation fields for a given periodic box size. The equilibrium density profiles are obtained by effecting this procedure over different box sizes to obtain the configuration with the lowest free energy.

4.3.3 Calculation of Bridge and Loop Fractions

The procedure for calculating the looping/bridging fractions in multiblock copolymers is adapted directly from the earlier researches of Matsen [98], and Drolet and Fredrickson [19]. To maintain brevity, we refer the reader interested in the details to the original articles.

4.4 Results and Discussion

Our study aims to shed light on the chain conformations, specifically, the bridging and looping fractions in the models of semicrystalline multiblock copolymers studied in recent experiments [53, 11, 117, 52]. Specifically, our interest is in shedding light on the question "how does the formation of oriented foldlike conformations affect the bridging and looping fractions in different sequences of multiblock copolymers ?" In our model, the formation of folds and their orientation is driven by an interplay of the chain rigidity λ (Eq. (4.4)) and the Maier-Saupe interaction parameter, μ (Eq. (4.6)). We seek to answer the preceding question in a systematic manner by studying the effect of stiffness of the chain upon bridging fractions in different sequences of multiblock copolymers. In this manner, we are able to probe the transition from the limit of "flexible" block copolymers to the limit of "crystallizable" block copolymers. We will demonstrate that this transition has interesting consequences for the bridging fractions of both the flexible and the semiflexible component.

The self-assembly behavior of the model elaborated in the previous section is governed by a number of parameters: Flory-Huggins interaction parameter (χN), Maier-Saupe parameter (μN), chain rigidity (λ), size asymmetry ratio of the two monomers (β), and the relative volume fractions of different A and B blocks. In the next section we demonstrate that the effects of chain folding and crystallization may be studied by varying the rigidity (λ) of the semiflexible polymer B. Consequently, our results keep χN and μN fixed and while considering only values of μN for which the orientational (crystallization) transition occurs within the self-assembled morphologies, probe the role of λ upon the different chain conformations. Since we consider density inhomogeneities in only one direction, we are concerned only with formation of lamellar morphologies. In all the cases we studied, the nematic ordering in semiflexible B block was observed to be in the direction perpendicular to the lamellar interface.

Preliminary to discussing bridge and loop properties of multiblock copolymers, we present a brief discussion of the density and orientational order profiles in semicrystalline *diblock* copolymers. Much earlier work has been accomplished in the context of both flexible and semicrystalline diblock copolymers, and it proves of interest to compare the results of our model with these earlier predictions [38, 40].

4.4.1 Diblock copolymers

We first present results illustrating the manner by which our model mimics the qualitative features of crystallization in block copolymers. For this purpose, we probe the role of the parameter χN while keeping the ratios $\mu N/\chi N$ and $\lambda/\chi N$ fixed. Since the interaction parameter χN can be viewed as a measure of inverse temperature, this protocol mimics the scenario of structure development upon lowering the temperature. Fixing the ratios of $\mu N/\chi N$ and $\lambda/\chi N$ is designed to mimic the enhancements in both the rigidity and the tendency to form oriented bonds upon lowering the temperature. In Fig. (4.2), we display the volume fraction profiles of A ($\phi_A(\mathbf{r})$), B ($\phi_B(\mathbf{r})$) segments and the orienta-

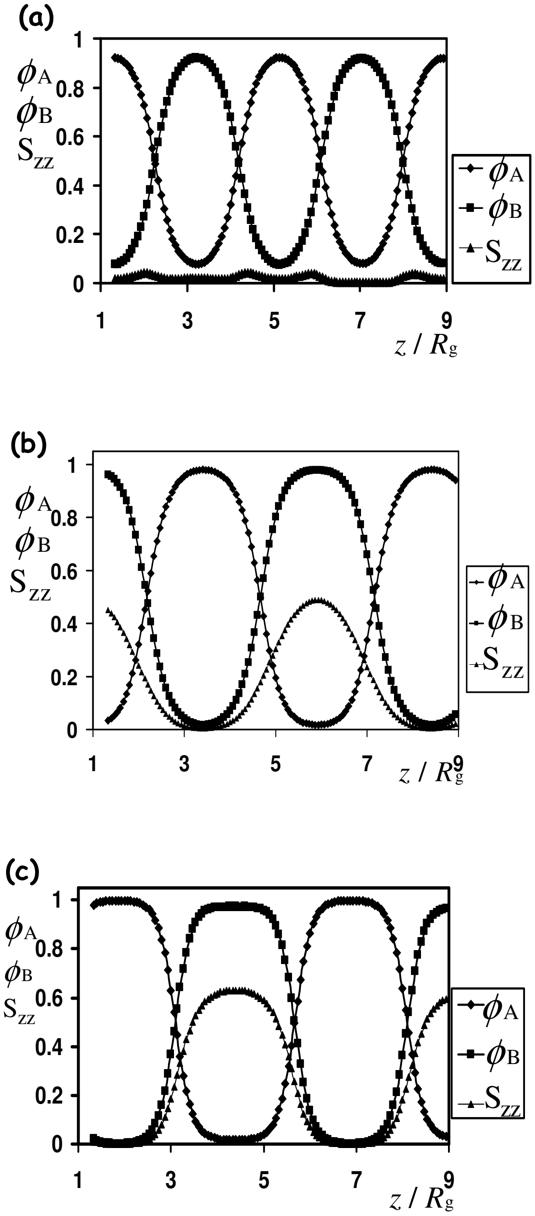

Figure 4.2: Density and orientational order parameter for fixed $f = 0.50$, $\mu/\chi = 3$, $\beta = 6$. and $\lambda/\chi N = 0.03$. As we increase the value of χN (or equivalently decrease T), we observe orientational order growing inside the semiflexible polymer, and consequently the domain size increases. The orientational order parameter for these 3 values of χN are, $\mathbf{S} \approx 0$ ($\chi N = 13$), $\mathbf{S} = 0.43$ ($\chi N = 14$) and $\mathbf{S} = 0.59$ ($\chi N = 17$). This observation is akin to crystallization within lamellar morphologies.

tional order parameter ($S_{zz}(\mathbf{r})$) in the semiflexible domain (B) for $\chi N = 13, 14$ and 17. Since nematic ordering in our simulations is completely along z-axis (or perpendicular to lamellar interface), orientational order is quantified by the zz component of the orientational order tensor (refer Eq. (4.9)). We observe that upon increasing χN, the semiflexible B domain undergoes an isotropic-nematic transition leading to the formation of an oriented B phase. Moreover, we observe that there is correspondingly an increase in the domain size of the B phase which indicates the formation of extended chain conformations. Upon further increasing the value of χN (or decreasing T), we observe that there is a further increase in the amount of orientational ordering within the semiflexible domains.

The above features qualitatively mimic the behavior observed in semicrystalline diblock copolymers. Indeed, in the scenario where crystallization occurs at a temperature lower than microphase separation transition, the domain spacing is expected to show a jump at the onset of crystallization [32, 12]. Moreover, crystallization leads to the formation of a strongly oriented B chains, an effect qualitatively mimicked by the nematic phase formed by our semiflexible chains.

We point out that the morphological effects seen in Fig. 4.2 can also be realized by considering a situation involving a fixed value of χN and orientational interaction μN, while changing the persistence length of the semiflexible block λ. In Fig. 4.3, we display representative results for the density profiles of A ($\phi_A(\mathbf{r})$) and B ($\phi_B(\mathbf{r})$) segments and the orientational order parameter

($S_{zz}(\mathbf{r})$) in the semiflexible domain (B) for two different values of chain rigidity, $\lambda = 0.036$ and $\lambda = 0.36$. For the lower value of λ (refer Fig. 4.3(a)), we observe that the density and orientational profiles resemble the results observed at high temperatures (refer Fig. 4.2(a) for $\chi N = 13$). In contrast, for the higher λ, we observe that the density and orientational profiles resemble the results observed for lower values of temperature (refer Fig. 4.2(c) for $\chi N = 17$). Based on these results, in the subsequent results we use λ as the control parameter to probe the role of crystallization upon the bridge and loop conformations in multiblock copolymers.

While the above results demonstrated qualitative correspondence between our model predictions and the crystallization phenomena, it is natural to probe the degree of quantitative conformance between our model and crystallization. Explicitly, we choose to consider the scaling of the domain sizes as a function of the volume fraction of the flexible component. In flexible diblock copolymers, the domain size is determined by the competition between entropic penalty associated with stretching of chains and interfacial energy [6]. On increasing the rigidity of B chains (i. e. transitioning from flexible to semiflexible polymers), the entropic penalty associated to extend over a distance D reduces, leading to an increase in the domain size. To render these physical considerations in quantitative terms, we consider the case of flexible diblock copolymers with a volume fraction f of A component and $1 - f$ of B component. In the limit of strong segregation, brush-like scaling theories can be adopted to estimate the respective domain sizes D_A and D_B of A and B

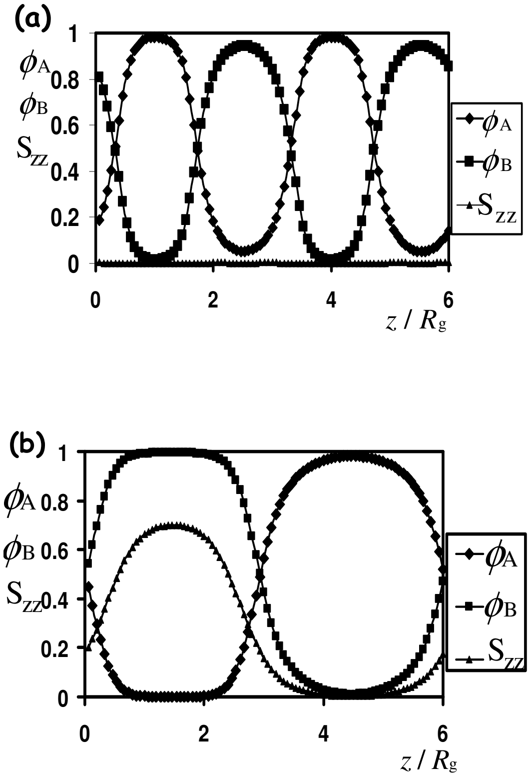

Figure 4.3: Density and orientational order parameter for low and high values of chain rigidity, λ. The parameters are $\chi N = 18$, $\mu N = 54$, $f = 0.50$, and $\beta = 6$. The values of λ are a. 0.036, b. 0.36. The orientational order parameter for these 2 values of χN are, $\mathbf{S} \approx 0$ ($\chi N = 12$), and $\mathbf{S} = 0.68$ ($\chi N = 18$).

components. Explicitly, by incompressibility requirement we have,

$$\rho_0 D_A A = Nf; \rho_0 D_B A = N(1-f), \tag{4.20}$$

where ρ_0 represents the monomeric density of A and B components and A denotes the area per chain in the lamellar phases. For flexible block copolymers, the free energy per chain in the lamellar phase can be estimated as:

$$\beta F \sim \frac{D_A^2}{Nfb^2} + \frac{D_B^2}{N(1-f)b^2} + \gamma A, \tag{4.21}$$

where b is the Kuhn segment length of the two chains, and γA is the interfacial energy between the two immiscible blocks. Substituting Eq. (4.20) into Eq. (4.21), and minimizing the free energy over the area per chain (A) leads to

$$A \sim \left(\frac{N}{\rho_0^2 b^2 \gamma}\right)^{1/3}. \tag{4.22}$$

Substituting the above value of A into Eq. (4.20), we obtain the overall domain size as *independent* of volume fraction of flexible block:

$$D \sim \frac{N^{2/3}}{\rho_0^{1/3}}(b^2\gamma)^{1/3}. \tag{4.23}$$

For estimating the expected domain sizes for semicrystalline diblock copolymers we utilize scaling arguments similar to the one used by DiMarzio et al. [38] based on a schematic of an *ideal* semicrystalline diblock copolymer where the B chain forms perfectly folded lamellae. We denote by n_f the number of folds in B chain, and ϵ as the energy needed to form one fold. The free energy per chain for the depicted situation is given as:

$$\beta F \sim \frac{D_A^2}{Nfb^2} + \gamma A + n_f \epsilon \tag{4.24}$$

Here, the area per chain in Eq. ((4.20)) scales as $A \sim n_f b^2$, and we obtain

$$\beta F \sim \frac{Nf}{\rho_0^2 n_f^2 b^6} + (\gamma + \epsilon/b^2) n_f b^2. \tag{4.25}$$

Minimizing the free energy over number of folds leads to

$$n_f \sim \left(\frac{Nf}{(\gamma + \epsilon/b^2) b^8 \rho_0^2} \right)^{1/3}, \tag{4.26}$$

and an overall domain spacing (D)

$$D = D_A + D_B \sim \frac{N}{\rho n_f b^2} \sim N[Nf]^{-1/3} \left[(\gamma + \epsilon/b^2) b^2 \rho_0^2 \right]^{1/3} \tag{4.27}$$

A significant difference between the characteristics of Eq. (4.27) and Eq. (4.23), is the dependence of the domain spacing of the semicrystalline copolymers upon the degree of polymerization of the flexible block (Nf). We note that the scaling exponent $-1/3$ is identical to the exponent predicted by DiMarzio et al.[38] A later study by Whitmore and Noolandi used SCFT modeling to calculate the domain scaling dependency on fN, and predicted $\alpha = -5/12$. Evaluation of domain scaling as a function of degree of polymerization of flexible block has been focus of many experimental investigations also, and have obtained values of α close to the theoretically obtained ones [110, 34]. In our study, we focused on the progression in scaling from the flexible limit (Eq. (4.23)) to the semicrystalline case (Eq. (4.27)), and whether such a progression can indeed be observed in our model for semicrystalline copolymers.

In Fig. 4.4, we plot the variation of overall domain spacing from our model of flexible-semiflexible diblock copolymers as a function of length of the flexible block (on a log-log scale) for different values of λ. We observe the results for the domain spacing are unfortunately not conclusive enough to extract a power law behavior (we note that experiments have also come to similar conclusions [34]). This may be due to our parameters not necessarily being in the strong segregation regime (which requires significantly large values of χN) where such brush-like scaling laws are expected to apply. Nevertheless, in an effort to effect a comparison with the above predictions, we fit the data by a power law and extracted an exponent which is displayed in the figure. We observe that for very low values of λ, the domain spacing is practically independent of f as expected from the above scaling arguments for flexible block copolymers. Upon increasing the value of rigidity, we observe that domain spacing exhibits a value of scaling exponent in the range -0.33 to -0.37 consistent with the scaling analysis provided for semicrystalline diblock copolymers above.

The above correspondences, between the qualitative phenomena and the quantitative scaling predictions for semicrystalline block copolymers [38, 40] on the one hand and our numerical results for the flexible-semiflexible copolymer system on the other hand, suggests that our model can serve as a reasonable approach to study the conformational properties of semicrystalline multiblock copolymers.

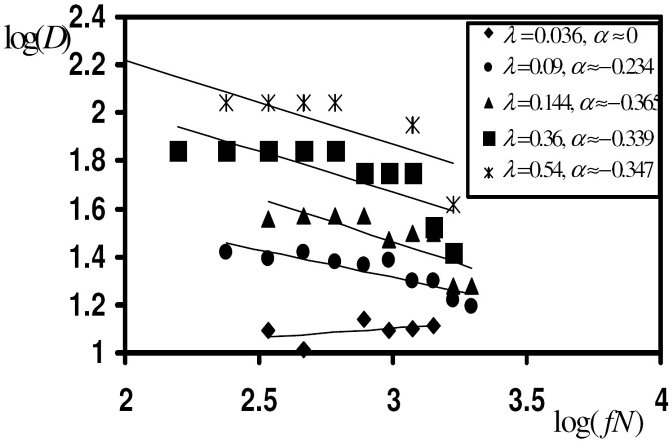

Figure 4.4: Scaling exponents of D as a function of fN for different values of rigidity, λ. The values of the other parameter are : $\chi N = 18$, $\mu/\chi = 3$, and $\beta = 6$. α represents the scaling exponent for domain spacing as a function of degree of polymerization of the flexible block. The straight lines represents the linear fit to the data points of domain scaling. Slope of these lines is used to evaluate the scaling exponent, α. (The plots are shifted on the y-axis to provide a better clarity, but it does not affect the slope of this log-log plot.)

4.4.2 Triblock Copolymers

In this section, we present results pertaining to bridging fractions in triblock copolymers. We considered both ABA and BAB sequences of triblock copolymers, with the midblock volume fraction set at $f = 0.5$ and the end block volume fraction set at 0.25. The results of the preceding section suggests that the persistence length of the semiflexible polymer serves as a probe of the effects one may expect in transitioning from the flexible multiblock copolymer to the semicrystalline copolymer limit. Based on this rationale, the first issue we consider is the effect of the persistence length upon the bridging fractions in these triblock copolymers. Figure 4.5 shows the variation of the bridging fraction of the center block in ABA and BAB triblock copolymers as a function of the rigidity (λ) of the semiflexible B chain. Also shown in the figure are the bridging fractions for the case of a symmetric *flexible* triblock copolymer (denoted as ABA (f)) [98]. At low values of λ, the bridging fractions for these three different categories of triblock copolymer are identical, confirming their conformational equivalence for small values of persistence lengths. It has been theoretically predicted that for the case of flexible triblock copolymer, the equilibrium bridging fraction lies in the range, $f_{br} \approx 40 - 45\%$ [98, 99]. Experimentally, the value of equilibrium bridging fraction ($f_{br} \approx 40\%$) has also been confirmed for lamellar triblock copolymers [118]. Our results (cf. Fig. 4.5) do conform to these theoretical/experimental results for low values of chain rigidity λ.

More interestingly, it is observed that increasing the rigidity leads to a substantial increase in the bridging fraction for the case of ABA triblock copolymers. This increase is manifested as an almost complete bridging observed at the highest values of λ. In contrast, for BAB triblock copolymers, increasing the persistence length of the B chain is seen to lead to a reduction in the midblock bridging fraction in the A domains, and at highest values of λ,

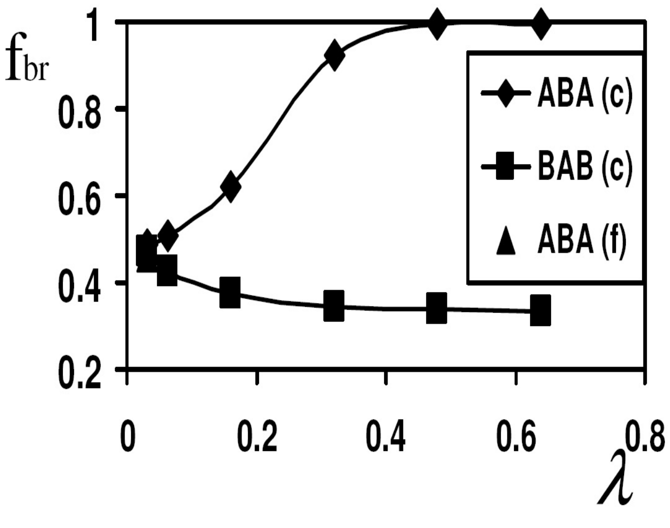

Figure 4.5: The bridging volume fraction plotted as a function of persistence length λ for ABA and BAB. The filled triangle represents the value of f_{br} for a flexible ABA triblock copolymer. The parameters for this case are : $\chi N = 32$, $f = 0.50$, $\mu N = 80$, and $\beta = 12$.

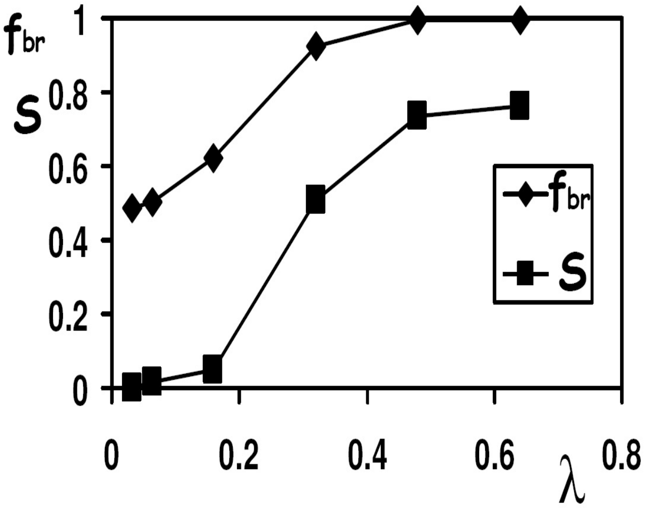

Figure 4.6: Correlation between bridging fraction and nematic order parameter of the midblock chain in ABA triblock copolymer. The parameters are same as the one used in Fig. 4.5.

it is observed that the bridging fraction apparently plateaus out to a reduced value. We note that an independent study of Li and Ruckenstein [119] calculated the equilibrium bridging fractions for lamellar, cylindrical, and spherical phases of the ABA triblock copolymer as a function of the chain stiffness. They also found that the bridging fraction increases with increasing stiffness of the midblock chain. However, the values of bridging fraction calculated by them for lamellar phases ($\approx 20\%$) are significantly lower than our calculated values ($\approx 90\%$).

An interesting question relates to the origins underlying the impact of the rigidity of the B block upon the bridging fractions in ABA and BAB triblock copolymers. First we discuss the case of ABA triblock copolymers, and point out that for the orientational interaction parameters chosen for our numerical results, the semiflexible block undergoes isotropic-nematic (I-N) transition on increasing the value of rigidity. This is clearly seen in Fig. 4.6 which displays the nematic order parameter $\mathbf{S}$ (which quantifies the degree of orientational ordering in the semiflexible chains) as a function of λ. Qualitatively this result reflects the fact that increasing the rigidity of the chain decreases the tendency for the chain to bend, hence favors the formation of nematic phases. Interestingly, a depiction of f_{br} in the same plot displays a strong correlation between and nematic ordering and the fraction of bridges in the system. This correlation provides a mechanistic origin for the increased bridging fractions, and can be rationalized by invoking the results of Halperin and coworkers who considered the formation of hairpin like defects of semiflexible polymers in nematic phases [120, 121]. Explicitly, Halperin *et al.* argue that effective energy for forming a hairpin defect in semiflexible polymers scales as $U_h \simeq (S\epsilon)^{1/2}$, where ϵ is the rigidity of the chain, and S represents nematic order parameter [120]. They predict that due to the unfavorable nature of such defects, the effective elasticity of the chain parallel to the nematic field is much lower (by a factor of $\exp(-U_h)$) than in the isotropic phase. Together, these effects make it more easier for a semiflexible chain to form a bridge in the nematic phase (relative to both flexible chains as well as semiflexible chains in an isotropic phase). In fact, Halperin and Williams predict an increase in the bridging fraction scaling as $\exp(\alpha U_h)$ (where α denotes a scaling exponent) which qualitatively explains the strong correlation between the S parameter and f_{br} [120]. In sum, the formation of a nematic (crystalline) phase by the semiflexible (crystalline) block reduces the propensity for the formation of folds and is responsible for the observed enhancement in bridging fractions in the B domain.

In contrast to the situation of ABA copolymers, bridging in BAB polymers relates to bridging of the flexible block, and hence our numerical results can be understood by invoking considerations for flexible polymers. While accurate analytical expressions do not exist for the parametric dependencies of bridging fractions of flexible polymers (due to the subtle entropic differences between bridges and loop conformations), approximate scaling arguments suggest that $f_{br} \propto H^{-\nu}$, where H represents the domain width (or the plate separations for interplate bridging by grafted chains) with $\nu \simeq 1/2 - 2/3$

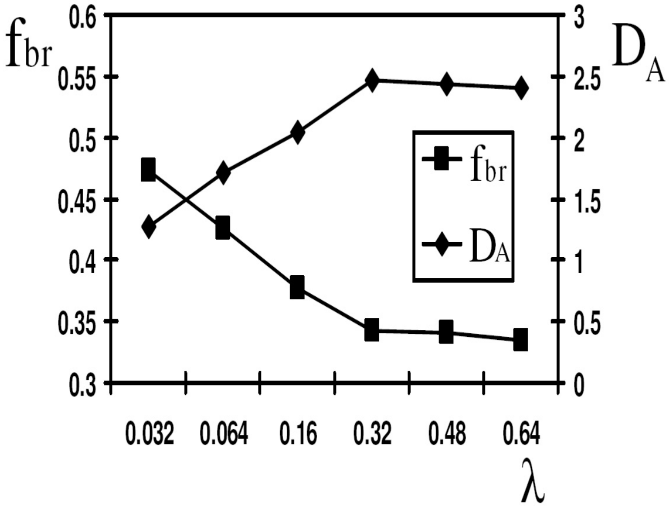

Figure 4.7: Correlation between the bridging fraction of A domain in BAB copolymer and the domain size of the flexible block (D_A). With increasing persistence length the domain size increases, while the bridging fraction (f_{br}) decreases.

[121, 54]. Physically, the preceding result suggests that an increased domain spacing leads to a corresponding decrease in the bridging fraction. This may be understood as a consequence of the enhanced conformational entropy cost of forming a bridge between interfaces which are further apart, and has also been qualitatively observed in an earlier work by Matsen in the context of increasing domain size due to increasing segregation between the copolymers [98]. We believe that this effect explains the decrease of bridging fraction with increasing rigidity for BAB triblock copolymer as shown in Fig. 4.7. Indeed, as we observed in the preceding section, an increase in λ of the B block, leads to an increase in the domain spacing of the A phase (refer Eq. (4.27)). As shown in Fig. 4.7 this effect also holds in the context of the domain spacings

of the BAB triblock copolymers. Not surprisingly, a depiction of f_{br} on the same plot shows a strong correlation to the domain spacing and confirms our hypothesis regarding their correlation.

To summarize, we observe that increasing the rigidity of the B chain can impact the bridging properties of ABA and BAB triblock copolymers in a contrastingly different manner. Based on comparison of the two types of triblock copolymer, it is concluded that ABA triblock sequence demonstrates higher bridging of different A-B domains than the BAB triblock sequence for the same relative volume fractions, and the same value of rigidity of the B chain. These results suggest that if the objective is to enhance the bridging fractions in A domain, then it is a better strategy to link the A block to a noncrystallizable B block. In contrast, if the objective is to increase the bridging fractions in the B domain, then it is more prudent to use crystallizable blocks which offer superior bridging characteristics.

4.4.3 Pentablock Copolymers

While triblock copolymers offer advantages arising from the mid-block bridging, they suffer from the disadvantage that the end blocks cannot bridge. Consequently, lamellar phases of triblock copolymers have bridged domains alternating with non-bridged domains (shown in Fig. 4.1). In contrast, pentablock copolymers (both ABABA and BABAB sequences) offer the possibility for bridging conformations in both A and B blocks and hence in both A and B domains. However, despite this difference the qualitative and quantitative de-

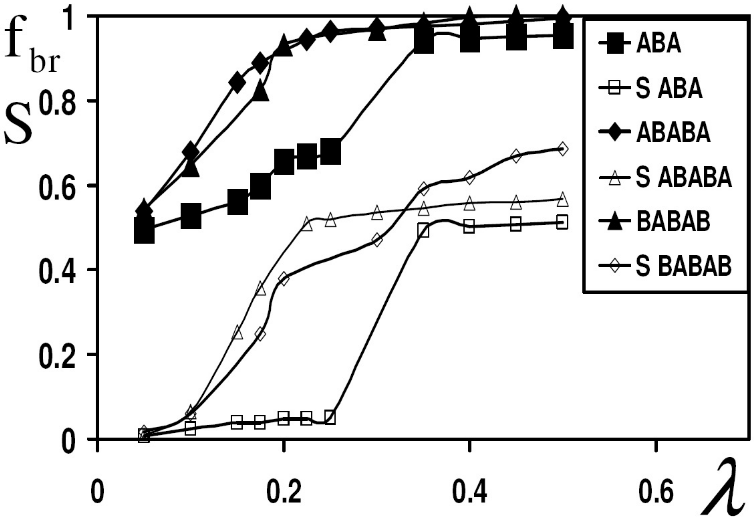

Figure 4.8: Bridging fractions in B domains of ABA, ABABA and BABAB copolymers. The parameters are $\chi N_{penta} = 50$, $\chi N_{tri} = 50$, $\beta = 12$, and $\mu/\chi = 2.5$. Both the sequences of pentablock copolymers are symmetric and posses equal volume fractions of A and B, i.e. $f_1 = f_5 = 0.125$, and $f_2 = f_3 = f_4 = 0.25$. The variation of bridging fraction as a function of rigidity is qualitatively similar for both triblock and pentablock copolymers irrespective of the nature of the sequence.

tails of bridging in the A and B blocks of the pentablock copolymer can be expected to be very similar to that of the triblock copolymer. Explicitly, in a BABAB pentablock copolymer (with average volume fractions of the blocks denoted $f_1 - f_2 - f_3 - f_4 - f_5$), we expect only a maximum fraction f_3/f_B of the B polymers to bridge in a given B domain. Hence, when measured relative to this fraction, we expect that the bridging fraction of B polymers (and its dependence on the rigidity λ), to be quantitatively comparable to those observed in ABA triblock copolymers. Likewise, in the same BABAB polymeric sequence, we similarly expect the bridging fractions of A polymer measured relative to the total fraction of "bridgeable" chains in A ($f_2 + f_4$) domains to be quantitatively comparable to the results observed for BAB triblock copolymers.

The above expectations are confirmed in Fig. 4.8, where we display our SCFT results for B bridging fractions of symmetric ABABA and BABAB (normalized by f_3/f_B) pentablock copolymers and compare them with the corresponding results for the ABA triblock copolymers. The degree of polymerization for pentablock copolymer is kept twice that of the triblock copolymer. To facilitate a quantitative comparison, we have set the parameter $\chi N = 50$ for pentablock copolymers and $\chi N = 25$ for triblock copolymers. The latter usually provides a satisfactory set point for establishing similar degrees of segregations in tri and pentablock copolymers. Fig. 4.9 portrays a similar representation for the A bridging fraction and compares it with the results for the BAB triblock copolymers. It is observed that to a good degree of

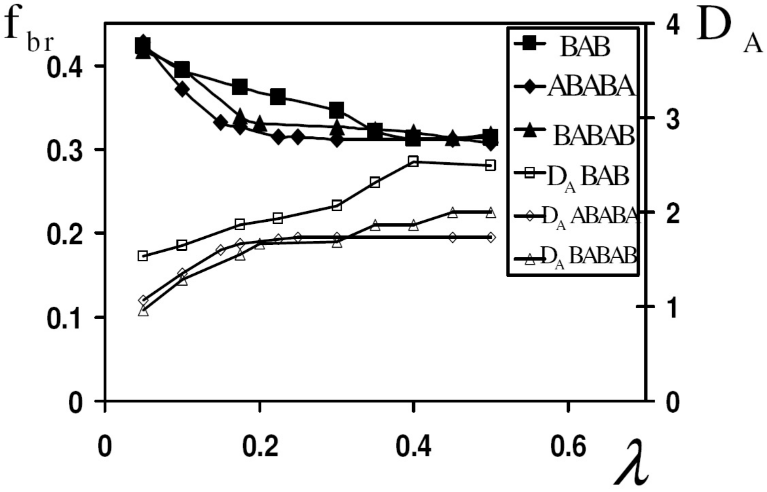

Figure 4.9: Bridging fractions in A domains of ABA, ABABA and BABAB copolymers. The parameters are $\chi N_{penta} = 50$, $\chi N_{tri} = 50$, $\beta = 12$, and $\mu/\chi = 2.5$. Both the sequences of pentablock copolymers are symmetric and posses equal volume fractions of A and B, i.e. $f_1 = f_5 = 0.125$, and $f_2 = f_3 = f_4 = 0.25$. The variation of bridging fraction as a function of rigidity is qualitatively similar for both triblock and pentablock copolymers irrespective of the nature of the sequence.

quantitative agreement, the behavior and the values of the bridging fractions in the pentablock copolymers are very similar to those observed in triblock copolymers. Moreover, as can be observed in the results depicted, the overall behavior of the B and the A bridging again correlate very well with the dependence of the nematic order parameters (refer Fig. 4.8) and of domain spacing (Fig. 4.9) as a function of the rigidity of the B block. The minor quantitative differences observed between the tri- and pentablock copolymers can be rationalized by noting that doubling the chain length of pentablock copolymer and renormalizing the χN parameter does not necessarily translate into same degree of orientational ordering and compositional segregations in the two systems. The latter differences manifest as the quantitative differences in the bridging fractions observed in Fig. 4.8 and Fig. 4.9.

The above results suggest that the pentablock copolymers combine the advantages offered by both ABA and BAB triblock copolymers. Indeed, both A and B domains exhibit bridging and consequently all the layers of the lamella exhibit bridging. Moreover, the bridging fraction of A and B blocks were seen to be correlated to the volume fraction of bridgeable blocks. The latter idea has already been exploited in experiments on BABAB pentablock copolymers where the overall toughness was increased by increasing the center block fraction (f_3) relative to the end blocks [11]. An alternative approach would be to mix a small amount of pentablock copolymers to triblock copolymers to thereby ensure bridging in both A and B domains [53]. Our results suggest that for such a protocol, adding a small amount of ABABA pentablock to a triblock BAB copolymer may be an optimal choice to exploit the substantial bridging present in the crystalline B blocks.

4.5 Conclusions

In this chapter, we have proposed a model to understand the thermodynamics of semicrystalline multiblock copolymers. The crystalline component was treated as a semiflexible chain possessing temperature dependent rigidity. The tendency to form parallel bonds was modeled using a Maier-Saupe potential. The domain scaling as a function of volume fraction of flexible block in a semicrystalline diblock copolymer was found to be in qualitative agreement with previous scaling theories. The bridging fractions was calculated for triblock and pentablock copolymers as a function of the rigidity of the semiflexible chain. It was observed that increasing the rigidity has opposing effects on the amount of bridging in A and B domains. For both triblock and pentablock copolymers, it was observed that increasing the rigidity of semiflexible block led to increase in the bridging conformations in the B domains, whereas it decreases the bridging conformations in the A domains. In a nutshell, our results suggest that if the objective is to enhance the bridging fractions in A domains of either BAB triblock copolymers or ABABA/BABAB pentablock copolymers, then it is a better strategy to use a noncrystallizable B block which offers larger bridging fractions in the A domains. In contrast, if the objective is to increase the bridging fractions in the B domain of ABA triblock or ABABA/BABAB pentablock, then it is more prudent to use crystallizable

B blocks.

We note that we have considered only lamellar morphologies and that some of the parameters considered may not necessarily exhibit lamellar morphologies at equilibrium. However even in such a situation, we still expect that the qualitative features of our results would hold. We also note that the model presented in this chapter can be extended to 2D and 3D simulations to gain understanding of the role of rigidity of one of the components on the morphologies and its corresponding effect on the phase behavior and the mechanical properties of the multiblock copolymers.

Chapter 5

Thin Film Morphologies of Rod-Coil Block Copolymers

5.1 Introduction

Rod-coil block copolymers are polymers where a flexible polymer is covalently linked to a rigid rodlike polymer which has a very high persistence length. Some of the examples of such rigid polymers are helical proteins and semiconducting polymer with rigid π-conjugated backbones. Such rod-coil block copolymers have received a lot of attention due to their potential applications in organic electronics devices like OLEDs and solar cells [2, 7, 46, 122]. Since these block copolymers can self-assemble at lengthscale of $\sim$ 10nm required for exciton diffusion, they are attractive candidates for photovoltaic and organic LED applications [2, 55, 122, 46]. In such applications where an interface is desired between two materials with different electron affinities, the semiconducting and optically active rod block acts as the electron donor, while electron acceptor is introduced into the coil block either by grafting it onto the flexible block or by simply adding nanoparticles [2].

Owing to the rodlike nature of one of the blocks, the self assembly of rod-coil block copolymers is significantly different that of conventional flexible block copolymers [79, 7, 8]. The self-assembly behavior in rod-coil block copolymer involves rich interplay between the microphase separation between two different blocks and liquid crystalline ordering of rodlike units [79, 7, 8]. The anisotropic nature of the the rodlike chains causes them to undergo orientational ordering to form nematic or smectic phases [96]. Unlike coil-coil diblock copolymers which form lamellar, cylindrical, and spherical morphologies depending on the relative volume fraction [5], rod-coil block copolymer exhibit primarily lamellar morphologies due to the strong orientational interactions between the rigid polymeric chains. The rods can be aligned either normal to the lamellar interface (in Smectic A arrangement) or tilted at an angle to the interface (Smectic C arrangement). The arrangement of rod chains in smectic A and smectic C orientation is displayed in Fig. 5.1. The size of the microphase separated domains and the tilting of rods with respect to the lamellar interface is determined by a competition between interfacial tension between dissimilar phases and the stretching free energy of the flexible coil [8]. Some of the unique morphological features observed for rod-coil diblock copolymer that are not seen for flexible block copolymers are zigzag [79], wavy lamellar [79], arrowhead phases [79], stripe, and puck phases [45, 123]. Theoretical studies have also predicted the existence of these phases [8, 124]. Unlike flexible block copolymers where the phase behavior is governed by just two parameters, volume fraction of one of the blocks (f), and the Flory-Huggins interactions parameter (χN), the phase behavior of rod-coil block copolymers is also influenced by the Maier Saupe parameter (μN), and the size asymmetry ratio ν [8, 125, 10, 21]. Maier Saupe potential describes the orientational interactions between anisotropic segments, while the ratio ν is a measure of the packing geometry of the molecules. Phase diagrams based on these four parameters have been constructed both theoretically [8], and experimentally [125]. For utilizing rod-coil block copolymers for organic electronic applications, it is necessary to pattern them onto thin films [126]. Hence it is imperative to the understand the phase behavior of these complex polymers under confinement. Before studying thin films of rod-coil block copolymers, it is pertinent to note what has been observed for thin films of coil-coil flexible diblock copolymers. The self-assembly of confined flexible diblock copolymers is affected by the surface interactions with the individual components and the commensurabil-

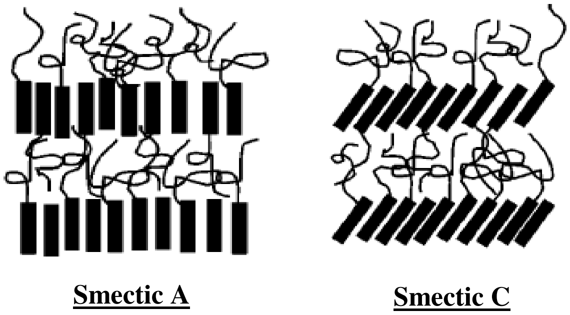

Figure 5.1: Schematic of orientation of rod chains within block copolymer microphases for smectic A and smectic C alignment.

ity of the thickness of the film with respect to bulk domain spacing [16]. If the surface has a preference for one block, it will result in segregation of that particular block near the surface. This can lead to either symmetric parallel morphology where the surfaces prefer the same block or antisymmetric parallel morphology where both the surfaces prefer different blocks. When the thickness is not commensurate with bulk domain spacing, the lamellar domain spacing can change or the orientation of lamellae might flip from parallel to perpendicular orientation [16, 127]. The perpendicular lamellae is stabilized for the case of neutral walls as it can maintain the bulk domain spacing.

The system of confined rod-coil diblock copolymer films is much more complex than the case of flexible diblock copolymers. In addition to surface interactions and thickness constraints, the anisotropic nature of rigid rodlike chain influences the phase behavior. Since the rod chains are not flexible, they cannot deform near the plates which confine them [47]. Also the rods can adopt a different orientation inside the thin film as compared to their bulk counterpart when the thickness is incommensurate with the bulk domain spacing. It is possible to have more than one orientation of rod in a given system of confined rod-coil block copolymers films [47].

Most of the experimental work has been focussed on studying free standing films of rod-coil diblock copolymers [128, 129]. In thin films where rod is attracted to the surface, perpendicular lamellae of rod-coil block copolymer was formed with either monolayer or bilayer smectic stacking [130, 129]. In thin films of poly (alkoxyphenylenevinylene)-*b*-isoprene (PPV-*b*-PI), where

PI has lower surface energy both at the silicon substrate and vacuum interface, parallel lamellae with symmetric wetting is observed generally for smaller thicknesses [128]. When thickness is incommensurate with the domain spacing in bulk, island-hole formation occurs where perpendicular lamellae mediate the change in thickness. It was also observed that on increasing the thickness of the film, the amount of perpendicular lamellae at the vacuum interface increases [128, 131, 132]. This reorientation of lamellae serves to relax the incommensurability in the relatively thick films [128, 47].

Understanding the nature of structure formation and orientation of semiconducting rodlike units in thin films of rod-coil block copolymers is key in order to make them useful for photovoltaic or organic LED applications. Very less theoretical studies are concerned with self-assembly in thin films of rod-coil block copolymers unlike the case for flexible block copolymers [16, 127, 25]. Pereira and Williams performed analytical calculations to model the parallel to perpendicular lamellae transitions in thin films of rod-coil block copolymers [47]. They accounted for possibility of two different orientations of rods in parallel lamellae and compared the free energies of different types of parallel lamellae with perpendicular lamellar morphology. However they did not account for possibility of different orientation of rods in perpendicular lamellae than in bulk. Also the framework does not allow to account for non-lamellar morphologies. A model previously developed in our group based on self-consistent field theory (SCFT) [16, 17, 18] has been utilized to understand the self assembly of rod-coil block copolymers in bulk [8]. The model was successful in rationalizing the experimental observations for both lamellar-like and non-lamellar like morphologies. Furthermore, it does not require any prior assumption of the nature of morphology and can predict the formation of any complicated microstructure unlike the analytical method proposed before [47]. In this chapter, we extend the model to study the effect of surface interactions and geometric constraints on self-assembly in thin films of rod-coil block copolymers. We analyze how these effects modify the domain spacing and orientation of rods from their bulk values. We also explore how the nature of surface interactions and boundary (surface) conditions within the framework of SCFT govern the transition between parallel and perpendicular lamellae. In Sec. II we briefly describe our model to analyze the structure formation in thin films of such polymers. Sec. III focusses on our simulation results to characterize phase behavior of rod-coil block copolymer thin films.

5.2 SCFT Model

5.2.1 Key Ingredients

The statistical mechanics of rod-coil block copolymers under self-consistent field theory framework has been treated extensively in the article by Pryamitsyn and Ganesan [8]. Also, the previous work on self-assembly of side-chain liquid crystalline polymers (Chapter. 3) and semicrystalline block copolymers (Chapter. 4) have similar ingredients. So we will present only the key details which differentiate this model and focus on boundary conditions while referring to previous articles [8, 10] for more detailed formalism. Notations are quite similar to the one adopted in the chapter on side chain liquid crystalline block copolymers (Refer Chapter. 3) and the previous article on rod-coil block copolymers [8].

We consider an incompressible melt of n rod-coil block copolymers chains confined by two plates separated by a distance, Δ. The volume fraction of the coil is given by f. The statistical segment of rod, a, is defined such that it possesses the same monomeric volume as the coil polymer, $ad^2 = b = \rho^{-1}$, where d is the diameter of rod molecule and b is statistical segment of coil molecule. All the lengthscales are normalized by coil radius of gyration, $R_g^2 = Nb^2/6$. In these units the length of the rod block is $L_R = (1-f)\beta$, where $\beta = Na/R_g$. The conformations of the flexible coil are ascribed by a Gaussian stretching energy. The microphase separation between the rod and coil block is governed by the product of Flory-Huggins interaction parameter and degree of polymerization, χN. To quantify the degree of orientational ordering, we utilize Maier-Saupe potential where the strength of orientational interactions is measured by the Maier-Saupe parameter, ω [8, 10, 96].

5.2.2 Treatment of Surface Potential and Boundary Conditions

In the SCFT framework, the incompressibility constraint is imposed by assuming that the total polymer volume fraction equals 1 in the entire system [16, 133]. However in case of confinement by hard surfaces the polymer density goes to zero near the surfaces. The inconsistency between these conditions is alleviated by modifying the incompressibility constraint. For the particular case of rod-coil block copolymers, we utilize $\phi_C(\mathbf{r}) + \phi_R(\mathbf{r}) = \phi_0(\mathbf{r})$ and choose

$$\phi_0(\mathbf{r}) = \begin{cases} (1 - \cos(\pi y/\epsilon))/2, & \text{if } 0 \leq y \leq \epsilon \\ 1, & \text{if } \epsilon \leq y \leq \Delta - \epsilon \\ (1 - \cos(\pi(\Delta - y)/\epsilon))/2, & \text{if } \Delta - \epsilon \leq x \leq \Delta \end{cases} \tag{5.1}$$

The distance ϵ from the surface over which the total polymer density rises to 1 is selected to be smaller than the radius of gyration of coil block (R_g) or the length of rod block ($(1-f)Na$). The surface potential ($H(\mathbf{r})$) acts over a distance δ from the surface and acts on the difference in densities of coil and rod polymers, $\phi_C(\mathbf{r}) - \phi_R(\mathbf{r})$ [16].

$$H(\mathbf{r}) = \begin{cases} \lambda_1(1 + \cos(\pi y/\delta))/\delta, & \text{if } 0 \leq y \leq \delta \\ 0, & \text{if } \epsilon \leq y \leq \Delta - \delta \\ \lambda_2(1 + \cos(\pi(\Delta - y)/\delta))/\delta, & \text{if } \Delta - \delta \leq x \leq \Delta \end{cases} \tag{5.2}$$

δ measures the range of surface potential, and λ_1 and λ_2 measure the strength of surface potential at the two surfaces. In its present form, a negative value of λ_1 or λ_2 imply that surface has preferential interaction for the coil block. To model the influence of the substrate boundary upon the flexible polymer conformations, Dirichlet boundary condition is applied for the end-segment distribution function of the coil block [27, 26]. Also, those conformations of rod molecules which result in any part of rod chain going out of confinement are disregarded. For the purposes of this chapter, we refer to this treatment of surface as “zero density” boundary condition.

5.3 Results and Discussion

5.3.1 Confinement by Neutral Surfaces

The first effect we study is the effect of confining rod-coil block copolymers by hard surfaces. The surface interactions are switched off ($\lambda_1 = \lambda_2 = 0$). In this study, we consider different morphologies exhibited in bulk (Smectic A, Smectic C, Puck Phases) under confinement and compare how are the morphological features different in thin films compared to bulk. For the case of lamellar morphologies we utilize free energy analysis to find which orientation (parallel or perpendicular) is the stable morphology [16, 27, 134].

Smectic A - As a first illustration, we consider a case which exhibits smectic A morphology in bulk. The bulk domain spacing is 6 R_g. In Fig. 5.2(a), we plot the free energy vs thickness for the two different types of lamellar orientation - parallel and perpendicular. Both these morphologies were achieved by starting with appropriate initial conditions for the potentials conjugate to the densities of individual component and the tensor potential conjugate to the orientational order parameter [18, 8]. The quantity plotted on y-axis is free energy of the thin film modified by the bulk free energy, and this quantity accounts for the excess free energy per unit area [16]. The parallel morphology shows periodic

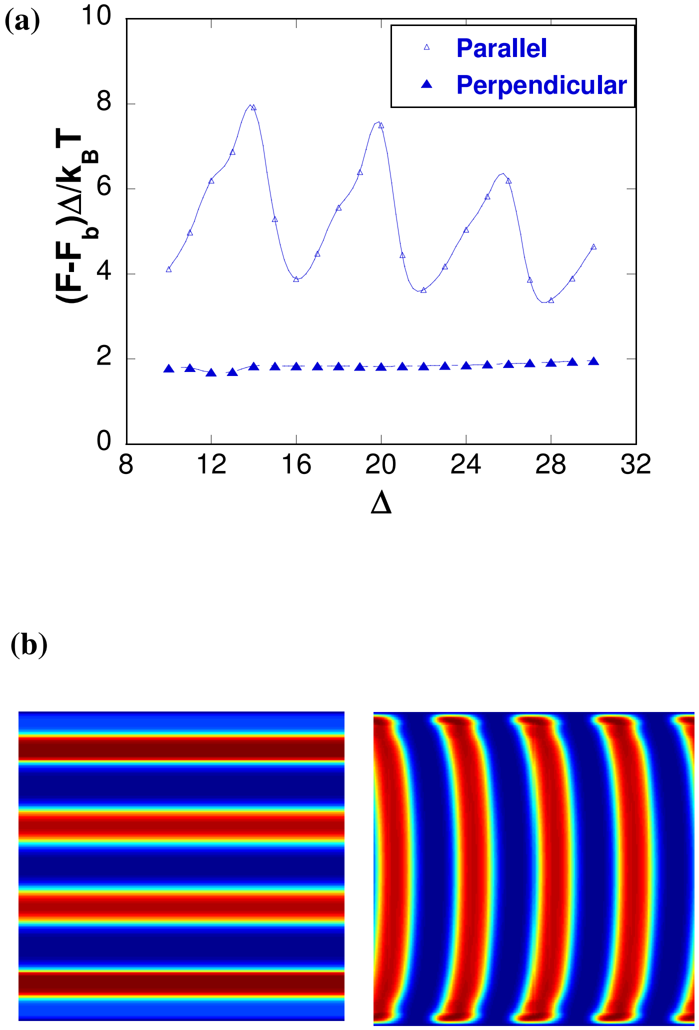

Figure 5.2: (a) Free energy plot for parallel and perpendicular lamellae for a smectic A case in bulk. The perpendicular lamellae posses lower free energy over the entire range of thickness. The parameters are : $\chi N = 10$, $f = 0.4$, $\omega N = 30$, and $\beta = 6$. (b) Density profile of the coil phase for $\Delta = 22R_g$. Red : Coil Block, Blue: Rod Block.

oscillations (periodic minima and maxima) in the free energy vs thickness curve, while the free energy of perpendicular orientation of lamellae is fairly constant throughout the range of thickness. For the entire range of thicknesses studied, the perpendicular lamellar orientation is stabilized in comparison to parallel lamellae morphology. For all the cases of Smectic A studied under confinement where length of rod was larger than radius of gyration of coil block, we observed that for neutral surface the *perpendicular* lamellar morphology always had the lower free energy.

In Fig. 5.2(b), we display the density profiles for parallel and perpendicular orientation for a representative thickness. For the case of perpendicular morphology, the domain width is same as bulk domain spacing (6 R_g) for all thicknesses and the smectic A orientation is maintained. At the thicknesses corresponding to minima in the free energy plot for parallel lamellar morphology, the domain spacing in center of the film is same as bulk domain spacing. We can see that the minima in free energy plot for parallel orientation of lamellae are separated by the bulk domain spacing. In the case of perpendicular morphology, the rods are aligned parallel to the confining surfaces. In Fig. 5.2(b) for the parallel lamellar morphology, we observe that the layers near both the surfaces are that of a rod block for neutral surfaces. Also, the orientation of rods in this layer was found to be arranged parallel to the substrate. Thus in parallel lamellae, two different orientations of rods with respect to the lamellar normal were observed within a same film – parallel to surface near the boundaries and perpendicular to surface (and lamellar interface) in the rest of the film.

The reason for lower free energy of perpendicular lamellae arises due to the surface stabilization of the rods and the ability to maintain the same smectic A orientation and domain spacing as in bulk. Because of the boundary conditions imposed on rods, even slight tilting of rods with respect to the substrate is severely prohibited. Thus rods prefer to arrange themselves parallel to the surface. In parallel lamellae, the domain spacing and orientation of rods with respect to the lamellar interface is only maintained in layers away from the substrate, whereas for the layer closest to surface, rods are aligned parallel to the lamellar interface. Such surface induced perpendicular morphologies where rods are stacked parallel to surface have been observed experimentally [129]. We also observe that in the case of perpendicular lamellae, the lamellaes are slightly curved near the surfaces. It is believed that the near the surfaces, rod molecules shift with respect to one another to allow for flexible chains to gain entropy and therefore lower their confinement energy [135]. This curved profile near the surface diminishes with stronger orientational ordering, i.e with perfect alignment of rods, the perpendicular lamellae are much straighter.

Smectic C At higher coil fractions and for longer rods in bulk, smectic A - smectic C transition occurs. Within the lamellar morphology, rods are tilted at an angle with respect to the normal to the lamellar interface for smectic C orientation [8, 96]. Even though the interfacial area increases between the rod and coil blocks, the overall free energy is lowered due to the extra conformational entropy gained by the coil block [8]. In Fig. 5.3, we plot the free

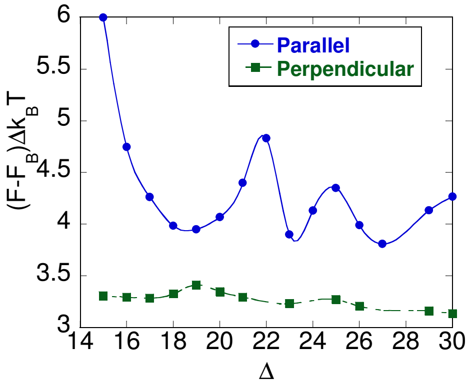

Figure 5.3: $\chi N = 8.0$, $f = 0.5$, $\beta = 10.$, $\omega N = 32$. Like for Smectic A morphology, perpendicular lamellar orientation is preferred for smectic C cases too.

energy vs thickness plot for parallel and perpendicular lamellae for a set of parameters which exhibits the smectic C morphology in bulk. The orientation of rods with respect to lamellar normal in the case of bulk is $50\,^\circ$. We again observe periodic minima and maxima in the free energy curve as a function of the thickness of the film for the case of parallel lamellae. Also, at the minima in free energy plot (Δ = 19, 23, and 27 R_g), the orientation of rods with respect to lamellar interface in the center of the film is same as in bulk. Near the surface, the rods are aligned parallel to the surface like the situation exhibited in Fig. 5.2 (b). Thus two different types of orientations are exhibited for parallel lamellar orientation in confined thin films for both smectic A and smectic C orientation of rods. However, from Fig. 5.3 we can observe that for every thickness considered, the perpendicular lamellae has lower free energy

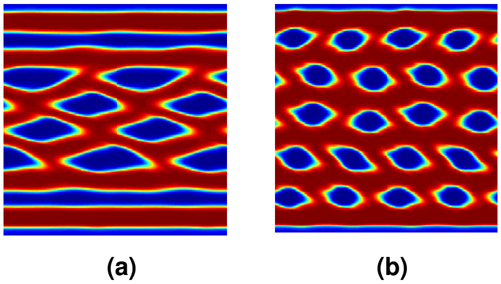

Figure 5.4: Representative density profiles for confined puck phase (a) $\chi N = 12$, $f = 0.6$, $\beta = 10.$, $\omega N = 48$ and (b) $\chi N = 16$, $f = 0.7$, $\beta = 10$, $\omega N = 64$.

compared to the parallel lamellar orientation. In the case of perpendicular lamellae, rods are aligned parallel near the surface. In the center of the film, perpendicular channels are formed where rods are oriented at an angle to the lamellar interface. Thus, we observe that due to surface stabilization of rods and ability to maintain the same domain spacing and orientation in perpendicular lamellae compared to bulk, confinement by neutral surface always leads to formation of perpendicular lamellar under our SCFT formalism. Before presenting the results of surface preference on self-assembly, we discuss the effect of confinement on puck phases which are observed at very high coil volume fractions.

Broken Lamellae and Puck Phases In Fig. 5.4, we show the effect of confinement on rod-coil block copolymers self-assembly at very high coil volume fractions. At higher coil volume fractions ($f \geq 0.6$), these rod-coil block copolymers exhibit broken lamellae or puck phase morphology [8]. We observe that similar phases are exhibited under confinement for the same range of parameters where they exhibit puck phases in bulk. However for the case of lower volume fraction ($f = 0.6$) in Fig. 5.4, we observe that presence of surface induces lamellar orientation near the surface, while having puck nanodomains of rods throughout the film. But at higher volume fractions of coil ($f = 0.7$) in the same figure, we observe that puck phases appear throughout the film as expected. Such phases have been observed experimentally too [136], where rectangular rod domains are packed onto a hexagonal lattice at higher volume fractions of the coil block. Even though such phases incur a huge penalty due to large interfacial area between coils and rods, it allows for coils to increase its stretching entropy [8].

In the next subsection, we study the effect of introducing surface preference for one component (coil) in order to study the perpendicular to parallel lamellar transition in confined thin films of rod-coil block copolymer.

5.3.2 Effect of Coil Attractive Surfaces

We have observed that perpendicular lamellar orientation are naturally favored over parallel lamellar orientation for the case of neutral surfaces. We also noted that rods formed formed a layer near the surface even though surface had no preference for either component. Therefore to study the parallel-perpendicular transition, it is natural to introduce a surface preference for the coil block, which would favor formation of parallel lamellae with coils at the

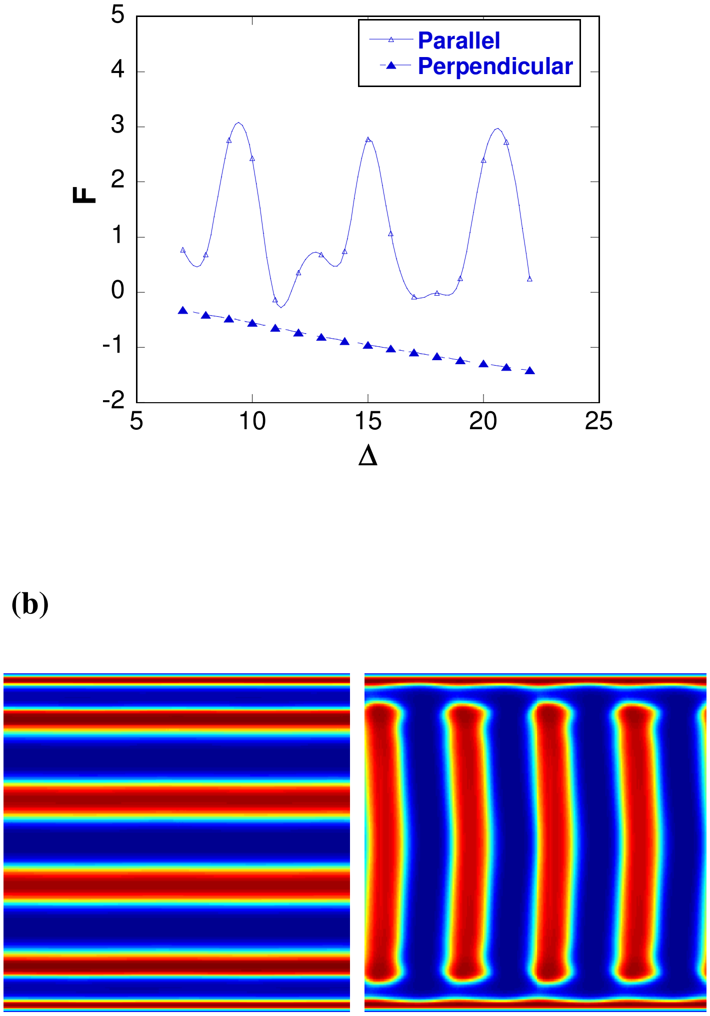

Figure 5.5: (a) Free energy versus thickness plot for parallel and perpendicular lamellae for the case considered in Fig. 5.2. $\lambda_1 = \lambda_2 = -20$. Perpendicular free energy has lower free energy even upon introduction of attractive interactions for coil. (b) Representative density profiles of parallel and perpendicular lamellae.

surface. We introduce this feature by rendering the surface parameters (λ_1 and λ_2) non-zero. In Fig. 5.5(a), we show the effect of coil attractive surface via a free energy vs. thickness plot for both parallel and perpendicular lamellae. Surprisingly, perpendicular lamellae is still favored over parallel lamellae even though there is a surface preference for coil block. We observed the same behavior for a range of surface parameters (λ_1, λ_2 = -10 to -40). If we look at representative density profiles in Fig. 5.5(b), we observe formation of coil block layers near the two confining surfaces in both the parallel and perpendicular lamellar orientation. Also, like in the case of neutral surfaces, rods closest to the surface were aligned parallel to the surface for both parallel and perpendicular lamellae. This surface induced orientation of rods plays a significant role in deciding the final morphology of rod-coil block copolymers within our theoretical framework. Only way to obtain a smectic A orientation of rods in proximity to the surface, is to forcefully exclude rods from the surface by having a very high value of surface range parameter, δ. If the range of surface potential is of the same order as length of the rod, then the effect of surface on orientation of rods would greatly diminish. But this would require us to have unrealistic values for δ. In next subsection, we look at modifying the boundary conditions in order to study parallel - perpendicular lamellae transition in confined films of rod-coil block copolymer.

5.3.3 No Flux Boundary Condition

To alleviate the issues with "zero density" boundary condition, we attempt to model the parallel-perpendicular transition under SCFT framework with Neumann condition or no flux boundary condition for Gaussian coil chain propagator [17, 26]. At the surfaces ($y = 0$ and $y = \Delta$),

$$\underline{\mathbf{n}} \cdot \nabla q = 0 \tag{5.3}$$

This acts as adsorption boundary condition for coil, thus favoring the formation of coil layers at the surface [17]. The general form of the Eq. (5.3) for weakly attractive walls is $\underline{\mathbf{n}} \cdot \nabla q + \kappa q = 0$, where κ^{-1} represents the lengthscale of attractive interactions [17]. Eq. (5.3) is a special case which leads to formation of coils at the surface The treatment of rods near the surface is same as detailed in previous section. We apply the boundary condition to same set of parameters studied in Fig. 5.2 and Fig. 5.5. We plot the variation of normalized free energy as a function of thickness in Fig. 5.6 for both parallel and perpendicular lamellae. We again observe that perpendicular lamellar morphology is the favored phase and posses lower free energy than parallel lamellae morphology. Even though the Neumann boundary condition results in formation of coil layers near the two surface, the surface induced orientation of rods results in parallel alignment of rods with respect to the surface in the rod layer in closest proximity to the surface. The lengthscale of the coil layer near the surface due to application of Neumann boundary condition is to the order of radius of gyration of coil block, R_g. However, if the rod length is larger than R_g, the coil layer would not be able to screen out the effect of surface on the alignment of rods. Only when the two lengths are comparable ($L_R = (1-f)\beta \sim R_g$), we can expect that coil layer will screen out the effect of surface on rods and the smectic alignment of rods with respect to lamellar interface in proximity to the surface will be maintained within the confined thin films.

Short Rods In Fig. 5.8, we plot the free energy vs thickness plot for the case of very short rods, i.e $L_R \sim R_g$. We observe that parallel lamellae is stabilized for the case of very short rods and it has lower free energy than the perpendicular lamellae morphology. The smectic A orientation is maintained in parallel lamellae near the surface and is unaffected by the presence of confining surface. As $(1-f)\beta \sim R_g$, the coil layer near the surface is able to screen out any effect of surface induced alignment of the rods. Also the no-flux boundary condition at the surface causes coil to form the layer near the surface which favors parallel lamellae. Thus one avenue to effect a transition from perpendicular to parallel transition is to make surface attractive for coil and have relatively shorter rods.

To account for effect of orientational ordering on stability of perpendicular vs parallel lamellae, we consider the effect of Maier-Saupe parameter on ordering in thin films of rod-coil block copolymer. In Fig. 5.8, we plot the free energy vs. thickness curves for two different values of ωN. For the lower value of ωN, we observe that parallel lamellae is the favored phases. On undergoing isotropic-nematic transition, perpendicular lamellar is favored over

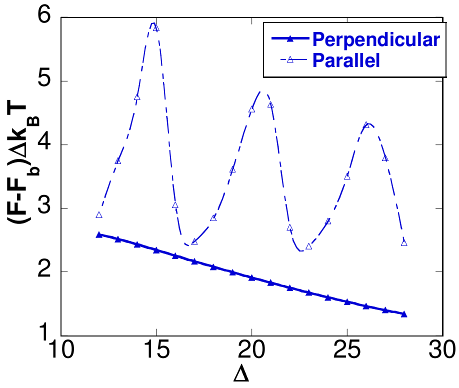

Figure 5.6: Plot of free energy as a function of thickness for parameters studied in Fig. 5.2. Here we apply Neumann condition for coil chain propagator function. In this framework, the perpendicular lamellae has the lowest free energy.

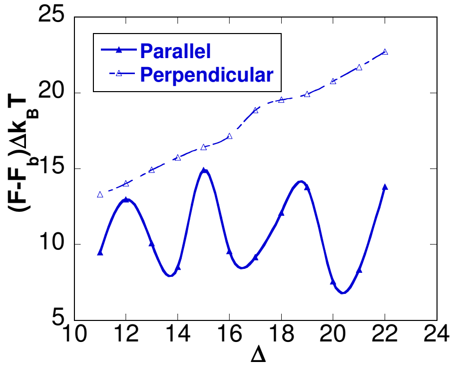

Figure 5.7: Free energy vs thickness variation for parallel and perpendicular lamellae for the case of very short rods. $\chi N = 12$, $f = 0.4$, $\omega N = 96$, and $\beta = 2$. The length of rods is comparable to coil layer near the surface, and thus the smectic A orientation is preserved near the surfaces under confinement.

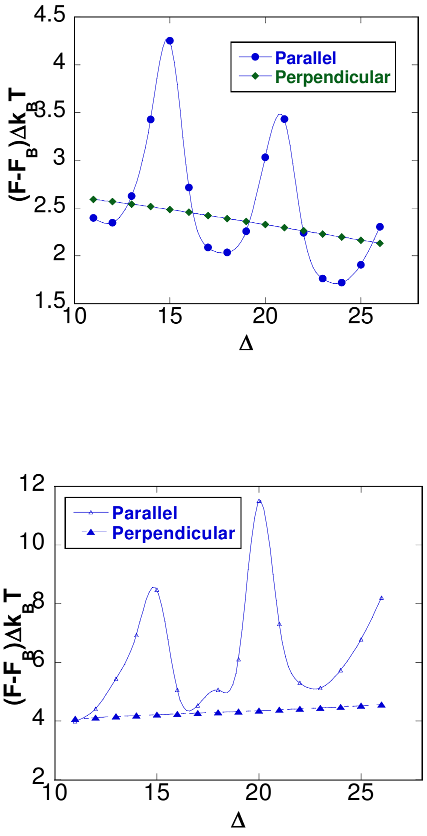

Figure 5.8: (a) $\omega N = 18$. This case is near isotropic-nematic transition. (b) $\omega N = 30$. This case is for higher orientational ordering in the rod block. Smectic ordering inside the rod phase tends to favor the perpendicular lamellar orientation.

parallel morphology. Smectic ordering stabilizes perpendicular lamellae. Due to strong orientational ordering in rod phase, the perpendicular lamellae are much straighter and hence stable.

5.4 Summary

In this chapter, we presented the mean field theory method to study the self-assembly of rod-coil block copolymers under confinement. We utilize a free energy analysis to study the stability of perpendicular and parallel lamellae. We observe that perpendicular lamellae is stabilized for lamellar-like morphologies for neutral surfaces. The surface induced orientation of rods leads to preference for perpendicular lamellae. Only for shorter rods and with surface preference for coil, parallel lamellar orientation was found to have lower free energy. In this chapter, we also looked at the effects of different boundary conditions in the framework of SCFT on the phase behavior of rod-coil block copolymers. We found out that utilizing no flux boundary condition allows us to study the transition between parallel and perpendicular lamellae.

In the next chapter, we utilize the morphologies generated under this framework and apply photovoltaic modeling to understand the microstructure-property link in order to optimize the performance of polymer-based solar cells.

Chapter 6

Morphology Property Correlations of Rod-Coil Block Copolymers for Photovoltaic Applications

6.1 Introduction

Photovoltaics and solar cells are emerging as attractive candidates for tapping into sources of renewable energy. Conventional solar cells based on crystalline silicon are quite efficient, but are accompanied by the disadvantage of being expensive to fabricate [55, 56]. Recently, polymeric and organic solar cells have emerged as attractive alternatives which are relatively inexpensive and allow fabrication onto flexible substrates using high throughput solution processing techniques [55, 56]. However, currently, the best available polymer solar cells still lag behind that of conventional silicon devices in their efficiencies, and hence there is a need to understand the relationship between microstructure of such polymeric devices and their final properties to facilitate the design of efficient polymer photovoltaic devices.

There are many key issues regarding in the design of polymeric photovoltaic (PV) devices which need to be addressed. We note that the mechanism of photovoltaic operation in polymer solar cells is quite different compared to conventional solar cells. Conjugate (or semiconducting) polymers are electronically active because of their highly polarizable π-electrons [56]. However, in contrast to silicon devices, on photon absorption, free charge carriers (electrons or holes) are not generated in these conjugate polymers [137, 55, 56]. Rather, electron-hole pairs known as *excitons* are generated. These pairs are bound together by a high Coulombic binding energy (relative to inorganic materials) of the order of $0.1 - 1.4$ eV [56]. Such excitons can dissociate into electron and hole pairs at an interface between two materials having different electron affinities, thereby necessitating at least two chemical components in the fabrication of polymeric electronic devices [55, 138]. The material with higher electron affinity is conventionally termed the acceptor (A), while the material with lower electron affinity is called the donor (D). The transport of the electrons and holes to the respective electrodes constitutes useful power generated from the system. This transport process competes with a possibility for the electron-hole pairs to recombine, as well as the decay of the original exciton after diffusion over a decay length [55, 56]. It is evident then that an optimal lengthscale of phase separation between the two components are required to balance the preceding transport processes in order to obtain high photocurrents [139, 140]. Not surprisingly, understanding and controlling the distribution of the donor-acceptor interface within the device is an actively pursued strategy to improve the efficiency of the PV device.

From the above discussion it is evident that the simplest device structures one might envision viz., a bilayer device (or planar heterojunction) of a layer of donor and acceptor materials sandwiched between two electrodes, is not expected to be very efficient as PV device [141, 61, 138]. Indeed, due to the decay process mentioned above, only excitons generated within a layer of ~ 10 nm from the D-A interface can contribute to generation of charge carriers. Hence the active layer region in such bilayer devices is small compared to the typical device thickness (which is of the order of 100-500 nm) [55, 142, 58]. Consequently, most organic PV efforts focus on bulk heterojunction devices (BHJ) where interfaces between donor and acceptor material are distributed throughout the device [55]. In such a case, achieving donor and acceptor domains with a lengthscale of ~ 10 nm would ensure that almost all photogenerated excitons diffuse to interface and dissociate to form free charge carriers (electrons and holes). This reasoning has motivated researchers to exploit thermodynamic phase separation of two chemically incompatible components has a potential route to achieve BHJ devices. The most common materials that have been studied in this context are blends of conjugated polymer such as poly(phenylenevinylene) (PPV) or poly(3-hexylthiophene) (P3HT) acting as donors mixed with either fullerene derivatives like (6,6)-phenyl C61-butyric acid methyl ester (PCBM) or inorganic materials like CdSe or titania acting as electron acceptors [143, 57, 144, 145, 146]. In these materials, efficiencies in the range $4-5\%$ have been demonstrated — rendering them competitive with silicon solar cells [55, 57].

A potential issue with using donor-acceptor blends for the above applications is that the intermixing between the two components leads to *macrophase* separation. In such a case, the domain sizes are larger and due to kinetic effects may form “dead ends” and bottlenecks which prevent the transfer of charges to appropriate electrodes. Consequently, it is harder to exercise complete control over the resulting morphologies and domain sizes. Not surprisingly, a number of physical parameters which modulate the kinetics of the phase separation processes, such as the choice of casting solvent, has been shown to play an important role on the efficiency of the resulting device [57]. Consequently, there is a need for ordered heterojunctions where the lengthscale for phase separation is controllable and smaller, and in which continuous pathways exist for the charge carriers to reach the appropriate electrodes [58, 55].

Recently, semiconducting *block copolymers* have emerged as a promising alternative which can avoid the shortcomings noted in the context of blends [2, 58, 59, 60, 147, 148]. Most such block copolymers consist of a conjugated polymer (donor) which is typically rod-like in conformation linked to a flexible coil block. The flexible block is usually functionalized by electron accepting moieties such as fullerene (C_{60}) or oxadiazole molecules [2, 46]. Due to the chemical incompatibility between the two blocks, the block copolymers *microphase* separate into *equilibrium* ordered heterojunction structures which can potentially alleviate the kinetic issues noted in blends. Indeed, experiments have shown that the donor-acceptor block copolymer may actually exhibit enhanced photovoltaic efficiency relative to a blend of its individual polymers

[2, 59].

Success in the above efforts require a fundamental understanding of the self-assembly morphologies in rod-coil block copolymers (under confinement mimicking devices) and the correlations between the structure and the device properties. The morphological aspects of self-assembly of rod-coil block copolymers has been studied extensively in a number of theoretical [8, 149, 150] and experimental researches [79, 45, 7]. In our earlier work, we developed a self-consistent field theory (SCFT) model for predicting the self-assembly morphologies of rod-coil block copolymers [8]. We delineated a morphological phase diagram within the context of two-dimensional phases which included Smectic A and Smectic C lamellar phases and hockey puck-like cylindrical phases. Subsequent experiments of Segalman and coworkers have examined the phase diagram of rod-coil block copolymers systematically and have confirmed many of the predictions of the theory. More recently, we have extended the preceding framework to address the effect of confinement on the self-assembly morphologies. In the latter work, we confirmed the existence of equilibrium self-assembly morphologies similar to bulk systems, with an additional possibility of the lamella phases being oriented either parallel or perpendicular to the confining surfaces depending on the interaction of the different blocks with the surfaces.

In this article, we seek to extend our above researches on *morphology* predictions to address the *property* characteristics of PV devices consisting of rod-coil block copolymers. For this purpose, we adapt a continuum formalism termed the drift-diffusion model which characterizes the transport of excitons, electrons and holes under photo-adsorption to render predictions regarding the device characteristics. Such drift-diffusion models have been utilized in earlier researches to study the photovoltaic properties of bilayer devices [61] and bulk heterojunctions [62]. Most pertinent to this work, in a seminal work, Buxton and Clarke used such a framework to study the device characteristics of thin film morphologies of *flexible* block copolymers [58].

In this work, we extend the above works by focusing on following aspects:

(i) Incorporating features inherent to the *semi-rigid or rod-like* nature of most of the donor molecules used in the experimental studies: Specifically, the nature of charge transport in such semi-rigid conjugated polymers is expected to be anisotropic [55, 151]. Indeed, experimental evidence exists to show that the transfer of electronic excitation energy is predominantly intrachain (along the length of polymer backbone) as compared to interchain (hopping between different polymers) in extended conformations of conjugated polymers [152, 153]. It has been also been observed that an increase in crystallinity (concomitant with an increase in the orientational ordering of the chains) of conjugated polymer P3HT chains leads to increase in photocurrent [154, 155]. Another set of experimental studies have shown that the hole mobility is enhanced when polymer is infiltrated into titania nanopores due to alignment of polymer chains in the charge transport direction [151]. In the context of thin film field-effect transistors, Siringhaus et al. observed that mobility of charge carriers can vary by a factor of 100 depending on the nature of orientation of P3HT crystalline lamellae inside the film [156]. Also, Kinder et al. observed that intrachain hole mobility along polymer backbone was higher by a factor of 6.5 than the perpendicular direction in thin film transistors [157]. Quantum mechanical calculations have confirmed that while the charge transport in the interchain direction due to π-π stacking of crystalline chains (of P3HT) can contribute to charge transport, that this contribution is less dominant than the one in the intrachain direction (along polymer backbone) [158].

Motivated by the above results, *we extend the drift-diffusion models to account for the possible anisotropy in mobility of holes and excitons.* In the formalism we adopt, we model this effect by rendering the mobility of holes and excitons to be tensors whose values are determined by the average orientational order parameter of the rodlike donor molecules. In this article we demonstrate that the anisotropy effect can have dramatic consequences in determining the PV device characteristics. We should note that our model is not restricted to block copolymers, and in general accommodates the characteristics of BHJ devices with a continuous spatial variation of the morphologies and orientations of donor and acceptors and wherein the donor phases are assumed to be characterized by anisotropic hole and exciton mobilities. In fact, we consider several "simulated" morphologies to understand the physics underlying the results for rod-coil block copolymers. We present the model details and the relevant parameters in Section 6.2.1

(ii) In Section 6.3, we use morphologies generated from a SCFT model of rod-coil block copolymers under confinement to study their device characteristics. While a description of SCFT model and a discussion of the morphological phase diagram are presented in the previous chapter, the results in this section demonstrate that the device characteristics of realistic systems employing donor-acceptor materials of rod-coil block copolymers involve a complex interplay of the several features including the orientation of domains, domain widths, the degree of phase separation, and the orientation of rodlike domain molecules in influencing the PV characteristics of the device. We utilize "artificially generated" morphologies with characteristics similar to those observed in block copolymers to understand the effect of each individual factor listed above and rationalize the results obtained for device modeling of confined thin films of rod-coil block copolymer.

6.2 Drift-Diffusion Modeling of Device Characteristics

6.2.1 Model

In this section, we present the formalism we use to study the device characteristics of photovoltaic cells. The model we employ falls in the general category of drift-diffusion models, which captures within a continuum reaction-diffusion framework the generation of excitons, their dissociation into electrons and holes, and the subsequent transport of electrons and holes to the electrodes. Drift diffusion models yield the spatial variation of electric field and densities of electrons, holes and excitons [159, 137]. Below, we present our adaptation of such a formalism to incorporate: (i) The anisotropic mobility of charge carriers; and (ii) The morphologies resulting from SCFT calculations. Subsequently, we discuss the numerical methods used to solve the resulting equations.

The drift-diffusion equations consists of the following equations governing the exciton (x), electron (n), hole (p) concentrations and the electrostatic potential (ψ): [159, 58, 137]

$$\frac{\partial x}{\partial t} = \frac{1}{q}\nabla \cdot [k_B T \boldsymbol{\mu}_x \cdot \nabla x] + G(\mathbf{r}) - R_d(x) - D(\mathbf{E}, x) + \frac{1}{4}R(n,p) \quad (6.1)$$

$$\frac{\partial n}{\partial t} = \frac{1}{q}\nabla \cdot \mathbf{J}_n, + D(\mathbf{E}, x) - R(n,p) \quad (6.2)$$

$$\frac{\partial p}{\partial t} = -\frac{1}{q}\nabla \cdot \mathbf{J}_p + D(\mathbf{E}, x) - R(n,p), \quad (6.3)$$

$$\nabla.(\epsilon \nabla \psi) = -q(p - n). \quad (6.4)$$

Equations 6.1 - 6.3 represent continuity equations for exciton, electron and hole concentrations. Eq. 6.4 represents the Poisson's equation relating the electrostatic potential (ψ) to the local difference in concentrations of electrons (n) and holes (p). Here, ϵ is the permittivity of the medium, and q denotes the elementary charge.

In Eq. 6.1 first term represents the transport due to diffusion of excitons with the mobility coefficient denoted as $\boldsymbol{\mu}_x$. The terms $R_d(x)$, $G(\mathbf{r})$ and $D(\mathbf{E}, x)$ represent respectively the rates of decay, photogeneration and dissociation of excitons. The functional forms for these rates are assumed to be similar to those adopted in earlier works [58, 137, 61]. To maintain completeness, we present a brief compendium of the relevant equations below. The decay rate of excitons $R_d(x)$ is assumed to be of the form, $R_d(x) = x/\tau_x$, where τ_x is the average lifetime of exciton chosen such that the diffusion length of exciton is 10 nm. The term $G(\mathbf{r})$ is assumed to be of the form:

$$G(\mathbf{r}) = \Sigma_i \Phi_i(\nu_i)\alpha_i \exp\left[-\alpha_i(\Delta - y)\right], \tag{6.5}$$

Here $\Phi_i(\nu_i)$ represents the frequency (ν_i) dependent incident photon flux [160]. The incident power is obtained by summing over the intensities at different frequencies. This data corresponds to AM 1.5 Solar Insolation data having a total irradiance of 83.18 mW cm^{-2}. The frequency dependent absorption coefficient (α_i) is assumed to have a Gaussian distribution as a function of the frequency, ν_i [137, 58]. The photogeneration of excitons have been assumed to have an exponential dependence on the distance from the transparent top electrode, $(\Delta - y)$ [137, 58].

The dissociation of excitons $D(\mathbf{E}, x)$ is modeled through Onsager's theory of electrolyte dissociation: [161]

$$D(\mathbf{E}, x) = xN_f \int_0^\infty k_D(\mathbf{E}, a)F(a)da, \tag{6.6}$$

where k_D is the electric field dependent rate constant given by Braun: [162]

$$k_D(\mathbf{E}, a) = K_R \frac{3}{4\pi a^3} \exp(-E_{b0}/k_BT)\left[1 + b + \frac{b^2}{3} + \frac{b^3}{18} + \frac{b^4}{180} + ...\right] \tag{6.7}$$

where,

$$K_R = q\mu_{avg}/\epsilon \tag{6.8}$$

$$b = q^3|\mathbf{E}|/8\pi\epsilon k_B^2 T^2 \tag{6.9}$$

where μ_{avg} is the averaged mobilities of electrons and holes at that point in space. The dissociation rate is integrated over a Gaussian distribution of separation distances (a), specified by $F(a)$. The exciton binding energy is denoted as E_{b0}.

The term $R(n,p)$ reprsents the recombination rate of electrons and holes which is assumed to bimolecular reaction described by a Langevin recombination term. Only a fraction (1/4) of electrons and holes are assumed to recombine to form singlet excitons [163].

$$R(n,p) = q(\mu_n + \mu_p)pn/\epsilon \tag{6.10}$$

where μ_n and μ_p represent the isotropic mobilities of electron and holes respectively.

In Eqs. (6.2) and Eq. (6.3), the first term represents the flux (current density) of the charge carriers which are assumed to be of the form:

$$\mathbf{J}_n = -qn\boldsymbol{\mu}_n \cdot \nabla\psi + k_B T\boldsymbol{\mu}_n \cdot \nabla n, \tag{6.11}$$

$$\mathbf{J}_p = -qp\boldsymbol{\mu}_p \cdot \nabla\psi - k_B T\boldsymbol{\mu}_p \cdot \nabla p. \tag{6.12}$$

In the above, the mobilities of electrons and holes are denoted by $\boldsymbol{\mu}_n$ and $\boldsymbol{\mu}_p$ respectively. The above fluxes can be seen to consist of two contributions: a diffusive flux arising from the concentration gradient and a drift term arising from the influence of electric field (Since exciton is neutral, Eq. (6.1) does not have a drift term). Prior researches which have used the above formalism have assumed that the (electric-field dependent) mobilities $\boldsymbol{\mu}_i (i = n, p)$ are isotropic and are given by Poole-Frenkel form:

$$\mu_i = \mu_i^0 \exp(\gamma \sqrt{|\mathbf{E}|}) \tag{6.13}$$

where μ_i^0 is the zero field mobility and the field-dependent mobility parameter is represented by γ.

To adapt the above formalism to the systems of interest in this article, a few modifications are needed. On the one hand, the above equations need to be recast in a form which accounts for the input spatial morphologies of the donor acceptor system. The morphologies are characterized by the fields which denote the volume fraction profiles of the donor and acceptor respectively. Most polymeric systems are assumed to be incompressible, where the constraint $(\phi_D(\mathbf{r}) + \phi_A(\mathbf{r}) = 1)$ holds. In the systems of interest in this article, the exciton undergoes dissociation at the donor-acceptor interface, where the binding energy is reduced by the difference in electron affinities of the two materials. To account for the latter feature, we model the effect of interface on E_{b0} by modifying it as:

$$E_b = E_{b0} - \alpha |\nabla \phi_A| \Delta\chi. \tag{6.14}$$

In the above, α is a phenomenological constant and $\Delta\chi$ represents the difference in electron affinities of the two materials (In pure donor and acceptor phases, the exciton binding energy is assumed to be unaffected). A second feature relates to the issue discussed in the introduction that experimental evidences point to the fact that the mobilities of holes and excitons not only depend on the spatially varying density profiles and electric fields, but are also expected to be anisotropic and in general to be different along the backbone of the donors compared to perpendicular to it. To account for the latter feature, we generalize the above function forms (Eq. (6.13)) to allow the mobilities $\boldsymbol{\mu}_x$ and $\boldsymbol{\mu}_p$ to be anisotropic tensors which depend on the average state of orientation of the rods. We further assume that the information regarding the average state of orientation of the rods is available (as output of a morphological model) and characterized by an orientational order parameter $\mathbf{S}(\mathbf{r})$ [8, 10, 96].

To illustrate the above modifications, we explain how the hole mobility is influenced by the density variations and orientational ordering of one of the species. Explicitly, the hole mobility is assumed to be of the form:

$$\boldsymbol{\mu}_p(\mathbf{r}) = \mu_p^I(\mathbf{r})\mathbf{I} + \mu_p^S(\mathbf{r})\mathbf{S}(\mathbf{r}), \tag{6.15}$$

where μ_p^I and μ_p^S denote the isotropic and anisotropic term respectively and $\mathbf{I}$ denotes is the identity matrix. The magnitude of orientational order parameter ($S(\mathbf{r})$) is equal to the maximum value of eigenvalue of the $\mathbf{S}(\mathbf{r})$ matrix at a given point $\mathbf{r}$. The coefficients $\mu_p^I(\mathbf{r})$ and $\mu_p^S(\mathbf{r})$ (in the eq. (6.15)) are in turn assumed to be dependent on the volume fractions of the donor and acceptor species as:

$$\mu_p^j(\mathbf{r}) = \mu_{pA}^j(\mathbf{E})\phi_A(\mathbf{r}) + \mu_{pD}^j(\mathbf{E})\phi_D(\mathbf{r}) \quad (j = I, S). \tag{6.16}$$

Each of the above coefficients μ_{pA}^j and μ_{pD}^j are assumed to be of the Poole-Frenkel form (Eq. (6.13)). We quantify the anisotropy in mobilities of hole by a single parameter:

$$\mu_R = \mu_p^{S0}/\mu_{pD}^{I0}. \tag{6.17}$$

where the “0” superscript indicates zero-field mobilities (Eq. (6.13)).

The above generalized drift-diffusion formalism allows us to account for spatially varying morphologies and the anisotropy in charge transport within an internally consistent framework for donor-acceptor mixtures characterized by a continuous spatial variation of the morphologies of donor and acceptors, with the donor phases assumed to be characterized by anisotropic hole and exciton mobilities. We emphasize that the above model only requires as input the volume fraction profiles and the orientational order parameter in the donor phase and accommodates both donor-acceptor blends and block copolymers. We believe that this is a significant improvement over previous models and allows us to account for the effects of orientation and (potentially) crystallization of donors in prediction of photovoltaic properties. As noted in the introduction, Buxton and Clarke introduced a formalism for flexible block copolymers which in many respects is similar except in not incorporating the effects of anisotropic mobility [58]. Since not all equations were detailed in their article, we are unable to present a detailed comparison of the functional forms they used to modify their equations to account for compositional inhomogeneities.

The output of the above equations are the spatially varying electron, hole, exciton densities, the fluxes of electrons, holes, and excitons, and the electrostatic potentials. The photovoltaic response is measured in terms of a current - voltage ($J - V$) curve. The total current density (J) comprising of both electron and hole current density is evaluated as a function of applied voltage (V) between the two electrodes. The quantities typically of interest are: (i) The short circuit current (J_{SC}) which is obtained at zero voltage condition and is the maximum current obtainable from the solar cell; (ii) Open circuit voltage V_{OC} is the condition where the output current is zero and represents the maximum voltage obtainable from the solar cell. The photovoltaic efficiency (η) is dependent on the values of J_{SC} and V_{OC}. Explicitly, $\eta = FF \times J_{SC} \times V_{OC}/P_{in}$, where FF represents fill factor ($= P_{max}/J_{SC} \times V_{OC}$), and P_{in} represents input power. High values of J_{SC} and V_{OC} are desirable for efficient solar cell devices.

6.2.2 Non-Dimensionalization of Drift-Diffusion Equations

To render the drift-diffusion equations (Eq. (6.1)-(6.4))solvable, we need to non-dimensionalize the equations [137]. The concentrations are scaled by N, such that the spatial discretization is scaled by Debye length of $\Delta x = (\epsilon_0 k_B T/q^2 N)^{1/2} = 1$ nm. This spatial discretization results in $N = 1.438 \times 10^{24}$ m^{-3}. The electrostatic potential (ψ) is scaled by $k_B T/q$ and the zero-field mobilities are scaled by $\mu_{max} = 1 \times 10^{-8}$ m^{2}V^{-1}s^{-1}. Based on scaling analysis for any of the continuity equations, the timescale is automatically set as $\Delta t = \Delta x^2 q/\mu_{max} k_B T = \epsilon_0/qN\mu_{max} = 3.895$ ns. The drift-diffusion equations are now written in a scaled form -

$$\frac{\partial x}{\partial t} = \nabla \cdot [\boldsymbol{\mu}_x \cdot \nabla x] + AG(\mathbf{r}) - R_d(x) - AD(\mathbf{E}, x) + \frac{1}{4}R(n, p) \tag{6.18}$$

$$\frac{\partial n}{\partial t} = \nabla \cdot \mathbf{J}_n, + AD(\mathbf{E}, x) - R(n, p) \tag{6.19}$$

$$\frac{\partial p}{\partial t} = -\nabla \cdot \mathbf{J}_p + AD(\mathbf{E}, x) - R(n, p), \tag{6.20}$$

$$\nabla . (\epsilon_r \nabla \psi) = -(p - n). \tag{6.21}$$

where A is a scaling constant ($A = \epsilon_0/qN^2\mu_{max}$).

6.2.3 Boundary Conditions and Numerical Details

The above equations are supplemented by boundary conditions for charges at the electrodes. We adopt the thermionic injection and recombination model used in previous researches in this context [61, 164, 165]. Below the open circuit voltage (V_{OC}), electrons flow towards cathode and holes flow towards anode leading to next extraction of charges. Above V_{OC}, there is net injection of electrons at cathode and holes at anode. At V_{OC}, the injection of charges and recombination (extraction) will be exactly balanced leading to zero electric field. The following equations (in non-dimensional form) represent the boundary conditions for electrons and holes at cathode and anode.

$$\mathbf{J}_i = J_i^k \tag{6.22}$$

where i represents electrons (n) or holes (p), and k stands for either cathode (cat) or anode (an). We present the following equations for the four sets of boundary conditions for three different cases of electric field [166].

$$J_n^{cat} = \begin{cases} B\mu_n(N_0 e^{-(\phi_{bn}^{ca}+q|E|r_c/4)/k_BT} - n_c), \;\; E > 0, \\ B\mu_n(N_0 e^{-\phi_{bn}^{ca}/k_BT} - n_c), \;\; E = 0, \\ B\mu_n\left(N_0 e^{-\phi_{bn}^{ca}/k_BT} e^{\sqrt{f}} - n_c\left(\frac{1}{\psi^2} - f\right)/4\right), \;\; E < 0. \end{cases} \tag{6.23}$$

$$J_p^{cat} = \begin{cases} B\mu_p(-P_0 e^{-(\phi_{bp}^{ca}+q|E|r_c/4)/k_BT} + p_c), \;\; E < 0, \\ B\mu_p(-P_0 e^{-\phi_{bp}^{ca}/k_BT} + p_c), \;\; E = 0, \\ B\mu_p\left(-P_0 e^{-\phi_{bp}^{ca}/k_BT} e^{\sqrt{f}} + p_c\left(\frac{1}{\Psi^2} - f\right)/4\right), \;\; E > 0. \end{cases} \tag{6.24}$$

$$J_p^{an} = \begin{cases} B\mu_p(P_0 e^{-(\phi_{bp}^{an}+q|E|r_c/4)/k_BT} - p_a), \;\; E > 0, \\ B\mu_p(P_0 e^{-\phi_{bp}^{an}/k_BT} - p_a), \;\; E = 0, \\ B\mu_p\left(P_0 e^{-\phi_{bp}^{an}/k_BT} e^{\sqrt{f}} - p_a\left(\frac{1}{\Psi^2} - f\right)/4\right), \;\; E < 0. \end{cases} \tag{6.25}$$

$$J_n^{an} = \begin{cases} B\mu_n(-N_0 e^{-(\phi_{bn}^{an}+q|E|r_c/4)/k_BT} + n_a), \;\; E < 0, \\ B\mu_n(-N_0 e^{-\phi_{bn}^{an}/k_BT} + n_a), \;\; E = 0, \\ B\mu_n\left(-N_0 e^{-\phi_{bn}^{an}/k_BT} e^{\sqrt{f}} + n_a\left(\frac{1}{\Psi^2} - f\right)/4\right), \;\; E > 0. \end{cases} \tag{6.26}$$

In the above equations, ϕ_{bi}^{ca} and ϕ_{bi}^{an} represent the barrier height for ith charge ($i = n,\, p$) at cathode and anode respectively. N_0 and P_0 are the densities of chargeable sites in the organic material. p_a and p_c are the densities of holes at anode and cathode respectively. n_a and n_c are the densities of electrons at anode and cathode respectively. In the above equations, the non-dimensional values of mobilities and densities is utilized. The expressions for remaining parameters and constants (expressed in non-dimensional terms) is given below. The origin of these terms can be found in more detail in the article by Lacic and Inganas [166].

$$B = 16\pi\epsilon_0\epsilon_r k_B T \times 10^{-9} \tag{6.27}$$

The Coulomb radius (r_c) is the distance between electron and hole where the

Coulombic binding energy exceeds $k_B T$,

$$r_c = q^2/4\pi\epsilon_0\epsilon_r k_B T \tag{6.28}$$

$$\Psi = f^{-1} + f^{-1/2} - f^{-1}\sqrt{1 + 2\sqrt{f}} \tag{6.29}$$

where,

$$f = qEr_c/k_B T \tag{6.30}$$

The drift-diffusion equations are numerically discretized using Scharfetter-Gummel scheme [167]. Conjugate gradient method is used to evolve the Poisson's equation while Crank-Nicholson method is used to obtain electron, hole and exciton densities at each new time step [93].

6.2.4 Parameters

The model detailed in the previous section involves a number of parameters. In this work, we fixed most of the device parameters and mainly focus on the interplay of the morphologies and anisotropic mobilities on the photovoltaic behavior. Most of the following parameters have been taken from the paper of Buxton and Clarke [58]. The zero field mobilities of electron in acceptor and donor regions are taken to be $1\times10^{-8}\text{m}^2\text{V}^{-1}\text{s}^{-1}$ and $1\times10^{-11}\text{m}^2\text{V}^{-1}\text{s}^{-1}$, respectively ($\mu^0_{nA}$ and μ^0_{nD}). The zero field mobilities of holes in the donor and acceptor regions are taken to be $1\times10^{-8}\text{m}^2\text{V}^{-1}\text{s}^{-1}$ and $1\times10^{-11}\text{m}^2\text{V}^{-1}\text{s}^{-1}$, respectively ($\mu^0_{pD}$ and μ^0_{pA}). The exciton mobility, μ_x is fixed at $3.86\times10^{-9}\text{m}^2\text{V}^{-1}\text{s}^{-1}$, and has a lifetime, τ_x of 1μs. The field dependent mobility parameter is taken to be $\gamma = 5 \times 10^{-4}\mathrm{m}^{1/2}\mathrm{V}^{-1/2}$ (Eq. (6.13)). The exciton binding energy is taken to be 0.5eV and the Schottky barrier height for injection of charge carriers is taken to be 0.5eV. The built in voltage is assumed to be 0.5V [58]. The spatial discretization used is 1 nm. The value of relative permittivity is chosen to be uniform throughout the device as, $\epsilon_r = 3.4$. The phenomenological parameter α is taken to be $2 \times 10^{-18}\ m^2$. The densities of chargeable sites are, $N_0 = 378$ and $P_0 = 128$ in non-dimensional units [166].

6.2.5 SCFT Model For Donor-Acceptor Morphologies

To model the self-assembly of confined rod-coil block copolymers, we use the model of Pryamitsyn and Ganesan [8] which utilizes self-consistent field theory (SCFT) to model the self-assembly of rod-coil block copolymers in the bulk. Along lines similar to the earlier work on flexible block copolymers, [16] we extended the model to incorporate the effects of confinement and surface interactions upon self-assembly along the similar lines of Matsen.

Briefly, the key ingredients utilized in our SCFT model are the Flory-Huggins interactions to model the repulsive interactions between the rod and coil block, Gaussian stretching energy for the coil block, and Maier Saupe potential to describe the orientational ordering between liquid crystalline rod molecules. The phase diagram in thin-films of rod-coil block copolymers is affected by volume fraction of one of the blocks (f), the Flory-Huggins interactions parameter (χN), the Maier Saupe parameter (ωN), the size asymmetry ratio β, and the surface interactions [45, 7, 125, 8, 168]. We utilize this model to obtain the densities and orientational order parameter ($\phi_A(\mathbf{r})$, $\phi_D(\mathbf{r})$, and $\mathbf{S}(\mathbf{r})$) which are utilized as input to our photovoltaic model. All the length-scales in the SCFT model are normalized by radius of gyration of the coil block, R_g. For using these morphologies in our photovoltaic model, we use a conversion factor of $R_g = 3.33$ nm.

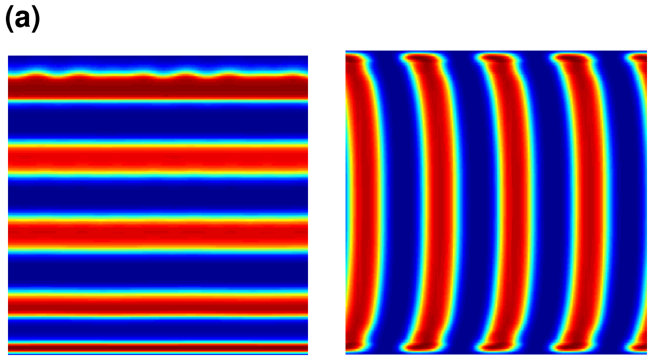

Parallel Lamellae **Perpendicular Lamellae**

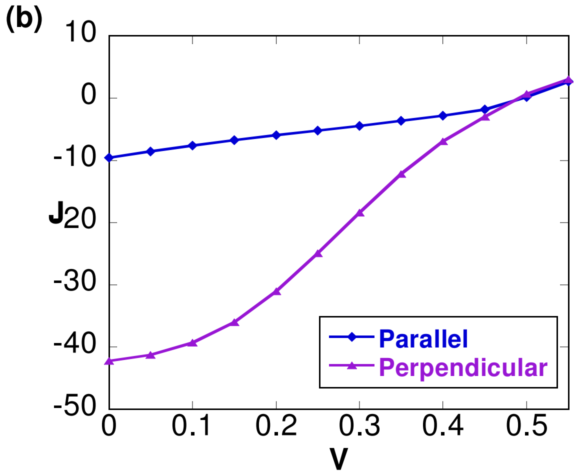

Figure 6.1: (a) Density profiles for donor and acceptor phases for parallel lamellae, and perpendicular lamellae. The coil block is shown in red and the rod block is shown in the blue phase. The parameters are: $\chi N = 10$, $f = 0.40$, $\omega N = 30$, and $\beta = 6$. (b) J-V curves for the above phases. The units are Am^{-2} for current density (J), and Volts for voltage (V).

6.3 Results and Discussion

6.3.1 Influence of the morphology of self-assembly upon device characteristics

In Fig. 6.1(a), we display two representative morphologies arising from the self-assembly of rod-coil block copolymers in confined situations. These are lamellar morphologies which are oriented parallel and perpendicular to the confining surfaces. The molecular parameters (χN, ωN, f, and β) for both parallel and perpendicular lamellae were kept the same. However, for the case of perpendicular lamellae the confining surfaces had no preferential interactions with either of the polymers. In contrast, the parallel morphology was achieved for the case when the anode surface was assumed to prefer the rod (donor) phase, whereas, the coil (acceptor) was favored at the cathode. In both the parallel and the perpendicular morphologies, the conditions were such that the rods were aligned perpendicular to the interface between rods and coils (Smectic A morphology).

From the Fig. 6.1(b), it is evident that the device having perpendicular lamellae ($\eta = 0.75\%$) exhibits better performance than parallel lamellar morphology ($\eta = 0.16\%$) . Indeed, the perpendicular lamella phase benefits from several factors that are key for better performance of polymer solar cell devices. On the one hand, direct pathways exist for both electrons and holes to reach the respective electrodes. Moreover, since the rods are aligned perpendicular to the lamellar interface the excitons are able to reach the D-A interface easily because of the preference for transport of holes along the backbone of the donors. In contrast, the device possessing parallel lamellae benefits only from the donor-acceptor microphase separation and the fact that rods are aligned perpendicular to the surface of electrodes. The latter furnishes higher charge transport rates for holes to travel to the electrodes. However, the major disadvantage of parallel lamellae is that the layers of donors (rod phase) act as blocking layers for electrons and viceversa. Therefore in parallel lamellae, the donor-acceptor interfaces closer to the electrodes contribute towards charge generation and photocurrent, whereas the charges generated at other interfaces are mostly blocked by the alternating donor-acceptor lamellaes.

In general by carefully tuning the surface interactions and/or by applying external fields, it is possible to align the layers of block copolymers to be oriented parallel or perpendicular to the electrode interfaces. This raises the question, "in general, what is the role of the influence of orientation of the domains (relative to the electrodes) in influencing the device PV characteristics?" We note that in the example considered above, these considerations were complicated by the occurrence of multiple domains (which act as blocking layers) and the presence of anisotropic charge transport. Of interest is the specific influence of the orientation of the lamellae upon the PV device characteristics.

To study the effect of domain orientation on photovoltaic properties, we considered two model morphologies. In Fig. 6.2 (a), we show the schematics of parallel and perpendicular bilayer devices considered. To isolate the effects

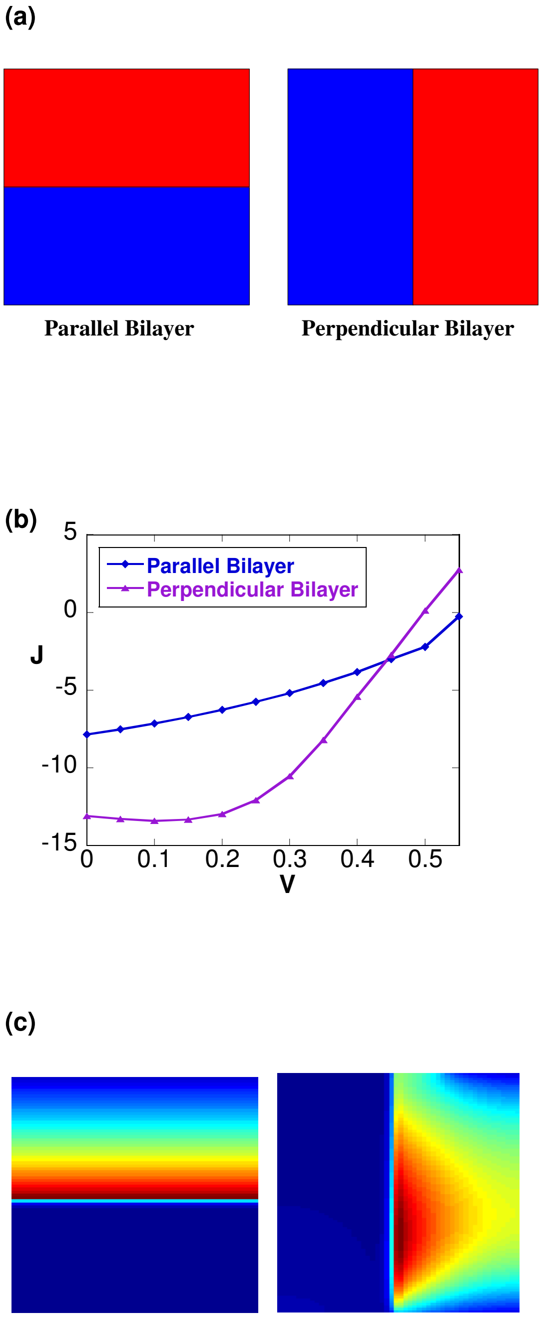

Figure 6.2: (a) Schematics for parallel and perpendicular bilayer morphology. The red phase is the acceptor layer and blue layer is the donor phase. (b) Effect of domain orientation on the J-V response. The units are Am^{-2} for current density (J), and Volts for voltage (V). (c) Electron density (n) for parallel and perpendicular bilayer morphology. $V = 0.45V$, $\Delta = 100nm$.

arising just from the orientation of the bilayers, we switch off the effects arising from the anisotropic mobilities (equivalently, we set $\mu_R = 0$ in Eq. (6.17)). In Fig. 6.2b, we display the J-V curves for the two cases illustrated in Fig. 6.2 (a). It is seen from the results that even for the case of a single donor-acceptor interface, having domains oriented perpendicular to the electrodes exhibits better performance relative to the parallel domains. Moreover, the reasoning discussed above is confirmed in the results for electron densities for parallel and perpendicular bilayers plotted in Fig. 6.2. We observe in Fig. 6.2(c) that there is a continuous generation of electrons (and equivalently holes) throughout the device in perpendicular domain orientation. Since more excitons can dissociate throughout the device and charges are generated throughout between the electrodes such a configuration leads to higher short-circuit current (J_{SC}). In contrast, only excitons generated within the exciton diffusion lengthscale of the interface are seen to diffuse to result in production of electrons. Consequently, only a small fraction of photons gets converted to charge carriers. With this reasoning, it is also evident that the efficacy of the parallel bilayer device would increase upon decreasing the thickness of the PV device.

We note that other "non-layered" self-assembly morphologies are also possible in confined rod-coil block copolymers [45, 8]. Fig. 6.3 displays one such case termed the puck phase ($\eta = 0.31\%$) and compares its device characteristics to the parallel and perpendicular lamellar phases. The puck phase morphology is achieved in rod-coil block copolymers at high volume fractions of the coil block. In comparing the device characteristics of puck phases to

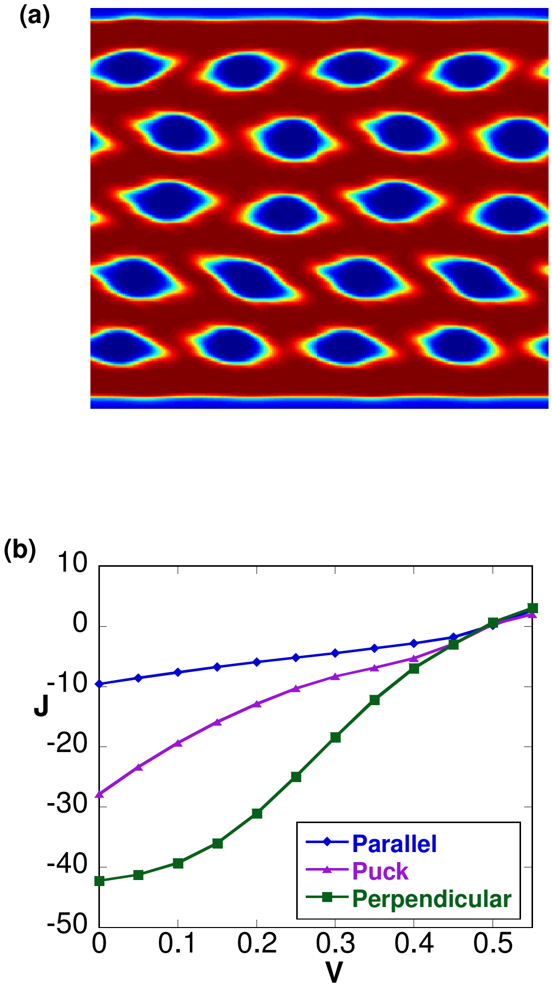

Figure 6.3: (a) Density profiles for donor and acceptor phases for puck phases. The parameters are $\chi N = 16$, $f = 06.$, $\omega N = 64$, and $\beta = 10$. (b) J-V curve for puck morphology compared with J-V curves for parallel and perpendicular morphology. It is quite evident that having straight nanostructured lamellar like morphologies between the two electrodes greatly improves the photovoltaic short-circuit current. The units are Am^{-2} for current density (J), and Volts for voltage (V).

the earlier-discussed lamellar morphologies it is seen that the puck phases exhibit performance intermediate to parallel and perpendicular lamellae. Indeed, while puck phases offer the advantage of high interfacial area between rods and coil blocks, they suffer from the absence of continuous pathways for holes to reach the anodes. While the former facilitates exciton dissociation and leads to higher production of free charges, the latter hinders hole transport. Another interesting thing to note is that whereas J-V curves for the lamellae are convex shaped, the J-V response for the puck phase morphology has a concave shape. This arises due to the presence of the acceptor phase at the anode which results in a buildup of electron charge at the wrong electrode. Such charge accumulation at organic layer-electrode interface has been documented to result in concave shaped J-V curve [169, 170]. Recently it has been shown in experiments in the context of rod-coil block copolymer solar cells that cylindrical nanostructures are aligned parallel to the surface [171] were less efficient relative to other morphologies. Our results are consistent with these observations.

In summary, our analysis suggests that for efficient charge transport and efficiencies, the donor and acceptor phases should have continuous nanochannels between the two electrodes. For the same reason, lamellar morphologies observed in rod-coil block copolymers exhibit more desirable characteristics than the non-lamellar morphologies dispersed phases like puck phases.

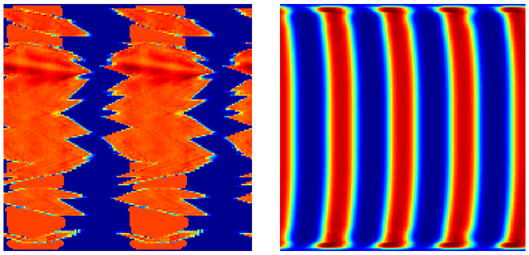

Blend Phase **Block Copolymer Microphase**

Figure 6.4: Representative density profiles for blend and block copolymer morphologies obtained from SCFT simulations. The domain size in block copolymers are much smaller than the blend morphologies. The blend morphology is obtained by simulating a blend of rod polymers and solvent in SCFT framework. It is easily observed that the domain sizes in block copolymers are much smaller as compared to blend systems.

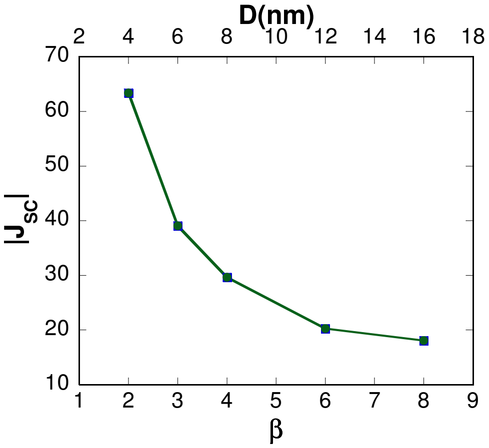

Figure 6.5: Effect of domain spacing for rod-coil block copolymers on the short-circuit current.

6.3.2 Effect of Domain Sizes

Donor-acceptor block copolymers offer unique advantages in the ability to control the domain sizes resulting from self-assembly. Indeed, this is most easily accomplished by either using longer block copolymers and/or mixing with a third component. In contrast, the domain sizes achieved in donor-acceptor blends tend to be much larger, and usually controlled by the kinetics of the phase separation process (Fig. 6.4)). These considerations motivate the question, “What is the influence of the domain sizes upon the PV device characteristics?” Specifically, of interest is whether there is an “optimum” domain size for achieving the best PV device characteristics.

At the outset, we address the above issue in the context of morphologies of rod-coil block copolymers. One possible means to modulate the domain sizes in rod-coil block copolymers is to vary the size asymmetry ratio β. β is a nondimensional parameter quantifying the length of the rod unit, and in the case of Smectic A morphology, the domain width in rod-coil block copolymer is directly proportional to the value of β [8]. In Fig. 6.5, we plot $|J_{SC}|$ as a function of the β parameter. To isolate the effects arising from the domain widths, the displayed device characteristics were computed within the framework of the isotropic transport model ($\mu_R = 0$). We observe that the short circuit current correlates inversely with the length of the donor units and the thickness of the domains. Smaller rod units facilitate more interfaces between the rod and coil phases, and in turn leads to enhanced production of electrons and holes. The overall behavior is governed by higher exciton dissociation due to presence of more number of interfaces. In the perpendicularly oriented lamellae, these charge carriers have direct access to the electrodes and therefore enhance the overall efficiency of the PV device.

It is however evident that the above trend cannot continue indefinitely to very small domain spacing. Indeed, at smaller domain widths, the recombination of electrons and holes are expected to become relevant and result in lower efficiencies. Unfortunately, due to numerical limitations, within the context of our SCFT model for rod-coil block copolymers, we were unable to achieve domain sizes smaller than those in the results displayed in Fig. 6.5. As an alternative, we considered "artificial" morphologies with prescribed domain widths to explore the interplay between recombination rates and domain widths. A schematic of such perpendicular multilayer morphology is shown in Fig. 6.6(a). In Fig. 6.6 (b), we display J_{SC} as a function of domain width obtained by varying the number of layers in the morphology shown in Fig. 6.6(a). Also, we monitor the effect of varying domain widths at different values of exciton lifetimes (τ_x). For the lowest value of τ_x, we observe that the plot is very similar to the one obtained for rod-coil block copolymers (Refer Fig. 6.5), where the value of J_{SC} reduces with increasing domain width. However, for higher values of τ_x we observe that there is an optimal width required for highest photocurrent. It is evident that the observed behavior results from an increase in the recombination probability which competes with the enhanced exciton generation and dissociation due to reduced domain width. At smaller domain widths, the charges are not efficiently separated at the interface and

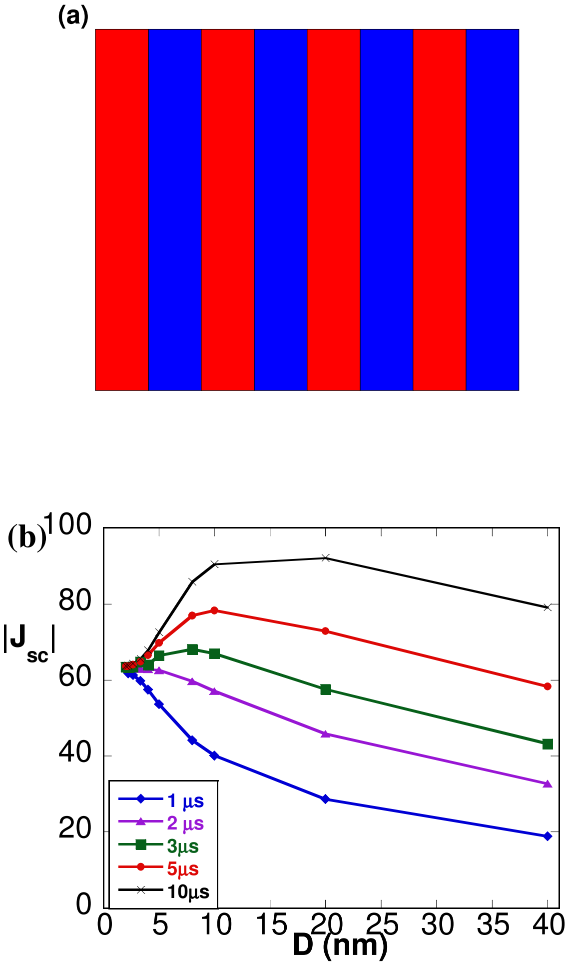

Figure 6.6: (a) Schematic of perpendicular multilayer morphology. (b) Effect of domain spacing for different exciton lifetimes. There exists an optimal domain width which produces the maximum J_{SC}.

there is a higher propensity for them to recombine. Increasing the value of exciton lifetime (τ_x) changes the exciton diffusion lengthscale ($l_D \sim \sqrt{\tau_x}$). For higher τ_x, the excitons can travel farther without decaying. Therefore increasing the value of exciton diffusion lengthscale will result in increasing the value of optimal domain width.

In summary, exciton dissociation competes with charge recombination to decide the optimal domain width required for efficient devices. We note that these results are consistent with Monte Carlo simulations that an optimal range of phase separation is needed for efficient device due to competition between the exciton dissociation and efficient charge separation [139]. It was also observed that optimal domain width increased upon increasing the exciton lifetime [139]. Our results qualitatively matched with the Monte Carlo simulation results on study of existence of optimal domain width arising from competition between exciton dissociation and charge recombination.

6.3.3 Effect of Chemical Incompatibility and Degree of Phase Separation

The chemical incompatibility between the donor and acceptor phases is another design parameter which can be modulated by choosing alternative combinations of donors and acceptors. Chemical incompatibility in turn determines features such as the degree of phase separation, the domain size, and also governs the nature of interfacial widths between the donor and acceptor. In our model, the chemical incompatibility between the two blocks of the block copolymer is embodied through the Flory-Huggins interaction parameter (χN). In this section, we present results for the device characteristics for different χN. To maintain the focus on the issue of interest, we use the isotropic transport version of our model.

In Fig, 6.7, we display the J-V curves for different values of χN. It is evident that increasing the value of Flory-Huggins parameter leads to an improvement in photovoltaic response. A jump in photocurrent is observed when the block copolymer undergoes microphase separation (cf. morphologies displayed in Fig. 6.7(a)). Increasing χN further is seen to enhance the efficiency of the PV device as seen in Fig. 6.7(b) These results can be rationalized based on two effects evident in the density profiles for different χNs. Higher χN is seen to correlate to purer donor and acceptor phases which results in improved transport properties for holes in the donor (rod) phase and electrons in the acceptor (coil) phase. A second effect evident is that increasing the chemical incompatibility results in a reduction of the interfacial width. We show in Fig. 6.7 (c) that for rod-coil block copolymer morphologies, the interfacial width (ξ) reduces with increase in degree of phase separation (χN). As we can observe from one dimensional rod density profiles plotted in Fig. 6.7 (a), the interface is thinner for higher χN (=20) than lower χN (=12). Smaller interfacial widths facilitates better charge separation by reducing the recombination probability. Together these effects are expected to result in better overall transport and device characteristics with increasing chemical incompatibility.

The above results are seen to involve the synergistic action of two distinct features. To further test our hypothesis specific to the correlation between the photovoltaic properties and the interfacial width, we utilized a perpendicular bilayer morphology (depicted in Fig. 6.2 (a)) and vary the interfacial width of the donor-acceptor interface. The variation of J_{SC} as a function of the interfacial width for this simulated morphology is displayed in Fig. 6.7 (d), and confirms that reducing interfacial width indeed improves the photovoltaic properties. It has been observed in experiments that solvents leading to better phase separation yield higher short circuit current and hence higher photovoltaic efficiencies [57]. Our results quantifies and confirms these observations.

6.3.4 Influence of anisotropic charge transport characteristics

In self-assembled rod-coil block copolymers, the rods can in general be oriented at an angle to the donor-acceptor interface (Smectic C phases and puck phases). An outstanding question is "Within the context of the proposed anisotropic transport model, what is the interplay between the morphology of self-assembly and the orientation of the rod molecules in influencing the PV device characteristics?" We note that in our SCFT model for rod-coil block copolymers, the propensity for orientational ordering arises through a Maier-Saupe orientational interaction term whose strength is quantified by the parameter ωN. To resolve this issue, we consider perpendicularly ori-

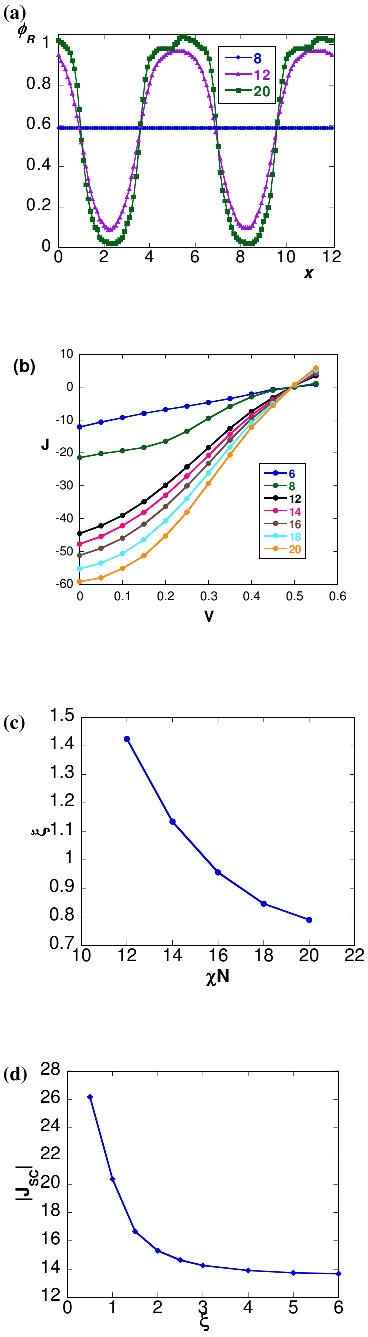

Figure 6.7: (a) 1D rod density profiles for $\chi N = 8$, $\chi N = 12$, and $\chi N = 20$. These are generated by considering a slice of perpendicular lamellar morphology. Well microphase separated lamellaes are observed for higher χN value. (b) J-V curves for different values of phase separation characterized by χN. The units are Am^{-2} for current density (J), and Volts for voltage (V). (c) The relationship between interfacial width (ξ) in non-dimensional units and χN. (d) The relationship between J_{SC} and ξ (nm) for artificial perpendicular bilayer morphology.

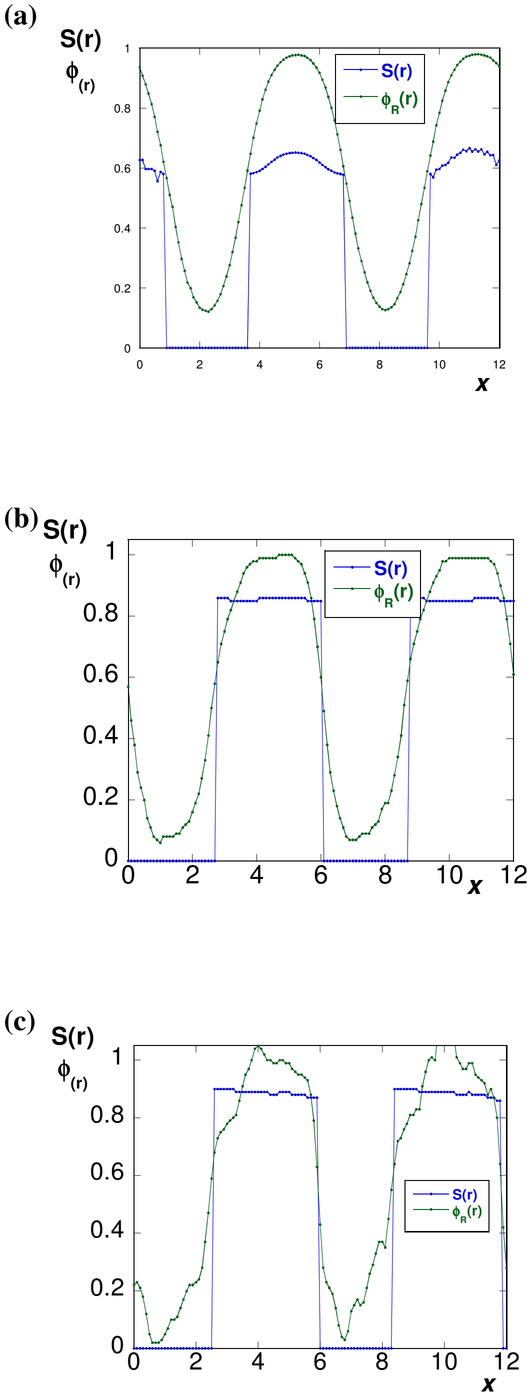

Figure 6.8: One dimensional density profiles of orientational order parameter ($S(\mathbf{r})$), and rod density ($\phi_R(\mathbf{r})$) for three values of ωN - (a) 15, (b) 40, and (c) 100.

ented lamellar morphologies generated with three different values of ωN. In Fig. 6.8, we plot orientational order parameter ($S(\mathbf{r})$), and rod density ($\phi_R(\mathbf{r})$) for three values of ωN : 15, 40 and 100. (Value of $\omega N \approx 15$ corresponds to isotropic-smectic transition, i.e. onset of orientational ordering in rod block)

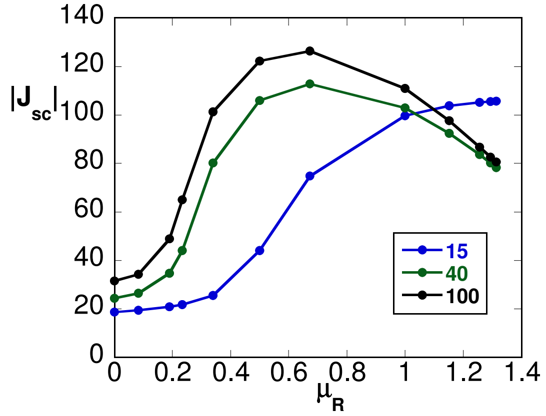

Figure 6.9: Effect of anisotropic mobility and orientational ordering on photocurrent. For well aligned rods, there exists an optimum value of μ_R which results in highest short-circuit current.

In Fig. 6.9, we plot the variation of absolute value of short circuit current (J_{SC}) as a function of μ_R for the three situations depicted in Fig. 6.8. Near the isotropic-smectic transition ($\omega N \approx 15$, S ≈ 0.6), the photovoltaic current is seen to increase with increasing anisotropy in the mobility of charge carriers and becomes constant for higher values of μ_R. On the other hand, for higher values of Maier-Saupe parameter (where nematic order parameter $S > 0.9$), the J_{SC} exhibits an optimal value of anisotropy (measured by μ_R) for which the photovoltaic current is maximum.

To rationalize the above results, we note that in perpendicular lamellae the rods are aligned parallel to the confining surfaces. Increasing μ_R increases the mobility along the polymer backbone (intrachain) and reduce the mobility along the interchain direction (refer Eq. (6.15)). As the mobility of holes and excitons is rendered more anisotropic, the rate of excitons traveling to interface and the subsequent charge separation improves. This is reflected in the larger efficiencies noted for morphologies with better orientational ordering ($\omega N = 40, 100$). However, the preceding effects are concomitantly accompanied by a reduction in the transport of holes to the anode (in the interchain direction). The non-monotonic trends observed in Fig. 6.9 can be rationalized as arising from an interplay of these two competing factors. At large μ_R, the interchain transport to the anode becomes the rate limiting step, leading to a lowering of the efficiency. It is evident that the competition between the transport in the parallel and perpendicular directions should depend on the magnitudes of both μ_R and S (cf. eq. (6.15)). Not surprisingly, in morphologies with pronounced orientational ordering, the optimal μ_R occurs at a smaller value relative to morphologies which are less ordered.

In Fig. 6.10, we consider the effect of interplay of anisotropy and thickness of the device on the short circuit current. We consider the case where the rods exhibit strong orientational ordering ($\omega N = 40$). We plot the value of short circuit current normalized by value of J_{SC} at zero anisotropy ($\mu_R = 0$) as a function of the degree of anisotropy. It was observed that short circuit

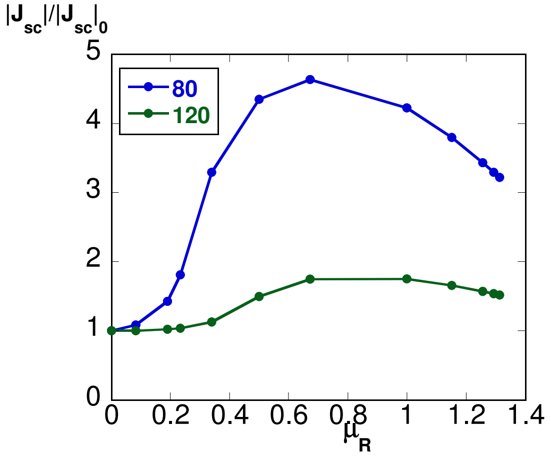

Figure 6.10: Effect of anisotropic mobility on photocurrent for two different thickness, 80 nm and 120 nm. The short circuit current is much higher in the thinner films. Also, the anisotropy effect is more pronounced for thinner devices. $\omega N = 40$.

current is much higher for thinner device (80 nm) as compared to the thicker device (120 nm) for all values of μ_R considered. This is because in a thinner film charges need to travel smaller distances to reach the electrodes. From Fig. 6.10, we see that the effect of anisotropy on J_{SC} is similar for both the film thicknesses. However, the effect of anisotropic charge transport is higher for thinner films as compared to thicker ones. The 80 nm device exhibits almost a five fold increase in short circuit current at the optimal value of anisotropy ($\mu_R = 0.67$). The relatively smaller effect of anisotropic charge transport on photocurrent for higher film thickness can be rationalized by noting that the charge transport in larger films are dictated mainly by the thickness of the film. The increase of transport along intrachain direction and the decrease along the interchain transport is relatively insignificant compared to the larger distance charges have to travel for a thicker film. Hence for optimal performance, a smaller device would be more appropriate.

We now discuss the interplay of domain size effects with the anisotropic transport of charges and excitons. For this, we considered the same morphologies used to generate Fig. 6.5, but computed the device curves with $\mu_R = 0.67$ (for comparison, we also display the isotropic case, $\mu_R = 0$). Increasing the degree of anisotropy in charge and exciton transport is seen to improve the photovoltaic response compared to the case where the charge transport was assumed to be isotropic. Interestingly, we observe that for $\mu_R = 0.67$, there is a optimal domain width for which the short circuit current is maximum. This contrasts with the situation for $\mu_R = 0$ where the short circuit current continuously increased upto the smallest domain sizes we probed.

As discussed in an earlier section (Sec. 6.3.1), the occurrence of an optimal domain width reflects an interplay between exciton dissociation and recombination. The results depicted in Fig. 6.5 reflect an increasing importance for recombination with increased anisotropy in charge transport. This is quantitatively illustrated in Fig. 6.11 (b), where we plot the variation of spatially averaged exciton dissociation rates and spatially averaged recombination rates for different values of β and for two values of μ_R. We clearly see that increasing the anisotropy in charge transport increases the recombination rate. If the domains are smaller and interfaces are close enough, there is an increased propensity in the case of anisotropic mobilities for the holes and

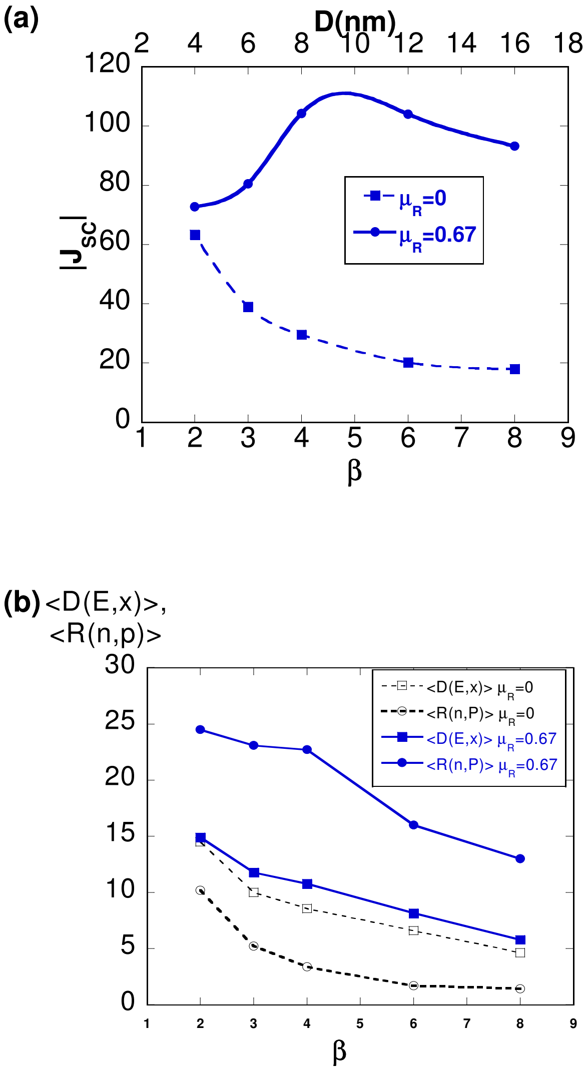

Figure 6.11: (a) Effect of domain spacing for rod-coil block copolymers on the short-circuit current. The variation of $|J_{SC}|$ as a function of domain size is different for isotropic and anisotropic charge transport. The units of J_{SC} is Am^{-2}. (b) The reduction in short circuit current is due to an increased recombination rate. The numbers on y-axis should be multiplied by 10^{26}, and units are $m^{-3}s^{-1}$.

electrons to undergo recombination. This competition between higher exciton dissociation and recombination leads to a peak in J_{SC} at an optimal domain size in perpendicular lamellaes of rod-coil block copolymers.

6.4 Summary and Outlook

In this research, we developed a model to understand the photovoltaic properties for polymer devices which consider as input the density and orientational ordering in donor and acceptor phases. This model improves upon the previous work by taking into account the anisotropic nature of charge transport in conjugated polymers. Our study focusses on self-assembly in rod-coil block copolymers as means to achieve desirable values of photovoltaic efficiency. Rod-coil block copolymers derive their advantages from their ability to form microphase separated morphologies and the capability for the rodlike units to be orientationally ordered. The perpendicularly oriented lamellar morphology was shown to be the most desirable morphology for obtaining high values of photocurrent. Also, the other factors that can improve the photovoltaic efficiency were a stronger degree of chemical incompatibility between the donor and acceptor units, and higher value of orientational order parameter. Such conditions lead to a well segregated microphase structure of rod-coil block copolymers having perfectly aligned rod molecules. Within these morphologies we demonstrated that an optimal domain spacing and optimal degree of anisotropy leads to the highest efficiencies.

Our model can be utilized to study other systems being considered for polymer solar cell devices like blends of conjugated molecules with fullerene derivatives [55, 57]. Our model provides the framework to calculate photovoltaic behavior (J-V curve) once the density of species and orientational ordering of conjugated molecules are known. Our future studies will address similar issues in the context of models for such donor-acceptor blends.

Chapter 7

Future Work

In this thesis, we have developed coarse grained models in the framework of self-consistent field theory (SCFT) to understand the self-assembly of block copolymers which have one “non-flexible” component, such as a rigid polymer (rod-coil block copolymer) or semiflexible unit (semicrystalline multiblock copolymers). These models can be extended and developed further to study other interesting systems. Our model for semicrystalline block copolymer only accounts for one dimensional lamellar morphologies of block copolymers. There is lot of interest in understanding the phase behavior of semicrystalline block copolymers where the microphase is not lamellar [12, 13, 33]. It will be interesting to see the effect of chain stiffness of one of the blocks on cylindrical and spherical microphases. Our model for flexible-semiflexible block copolymer can be extended to two and three dimensions in order to answer some of the questions related to interplay of block copolymer and chain orientational ordering in determining structure development of such polymers. In non-lamellar morphologies, it has been suggested that interblock segregation is enough to confine crystallization with the microdomains.[33]. The competition between interblock segregation (measured by χN) and orientational ordering (measured by λ and μN) will ultimately decide the final morphology. To solve the modified diffusion equation for semiflexible chain (as a model to semicrystalline chain), the real space approach adopted in this thesis (Chapter. 4) will be computationally exorbitant. Alternate techniques such as pseudo-spectral method proposed by Fredrickson [17] should be utilized to solve diffusion equation for wormlike chains in more than one dimensions. We evaluated bridging fractions for semicrystalline multiblock copolymer under the assumption of lamellar morphologies only. Once the SCFT model is extended to 2 and 3 dimensions, it will enable us to study the effect of morphology on bridging fractions.

One of the most important contributions of this thesis is to develop a theoretical framework to obtain photovoltaic properties dependent upon the phase separation of donor and acceptor phases and the orientational ordering of the semiconducting optically active rigid donor molecules (Refer Chapter. 6). We applied this methodology in drift-diffusion framework [159] for devices based on complex self assembly in semiconducting rod-coil block copolymers. Although our results were more relevant for block copolymer phase separation, the photovoltaic model in general can be adopted to obtain efficiencies for any blend or block copolymer exhibiting phase separation and orientational ordering in one or both the phases. Some of the other systems relevant for organic electronics applications which display similar characteristics as the above example are blend of semiconducting chain (e.g P3HT) and fullerene molecules [57], block copolymers and inorganic nanorods (e.g CdSe nanocrystals), and semiconducting donor chains blended with inorganic anisotropic nanocrystals (e.g TiO_2) [55, 146]. The study of photovoltaic properties in such systems will entail a two step approach. First, a mechanism to predict equilibrium morphologies in such systems need to be developed. Second, our continuum model to evaluate photovoltaic properties needs can be utilized in order to optimize the morphology development in these new systems.

Bibliography

[1] M. W. Matsen. The standard gaussian model for block copolymer melts. *Journal of Physics-Condensed Matter*, 14(2):R21–R47, January 2002.

[2] B. de Boer, U. Stalmach, P. F. van Hutten, C. Melzer, V. V. Krasnikov, and G. Hadziioannou. Supramolecular self-assembly and opto-electronic properties of semiconducting block copolymers. *Polymer*, 42(21):9097–9109, October 2001.

[3] M. Anthamatten and P. Hammond. A saxs study of microstructure ordering transitions in liquid crystalline side-chain diblock copolymers. *MACROMOLECULES*, 32(24):8066–8076, NOV 30 1999.

[4] F. S. Bates and G. H. Fredrickson. Block copolymers–designer soft materials. *Physics Today*, 52(2):32–, February 1999.

[5] F. S. Bates and G. H. Fredrickson. Block copolymer thermodynamics: Theory and experiment. *Annual Review of Physical Chemistry*, 41(1): 525–557, 1990.

[6] I. W. Hamley. *The Physics of the Block Copolymers.* Oxford Science Publications, 1998.

[7] B. Olsen and R. Segalman. Structure and thermodynamics of weakly segregated rod-coil block copolymers. *Macromolecules*, 38(24):10127–10137, 2005.

[8] V. Pryamitsyn and V. Ganesan. Self-assembly of rod–coil block copolymers. *The Journal of Chemical Physics*, 120(12):5824–5838, 2004.

[9] M. Anthamatten, W. Zheng, and P. Hammond. A morphological study of well-defined smectic side-chain lc block copolymers. *Macromolecules*, 32(15):4838–4848, 1999.

[10] M. Shah, V. Pryamitsyn, and V. Ganesan. A model for self-assembly in side chain liquid crystalline block copolymers. *Macromolecules*, 41: 218–229, 2008.

[11] A. Phatak, L. Lim, C. Reaves, and F. Bates. Toughness of glassy-semicrystalline multiblock copolymers. *Macromolecules*, 39(18):6221–6228, 2006.

[12] I. W. Hamley. Crystallization in block copolymers. *Adv. Polym. Sci.*, 148:113–137, 1999.

[13] Y.-L. Loo, R. Register, and A. Ryan. Modes of Crystallization in Block Copolymer Microdomains: Breakout, Templated, and Confined. *Macromolecules*, 35(6):2365–2374, 2002.

[14] A. Arceo and P. F. Green. *J. Phys. Chem. B*, 109:6958–, 2005.

[15] P. F. Green and R. Limary. Block copolymer thin films: pattern formation and phase behavior. *Advances in Colloid and Interface Science*, 94 (1-3):53–81, November 2001.

[16] M. W. Matsen. Thin films of block copolymer. *The Journal of Chemical Physics*, 106(18):7781–7791, May 1997.

[17] G. Fredrickson. *The Equilibrium Theory of Inhomogeneous Polymers.* Oxford Science Publications, 2006.

[18] G. Fredrickson, V. Ganesan, and F. Drolet. Field-Theoretic Computer Simulation Methods for Polymers and Complex Fluids. *Macromolecules*, 35(1):16–39, 2002.

[19] F. Drolet and G. Fredrickson. Optimizing chain bridging in complex block copolymers. *Macromolecules*, 34(15):5317–5324, 2001.

[20] G. H. Fredrickson. Theoretical profits. *Nat Mater*, 7(4):261–263, April 2008.

[21] M. Shah and V. Ganesan. Chain bridging in a model of semicrystalline multiblock copolymers. *The Journal of Chemical Physics*, 130(5):054904, 2009.

[22] A. Menelle, T. P. Russell, S. H. Anastasiadis, S. K. Satija, and C. F. Majkrzak. Ordering of thin diblock copolymer films. *Phys. Rev. Lett.*, 68(1):67–, January 1992.

[23] J. Watkins, G. Brown, V. RamachandraRao, M. Pollard, and T. Russell. Phase Separation in Polymer Blends and Diblock Copolymers Induced by Compressible Solvents. *Macromolecules*, 32(23):7737–7740, 1999.

[24] B. Vogt, V. RamachandraRao, R. Gupta, K. Lavery, T. Francis, T. Russell, and J. Watkins. Phase behavior of polystyrene-block-poly(n-alkyl methacrylate)s dilated with carbon dioxide. *Macromolecules*, 36(11): 4029–4036, 2003.

[25] H.-Y. Chen and G. H. Fredrickson. Morphologies of abc triblock copolymer thin films. *J. Chem. Phys.*, 116(3):1137–1146, January 2002.

[26] H. Morita, T. Kawakatsu, and M. Doi. Dynamic Density Functional Study on the Structure of Thin Polymer Blend Films with a Free Surface. *Macromolecules*, 34(25):8777–8783, 2001.

[27] M. Shah, V. Pryamitsyn, and V. Ganesan. Instabilities in block copolymer films induced by compressible solvents. *Journal of Physical Chemistry B*, 111(2):402–407, January 2007.

[28] K. K. Takashi Kato, Norihiro Mizoshita. Functional liquid-crystalline assemblies: Self-organized soft materials. *Angewandte Chemie International Edition*, 45(1):38–68, 2006.

[29] W. Zheng and P. Hammond. Phase Behavior of New Side Chain Smectic C* Liquid Crystalline Block Copolymers. *Macromolecules*, 31(3):711–721, 1998.

[30] I. Hamley, V. Castelletto, Z. Lu, C. Imrie, T. Itoh, and M. Al-Hussein. Interplay between smectic ordering and microphase separation in a series of side-group liquid-crystal block copolymers. *Macromolecules*, 37(13): 4798–4807, 2004.

[31] G. Mao, J. Wang, S. Clingman, C. Ober, J. Chen, and E. Thomas. Molecular design, synthesis, and characterization of liquid crystal-coil diblock copolymers with azobenzene side groups. *Macromolecules*, 30 (9):2556–2567, 1997.

[32] I. Hamley, J. Fairclough, N. Terrill, A. Ryan, P. Lipic, F. Bates, and E. Towns-Andrews. Crystallization in Oriented Semicrystalline Diblock Copolymers. *Macromolecules*, 29(27):8835–8843, 1996.

[33] Y.-L. Loo, R. Register, A. Ryan, and G. Dee. Polymer Crystallization Confined in One, Two, or Three Dimensions. *Macromolecules*, 34(26): 8968–8977, 2001.

[34] L.-B. Lee and R. Register. Equilibrium Control of Crystal Thickness and Melting Point through Block Copolymerization. *Macromolecules*, 37(19):7278–7284, 2004.

[35] S. Hong, W. MacKnight, T. Russell, and S. Gido. Structural Evolution of Multilayered, Crystalline-Amorphous Diblock Copolymer Thin Films. *Macromolecules*, 34(9):2876–2883, 2001.

[36] C. Koo, M. Hillmyer, and F. Bates. Structure and properties of semicrystalline-rubbery multiblock copolymers. *Macromolecules*, 39(2): 667–677, 2006.

[37] C. Koo, L. Wu, L. Lim, M. Mahanthappa, M. Hillmyer, and F. Bates. Microstructure and mechanical properties of semicrystalline-rubbery-semicrystalline triblock copolymers. *Macromolecules*, 38(14):6090–6098, 2005.

[38] E. A. DiMarzio, C. M. Guttman, and J. D. Hoffman. Calculation of Lamellar Thickness in a Diblock Copolymer, One of Whose Components Is Crystalline. *Macromolecules*, 13(5):1194–1198, 1980.

[39] T. Vilgis and A. Halperin. Aggregation of coil-crystalline block copolymers: equilibrium crystallization. *Macromolecules*, 24(8):2090–2095, 1991.

[40] M. D. Whitmore and J. Noolandi. Theory of crystallizable block copolymer blends. *Macromolecules*, 21(5):1482–1496, May 1988.

[41] P. J. Flory. Statistical thermodynamics of semi-flexible chain molecules. *Proceedings of the Royal Society of London. Series A, Mathematical and Physical Sciences*, 234(1196):60–73, 1956.

[42] W. Hu, D. Frenkel, and V. Mathot. Intramolecular Nucleation Model for Polymer Crystallization. *Macromolecules*, 36(21):8178–8183, 2003.

[43] W. B. Hu and D. Frenkel. Polymer crystallization driven by anisotropic interactions. *Adv. Polym. Sci.*, 191:1–35, 2005.

[44] J. Chen, D. Markiewicz, V. Lee, G. Klaerner, R. Miller, and J. Scott. Improved efficiencies of light-emitting diodes through incorporation of charge transporting components in tri-block polymers. *Synthetic Metals*, 107(3):203–207, December 1999.

[45] B. Olsen, X. Li, J. Wang, and R. Segalman. Thin film structure of symmetric rod-coil block copolymers. *Macromolecules*, 40(9):3287–3295, 2007.

[46] Y. Tao, B. Ma, and R. A. Segalman. Self-assembly of rod-coil block copolymers and their application in electroluminescent devices. *Macromolecules*, 41(19):7152–7159, 2008.

[47] G. G. Pereira and D. R. M. Williams. Smectic rod-coil melts confined between flat plates: Monolayer - bilayer and parallel-perpendicular transitions. *Macromolecules*, 33(8):3166–3172, 2000.

[48] T. Hermel, S. Hahn, K. Chaffin, W. Gerberich, and F. Bates. Role of molecular architecture in mechanical failure of glassy/semicrystalline block copolymers: Cec vs cecec lamellae. *Macromolecules*, 36(7):2190–2193, 2003.

[49] C. Honeker and E. Thomas. Impact of morphological orientation in determining mechanical properties in triblock copolymer systems. *Chemistry of Materials*, 8(8):1702–1714, 1996.

[50] R. J. Spontak and N. P. Patel. Thermoplastic elastomers: fundamentals and applications. *Current Opinion in Colloid & Interface Science*, 5 (5-6):333–340, November 2000.

[51] A. Hotta, E. Cochran, J. Ruokolainen, V. Khanna, G. H. Fredrickson, E. J. Kramer, Y.-W. Shin, F. Shimizu, A. E. Cherian, P. D. Hustad, J. M. Rose, and G. W. Coates. Semicrystalline thermoplastic elastomeric polyolefins: Advances through catalyst development and macromolecular design. *Proceedings of the National Academy of Sciences*, 103(42): 15327–15332, 2006.

[52] C. Ryu, J. Ruokolainen, G. Fredrickson, E. Kramer, and S. Hahn. Chain architecture effects on deformation and fracture of block copolymers with unentangled matrices. *Macromolecules*, 35(6):2157–2166, 2002.

[53] Y. Mori, L. Lim, and F. Bates. Consequences of molecular bridging in lamellae-forming triblock/pentablock copolymer blends. *Macromolecules*, 36(26):9879–9888, 2003.

[54] E. B. Zhulina and A. Halperin. Lamellar mesogels and mesophases: a self-consistent-field theory. *Macromolecules*, 25(21):5730–5741, 1992.

[55] K. Coakley and M. McGehee. Conjugated polymer photovoltaic cells. *Chemistry of Materials*, 16(23):4533–4542, 2004.

[56] A. C. Mayer, S. R. Scully, B. E. Hardin, M. W. Rowell, and M. D. McGehee. Polymer-based solar cells. *Materials Today*, 10(11):28–33, November 2007.

[57] S. E. Shaheen, C. J. Brabec, N. S. Sariciftci, F. Padinger, T. Fromherz, and J. C. Hummelen. 2.5 *Applied Physics Letters*, 78(6):841–843, 2001.

[58] G. A. Buxton and N. Clarke. Predicting structure and property relations in polymeric photovoltaic devices. *Physical Review B (Condensed Matter and Materials Physics)*, 74(8):085207, 2006.

[59] G. Hadziioannou. Semiconducting block copolymers for self-assembled photovoltaic devices. *MRS Bulletin*, 27:456–460, 2002.

[60] S. Lindner and M. Thelakkat. Nanostructures of n-type organic semiconductor in a p-type matrix via self-assembly of block copolymers. *Macromolecules*, 37(24):8832–8835, 2004.

[61] J. A. Barker, C. M. Ramsdale, and N. C. Greenham. Modeling the current-voltage characteristics of bilayer polymer photovoltaic devices. *Phys. Rev. B*, 67(7):075205, Feb 2003.

[62] L. J. A. Koster, V. D. Mihailetchi, H. Xie, and P. W. M. Blom. Origin of the light intensity dependence of the short-circuit current of polymer/fullerene solar cells. *Applied Physics Letters*, 87(20):203502, 2005.

[63] C.-I. Huang and T. P. Lodge. Self-consistent calculations of block copolymer solution phase behavior. *Macromolecules*, 31(11):3556–3565, June 1998.

[64] J. Naughton and M. Matsen. Limitations of the Dilution Approximation for Concentrated Block Copolymer/Solvent Mixtures. *Macromolecules*, 35(14):5688–5696, 2002.

[65] R. Limary, P. F. Green, and K. R. Shull. *Eur. Phys. J. E*, 8:103–, 2002.

[66] K. R. Shull. Mean-field theory of block copolymers: bulk melts, surfaces, and thin films. *Macromolecules*, 25(8):2122–2133, 1992.

[67] D. K. Taylor, J. S. Keiper, and J. M. DeSimone. *Ind. Eng. Chem. Res.*, 41:4451–, 2002.

[68] T. Koga, E. Akashige, A. Reinstein, A. Bronner, Y. Seo, K. Shin, M. Rafailovich, J. Sokolov, B. Chu, and S. Satija. The effect of density fluctuations in supercritical fluids: new science and technology for polymer thin films. *PHYSICA B-CONDENSED MATTER*, 357(1-2): 73–79, FEB 28 2005.

[69] Y. C. Lin, M. Muller, and K. Binder. *J. Chem. Phys.*, 121:3816–, 2004.

[70] L. Reichl. *A Modern Course in Statistical Physics*. John Wiley, New York, 1998.

[71] A. Raudino, F. L. Celso, A. Triolo, and R. Triolo. *J. Chem. Phys.*, 120: 3489–, 2004.

[72] K. Nishikawa and I. Tanaka. *Chem. Phys. Lett.*, 244:149–, 1995.

[73] S. M. Sirard, K. J. Ziegler, I. C. Sanchez, P. F. Green, and K. P. Johnston. *Macromolecules*, 35:1928–, 2002.

[74] E. W. Cochran, C. J. Garcia-Cervera, and G. H. Fredrickson. *Macromolecules*, 39:2449–, 2006.

[75] G. FREDRICKSON. Surface ordering phenomena in block copolymer melts. *MACROMOLECULES*, 20(10):2535–2542, OCT 1987.

[76] P. F. Green. Wetting and dynamics of structured liquid films. *Journal of Polymer Science Part B: Polymer Physics*, 41(19):2219–2235, 2003.

[77] P. Mansky, O. K. C. Tsui, T. P. Russell, and Y. Gallot. *Macromolecules*, 32:4832–, 1999.

[78] T. Kato, N. Mizoshita, and K. Kishimoto. Functional liquid-crystalline assemblies: Self-organized soft materials. *ANGEWANDTE CHEMIE-INTERNATIONAL EDITION*, 45(1):38–68, 2006.

[79] J. T. Chen, E. L. Thomas, C. K. Ober, and G.-p. Mao. Self-assembled smectic phases in rod-coil block copolymers. *Science*, 273(5273):343–346, July 1996.

[80] G. Mao and C. Ober. Block copolymers containing liquid crystalline segments. *ACTA POLYMERICA*, 48(10):405–422, OCT 1997.

[81] H. Fischer and S. Poser. Liquid crystalline block and graft copolymers. *ACTA POLYMERICA*, 47(10):413–428, OCT 1996.

[82] E. L. Thomas, J. T. Chen, M. J. E. O'Rourke, C. K. Ober, and G. Mao. *Macromolecular Symoposia*, 117:241–, 1997.

[83] C. Osuji, J. Chen, G. Mao, C. Ober, and E. Thomas. Understanding and controlling the morphology of styrene-isoprene side-group liquid crystalline diblock copolymers. *POLYMER*, 41(25):8897–8907, DEC 2000.

[84] E. Verploegen, L. C. McAfee, L. Tian, D. Verploegen, and P. T. Hammond. *Macromolecules*, 40:777–, 2007.

[85] M. Anthamatten and P. T. Hammond. Free-energy model of asymmetry in side-chain liquid-crystalline diblock copolymers. *Journal of Polymer Science Part B-Polymer Physics*, 39(21):2671–2691, November 2001.

[86] R. Wang, Z. Jiang, and J. Hu. Order to disorder transition of comb copolymer am+1bm: a self-consistent field study. *Polymer*, 46(16):6201–6207, July 2005.

[87] A. Shinozaki, D. Jasnow, and A. Balazs. *Macromolecules*, 27:2496–, 1994.

[88] R. J. Nap and G. Brinke. *Macromolecules*, 35:952–, 2002.

[89] M. W. Matsen and F. S. Bates. *Macromolecules*, 29:1091–, 1996.

[90] A. N. Semenov. *Sov. Phys. JETP*, 61:733–, 1985.

[91] M. W. Matsen and C. Barrett. *J. Chem. Phys.*, 109:4108–, 1998.

[92] M. W. Matsen and M. Schick. Stable and unstable phases of a diblock copolymer melt. *Physical Review Letter*, 72(16):2660–2663, April 1994.

[93] W. Press, S. Teukolsky, W. Vetterling, and B. Flannery. *Numerical Recipes in Fortran*. Cambridge University Press, 1992.

[94] A. SEMENOV. Contribution to the theory of microphase layering in block-copolymer melts. *ZHURNAL EKSPERIMENTALNOI I TEORETICHESKOI FIZIKI*, 88(4):1242–1256, 1985.

[95] E. Helfand and A. M. Sapse. *J. Chem. Phys.*, 62:1327–, 1975.

[96] P. G. de Gennes. *The Physics of the Liquid Crystals*. Oxford University Press, 1974.

[97] R. L. Jones, L. Kane, and R. J. Spontak. Morphological characteristics of lamellar aba triblock copolymers: A self-consistent field treatment. *Chemical Engineering Science*, 51(9):1365–1375, May 1996.

[98] M. Matsen and M. Schick. Lamellar phase of a symmetric triblock copolymer. *Macromolecules*, 27(1):187–192, 1994.

[99] M. W. Matsen and R. B. Thompson. Equilibrium behavior of symmetric aba triblock copolymer melts. *The Journal of Chemical Physics*, 111(15): 7139–7146, 1999.

[100] S. Rane and P. Gujrati. Theory of crystallization under equilibrium polymerization in a solution and the investigation of its melting properties. *Macromolecules*, 38(21):8734–8748, 2005.

[101] P. D. Gujrati and M. Goldstein. On the validity of the flory–huggins approximation for semiflexible chains. *The Journal of Chemical Physics*, 74(4):2596–2603, 1981.

[102] J. D. McCoy, K. G. Honnell, K. S. Schweizer, and J. G. Curro. Crystallization of polyethylene and polytetrafluoroethylene by density-functional methods. *The Journal of Chemical Physics*, 95(12):9348–9366, 1991.

[103] P. van der Schoot. Green-function description of dense polymeric systems. *Macromolecules*, 33(22):8497–8503, 2000.

[104] W. Hu, D. Frenkel, and V. B. F. Mathot. Lattice-model study of the thermodynamic interplay of polymer crystallization and liquid–liquid demixing. *The Journal of Chemical Physics*, 118(22):10343–10348, 2003.

[105] W. B. Hu and D. Frenkel. Oriented primary crystal nucleation in lamellar diblock copolymer systems. *Faraday Discussions*, 128:253–260, 2005.

[106] M. Muthukumar. Commentary on theories of polymer crystallization. *The European Physical Journal E - Soft Matter*, 3(2):199–202, October 2000.

[107] P. Welch and M. Muthukumar. Molecular mechanisms of polymer crystallization from solution. *Phys. Rev. Lett.*, 87(21):218302–, November 2001.

[108] J. D. Hoffman, G. Davis, and J. I. Lauritzen. *Treatise on Solid State Chemistry.* Plenum Press, New York, 1976.

[109] D. Sadler and G. Gilmer. A model for chain folding in polymer crystals: rough growth faces are consistent with the observed growth rates. *Polymer*, 25(10):1446–1452, October 1984.

[110] K. C. Douzinas, R. E. Cohen, and A. F. Halasa. Evaluation of domain spacing scaling laws for semicrystalline diblock copolymers. *Macromolecules*, 24(15):4457–4459, 1991.

[111] M. W. Matsen. Melts of semiflexible diblock copolymer. *The Journal of Chemical Physics*, 104(19):7758–7764, May 1996.

[112] D. Duchs and D. E. Sullivan. Entropy-induced smectic phases in rod–coil copolymers. *Journal of Physics: Condensed Matter*, 14 (46):12189–12202, 2002.

[113] K. Daoulas, D. Theodorou, V. Harmandaris, N. Karayiannis, and V. Mavrantzas. Self-consistent-field study of compressible semiflexible melts adsorbed on a solid substrate and comparison with atomistic simulations. *Macromolecules*, 38(16):7134–7149, 2005.

[114] R. R. Netz and M. Schick. Liquid-crystalline phases of semiflexible diblock copolymer melts. *Phys. Rev. Lett.*, 77:302–305, 1996.

[115] C. G. Gray and K. E. Gubbins. *Theory of Molecular Fluids:Vol 1. Fundamentals.* Oxford: Clarendon, 1984.

[116] G. D. Smith. *Numerical Solution of Partial Differential Equations: Finite Difference Methods.* Clarendon Press; Oxford Science Publications, 1985.

[117] J. Ruokolainen, G. Fredrickson, E. Kramer, C. Ryu, S. Hahn, and S. Magonov. Effect of thermal history and microdomain orientation

on deformation and fracture properties of poly(cyclohexylethylene)-polyethylene triblock copolymers containing cylindrical pe domains. *Macromolecules*, 35(25):9391–9402, 2002.

[118] H. Watanabe. Slow dielectric relaxation of a styrene-isoprene-styrene triblock copolymer with dipole inversion in the middle block: A challenge to a loop/bridge problem. *Macromolecules*, 28(14):5006–5011, 1995.

[119] B. Li and E. Ruckenstein. The equilibrium fraction of bridging chains and the swelling behavior of aba triblock copolymer mesophases. *Macromolecular Theory and Simulations*, 7(3):333–348, 1998.

[120] A. Halperin. On bridging and mesogels. *J. Adhesion*, 58:1–13, 1996.

[121] A. Halperin and D. R. M. Williams. Nematic networks: on thermoelasticity and the bridging fraction. *Macromolecules*, 26(24):6652–6653, 1993.

[122] M. Sommer, S. Httner, S. Wunder, and M. Thelakkat. Electron-conducting block copolymers: Morphological, optical, and electronic properties. *Advanced Materials*, 20(13):2523–2527, 2008.

[123] L. H. Radzilowski, B. O. Carragher, and S. I. Stupp. *Macromolecules*, 30:2110–, 1997.

[124] D. R. M. Williams and G. H. Fredrickson. Cylindrical micelles in rigid-flexible diblock copolymers. *Macromolecules*, 25:3561, 1992.

[125] B. D. Olsen, M. Shah, V. Ganesan, and R. A. Segalman. Universalization of the phase diagram for a model rod-coil diblock copolymer. *MACROMOLECULES*, 41(18):6809–6817, SEP 23 2008.

[126] R. A. Segalman. Patterning with block copolymer thin films. *Materials Science and Engineering: R: Reports*, 48(6):191–226, February 2005.

[127] G. T. Pickett and A. C. Balazs. Equilibrium orientation of confined diblock copolymer films. *Macromolecules*, 30(10):3097–3103, May 1997.

[128] B. D. Olsen and R. A. Segalman. *Macromolecules*, 40:6922–, 2007.

[129] J.-W. Park and Y.-H. Cho. Surface-induced morphologies in thin films of a rodcoil diblock copolymer. *Langmuir*, 22(26):10898–10903, December 2006.

[130] J. Park and E. Thomas. Multiple ordering transitions: Hierarchical self-assembly of rod-coil block copolymers. *ADVANCED MATERIALS*, 15 (7-8):585–588, APR 17 2003.

[131] B. D. Olsen, D. Alcazar, V. Krikorian, M. F. Toney, E. L. Thomas, and R. A. Segalman. Crystalline structure in thin films of dehppv homopolymer and ppv-b-pi rodcoil block copolymers. *Macromolecules*, 41 (1):58–66, January 2008.

[132] B. D. Olsen, X. Li, J. Wang, and R. A. Segalman. Near-surface and internal lamellar structure and orientation in thin films of rod-coil block copolymers. *SOFT MATTER*, 5(1):182–192, 2009.

[133] D. Meng and Q. Wang. Hard-surface effects in polymer self-consistent field calculations. *JOURNAL OF CHEMICAL PHYSICS*, 126(23), JUN 21 2007. ISSN 0021-9606. doi: 10.1063/1.2740633.

[134] K. R. Shull, E. J. Kramer, G. Hadziioannou, and W. Tang. *Macromolecules*, 23:4780–, 1990.

[135] C. Nowak and T. Vilgis. Aggregates of rod-coil diblock copolymers adsorbed at a surface. *JOURNAL OF CHEMICAL PHYSICS*, 124(23), JUN 21 2006. ISSN 0021-9606. doi: 10.1063/1.2204912.

[136] B. D. Olsen and R. A. Segalman. Nonlamellar phases in asymmetric rod-coil block copolymers at increased segregation strengths. *MACROMOLECULES*, 40(19):6922–6929, SEP 18 2007.

[137] G. A. Buxton and N. Clarke. Computer simulation of polymer solar cells. *Modelling and Simulation in Materials Science and Engineering*, 15(2):13–26, 2007.

[138] N. S. Sariciftci, L. Smilowitz, A. J. Heeger, and F. Wudl. Photoinduced electron transfer from a conducting polymer to buckminsterfullerene. *Science*, 258(5087):1474–1476, 1992.

[139] B. Lei, Y. Yao, A. Kumar, Y. Yang, and V. Ozolins. Quantifying the relation between the morphology and performance of polymer solar cells using monte carlo simulations. *Journal of Applied Physics*, 104(2):024504, 2008.

[140] V. D. Mihailetchi, L. J. A. Koster, J. C. Hummelen, and P. W. M. Blom. Photocurrent generation in polymer-fullerene bulk heterojunctions. *Phys. Rev. Lett.*, 93(21):216601, Nov 2004.

[141] C. W. Tang. Two-layer organic photovoltaic cell. *Applied Physics Letters*, 48(2):183–185, 1986.

[142] P. Blom, V. Mihailetchi, L. Koster, and D. Markov. Device physics of polymer:fullerene bulk heterojunction solar cells. *Advanced Materials*, 19(12):1551–1566, 2007.

[143] G. Dennler, M. C. Scharber, and C. J. Brabec. Polymer-fullerene bulk-heterojunction solar cells. *Advanced Materials*, 21(13):1323–1338, 2009.

[144] G. Yu, J. Gao, J. C. Hummelen, F. Wudl, and A. J. Heeger. Polymer photovoltaic cells: Enhanced efficiencies via a network of internal donor-acceptor heterojunctions. *Science*, 270(5243):1789–1791, Dec. 15, 1995.

[145] W. Huynh, J. Dittmer, W. Libby, G. Whiting, and A. Alivisatos. Controlling the morphology of nanocrystal-polymer composites for solar cells. *Advanced Functional Materials*, 13(1):73–79, 2003.

[146] W. U. Huynh, J. J. Dittmer, and A. P. Alivisatos. Hybrid nanorod-polymer solar cells. *Science*, 295(5564):2425–2427, Mar. 29, 2002.

[147] S. Barrau, T. Heiser, F. Richard, C. Brochon, C. Ngov, K. van de Wetering, G. Hadziioannou, D. V. Anokhin, and D. A. Ivanov. Self-assembling of novel fullerene-grafted donoracceptor rodcoil block copolymers. *Macromolecules*, 41(7):2701–2710, April 2008.

[148] S. H. Park, A. Roy, S. Beaupre, S. Cho, N. Coates, J. S. Moon, D. Moses, M. Leclerc, K. Lee, and A. J. Heeger. Bulk heterojunction solar cells with internal quantum efficiency approaching 100 *Nat Photon*, 3(5):297–302, May 2009.

[149] M. Matsen and C. Barrett. Liquid-crystalline behavior of rod-coil diblock copolymers. *JOURNAL OF CHEMICAL PHYSICS*, 109(10):4108–4118, SEP 8 1998.

[150] M. Reenders and G. ten Brinke. Compositional and orientational ordering in rod-coil diblock copolymer melts. *MACROMOLECULES*, 35(8): 3266–3280, APR 9 2002.

[151] K. Coakley, B. Srinivasan, J. Ziebarth, C. Goh, Y. Liu, and M. McGehee. Enhanced hole mobility in regioregular polythiophene infiltrated in straight nanopores. *Advanced Functional Materials*, 15(12):1927–1932, 2005.

[152] E. Collini and G. D. Scholes. Coherent Intrachain Energy Migration in a Conjugated Polymer at Room Temperature. *Science*, 323(5912): 369–373, 2009.

[153] J.-L. Bredas and R. Silbey. Chemistry: Excitons surf along conjugated polymer chains. *Science*, 323(5912):348–349, 2009.

[154] T. Erb, U. Zhokhavets, G. Gobsch, S. Raleva, B. Sthn, P. Schilinsky, C. Waldauf, and C. Brabec. Correlation between structural and optical

properties of composite polymer/fullerene films for organic solar cells. *Advanced Functional Materials*, 15(7):1193–1196, 2005.

[155] W.-H. Baek, H. Yang, T.-S. Yoon, C. Kang, H. H. Lee, and Y.-S. Kim. Effect of p3ht:pcbm concentration in solvent on performances of organic solar cells. *Solar Energy Materials and Solar Cells*, 93(8):1263–1267, August 2009.

[156] H. Sirringhaus, P. J. Brown, R. H. Friend, M. M. Nielsen, K. Bechgaard, B. M. W. Langeveld-Voss, A. J. H. Spiering, R. A. J. Janssen, E. W. Meijer, P. Herwig, and D. M. de Leeuw. Two-dimensional charge transport in self-organized, high-mobility conjugated polymers. *Nature*, 401 (6754):685–688, October 1999.

[157] L. Kinder, J. Kanicki, and P. Petroff. Structural ordering and enhanced carrier mobility in organic polymer thin film transistors. *Synthetic Metals*, 146(2):181–185, October 2004.

[158] Y.-K. Lan and C.-I. Huang. A theoretical study of the charge transfer behavior of the highly regioregular poly-3-hexylthiophene in the ordered state. *The Journal of Physical Chemistry B*, 112(47):14857–14862, November 2008.

[159] S. Selberherr. *Analysis and Simulation of Semiconductor Devices.* New York: Springer, 1984.

[160] A. Fahrenbruch and R. Bube. *Fundamentals of Solar Cells.* New York: Academic Press, 1983.

[161] L. Onsager. Initial recombination of ions. *Phys. Rev.*, 54(8):554–557, Oct 1938.

[162] C. L. Braun. Electric field assisted dissociation of charge transfer states as a mechanism of photocarrier production. *The Journal of Chemical Physics*, 80(9):4157–4161, 1984.

[163] P. W. M. Blom, M. J. M. de Jong, and S. Breedijk. Temperature dependent electron-hole recombination in polymer light-emitting diodes. *Applied Physics Letters*, 71(7):930–932, 1997.

[164] S. Lacic and O. Inganas. Modeling electrical transport in blend heterojunction organic solar cells. *Journal of Applied Physics*, 97(12):124901, 2005.

[165] J. C. Scott and G. G. Malliaras. Charge injection and recombination at the metal-organic interface. *Chemical Physics Letters*, 299(2):115–119, January 1999.

[166] S. Lacic and O. Inganas. Modeling electrical transport in blend heterojunction organic solar cells. *Journal of Applied Physics*, 97(12):124901, 2005.

[167] D. Scharfetter and H. Gummel. Large-signal analysis of a silicon read diode oscillator. *Electron Devices, IEEE Transactions on*, 16(1):64–77, Jan 1969.

[168] M. Shah, V. Pryamitsyn, and V. Ganesan. Thin film morphologies of rod-coil block copolymers. *(Unpublished)*.

[169] D. Gupta, M. Bag, and K. S. Narayana. Correlating reduced fill factor in polymer solar cells to contact effects. *APPLIED PHYSICS LETTERS*, 92(9), MAR 3 2008.

[170] M.-S. Kim, B.-G. Kim, and J. Kim. Effective variables to control the fill factor of organic photovoltaic cells. *ACS APPLIED MATERIALS & INTERFACES*, 1(6):1264–1269, JUN 2009.

[171] Y. Tao, B. McCulloch, S. Kim, and R. Segalman. The relationship between morphology and performance of donor acceptor rod-coil block copolymers solar cells. *Soft Matter (Accepted)*, 2009.

Vita

Manas R. Shah was born in Mumbai, India and attended Atomic Energy Junior College, Mumbai, India. He received his Bachelors of Technology degree in Chemical Engineering from the Indian Institute of Technology, Bombay in the year 2004. He began his graduate studies in Chemical Engineering at the University of Texas at Austin in August 2004.

Permanent Address: B102 Simran Palace, Plot-13, Sector-14,
Palm Beach Road, Sanpada, Navi Mumbai,
Maharashtra, 400705 India

This dissertation was typeset with LaTeX 2ε[1] by the author.

---

[1] LaTeX 2ε is an extension of LaTeX. LaTeX is a collection of macros for TeX. TeX is a trademark of the American Mathematical Society. The macros used in formatting this dissertation were written by Dinesh Das, Department of Computer Sciences, The University of Texas at Austin, and extended by Bert Kay, James A. Bednar, and Ayman El-Khashab.